# Experimental Investigation of Fully Developed Flows of a Newtonian Fluid in Straight Rectangular Ducts with Adjacent Open and Porous-Metal-Foam Domains

by

**James Medvescek**

**Department of Mechanical Engineering**

**McGill University**

**Montréal, Québec, Canada**

**A thesis submitted to McGill University**

**in partial fulfilment of the requirements for the degree of**

**Master of Engineering**

# Abstract

Over the last two decades, porous metal foams (which have very high values of surface-area-to-volume ratio, of the order of 10,000 square meters per cubic meter; and values of porosity in the range 0.85-0.98) have been increasingly used in devices for heat transfer (ultra-compact heat exchangers and heat sinks; heat pipes; and loop heat pipes), filtration, catalytic conversion, and acoustical control. In computational methods for thermofluid optimization of such devices, cost-effective modeling of fluid flows in adjacent open and porous-metal-foam domains is done using two different, but compatible, sets of volume-averaged governing equations; and at the interface between these domains, the intrinsic-phase-averaged pressure, phase-averaged fluid velocity, and normal stress are assumed to be continuous, and a tangential stress-jump condition, with two adjustable coefficients, is imposed. Accurate experimental data for determining these adjustable coefficients and establishing possible laminar-turbulent transition criteria for the aforementioned flows are urgently needed.

In the present work, an experimental investigation of fully developed flows of air in a straight, uniform, rectangular duct of high cross-sectional aspect ratio and containing open and porous-metal-foam domains was undertaken. These flows are akin to those studied in the classical Beavers-Joseph problem. Four different porous metal foams (with nominal pores per inch designations of 20, 40, 60; nominal thickness of 12.7 mm; and porosity in the range 0.85-0.94) were considered. An experimental facility was specially designed and constructed to allow test-section configurations of nominal open-domain heights of 0 (completely filled with porous metal foams), 3.175 mm, 6.35 mm, and 12.7 mm. The nominal width and length of the test section was fixed at 152.4 mm and 457.2 mm, respectively. The top wall of the test section had 64 wall-static-pressure taps and also a wall-shear-stress sensor, which was redesigned (improved) from an earlier version. The airflow rates were measured using a Venturi tube (specially designed, constructed, and calibrated for this work) and a bank of laminar flow elements. An analytical solution for laminar fluid flows in the problems of interest was adapted from other works in the published literature.

The results obtained from experiments undertaken for benchmarking tasks, characterization of the porous metal foams (photomicrographs; ligament, pore, and cell effective diameters; and porosity), and calibration of the wall-shear-stress sensor are presented and discussed. Data from experiments undertaken to determine the permeability and dimensionless form-drag coefficient of the porous metal foams were processed using four different approaches, and the results are presented and comparatively discussed.

Comprehensive sets of experimental data collected for airflows in adjacent open and porous-metal-foam domains (in the laminar, transitional, and turbulent regimes) are presented and discussed. These experimental data, the analytical solution for such problems with laminar flows, power-spectral-density (PSD) plots of the instantaneous wall-shear-stress measurements, and the requirements for physically tenable values for the laminar-flow results were collectively used to obtain guidance regarding laminar-turbulent transition, and then deduce the two coefficients in the interfacial jump condition on the shear stress.

For flows through test sections completely filled with the porous metal foams, the data collected were used to obtain a Darcy friction factor as a function of a Reynolds number (both based on the superficial velocity of the air and the effective diameter of the metal-foam ligaments). The data collected in the experiments on flows in test sections with adjacent open and porous domains were used to obtain the open-domain Darcy friction factor as a function of the corresponding Reynolds number. These results are presented and discussed.

# Résumé

Au cours des deux dernières décennies, les mousses métalliques poreuses, MMP, (ayant des valeurs très élevées de superficie d'échange thermique volumétrique, de l'ordre de 10 000 mètres carrés par mètre cube, et valeurs de la porosité de 0,85 à 0,98) sont devenues de plus en plus commun dans plusieurs domaines: le transfert thermique (échangeurs de chaleur ultracompacts, dissipateurs de chaleur, caloducs et des caloducs en boucle), la filtration; la conversion catalytique; et l'acoustique. Les simulations numériques d'écoulements en domaines ouvert / de MMP adjacents se font en résolvant deux équations différentes (moyennées volumétriquement), correspondant aux deux domaines différents. À l'interface de ceux-ci, la pression intrinsèque (moyennée), la vélocité du fluide (moyenné), et la contrainte normale sont supposées être continues, et une discontinuité de la contrainte tangentielle à l'interface, avec deux coefficients réglables, est imposée. La connaissance de ces coefficients réglables, et l'établissement de critères de transition laminaire-turbulent pour ces types d'écoulements nécessitent urgemment des données expérimentales précises.

Le travail ci-inclus comprend une étude expérimentale d'écoulements d'air pleinement développés, en canal rectangulaire et uniforme, de rapport largeur/hauteur élevé, et contenant des domaines ouvert / de MMP adjacents. De tels écoulements ressemblent à ceux étudiés dans le problème Beavers-Joseph. Quatre MMP différentes (ayant des pores de tailles nominaux de 20, 40, 60 pores par pouce, une épaisseur nominale de 12,7 mm, et des porosités allant de 0,85 à 0,94) furent examinées. Un dispositif expérimental fut conçu et construit pour permettre des configurations d'hauteurs du domaine ouvert dans la section de mesure de 0 (complètement rempli de MMP), 3,175 mm, 6,35 mm, et 12,7 mm. La largeur nominale et la longueur de la section de mesure furent fixées à 152,4 mm et 457,2 mm, respectivement. La paroi supérieure de la section de mesure possède 64 prises de pression statique et un capteur de contrainte de cisaillement à la paroi. Les débits d'air furent mesurés en utilisant un tube de Venturi (spécialement conçu, construit, et étalonné pour ce travail) et une banque d'éléments laminaires.

Les résultats obtenus des expériences menées pour i) des tâches d'analyse comparative; ii) la caractérisation des mousses métalliques (microphotographes; diamètres effectifs des ligaments, des pores et des cellules; porosité); et iii) l'étalonnage du capteur de contrainte de cisaillement sont présentés et interprétés. Les données provenant des expériences mesurant la perméabilité et le coefficient adimensionnel de traînée de forme des MMP furent déterminées selon quatre approches différentes, et comparées.

Des ensembles de données expérimentales recueillies en écoulements d'air en domaines ouvert / poreux adjacents (dans les régimes laminaire, de transition, et turbulent) furent présentés et analysés. Ces données, la solution analytique de tels écoulements laminaires, les densités spectrales de puissance des mesures instantanées de la contrainte de cisaillement à la paroi, et les conditions nécessaires correspondantes au régime laminaire furent collectivement utilisées pour obtenir des indicateurs concernant la transition laminaire-turbulent, et pour déduire les deux coefficients dans la condition de discontinuité de la contrainte de cisaillement à l'interface.

Les données provenant des mesures dans lesquelles le canal était complètement rempli de MMP furent utilisées pour calculer un coefficient de frottement de Darcy en fonction du nombre de Reynolds (basé sur la vélocité superficielle de l'air et le diamètre effectif des ligaments de la MMP). Les données recueillies dans les expériences en domaines ouverts / poreux adjacents furent utilisées pour obtenir le coefficient de frottement de Darcy (du domaine ouvert) en fonction du nombre de Reynolds correspondant. Ces résultats sont présentés et interprétés.

**I dedicate this thesis to my uncle**

**Karl Dusan Medvescek**

**1957-2012**

# Acknowledgements

I would like to express my sincerest gratitude to both of my supervisors, Professor B. Rabi Baliga and Professor Laurent B. Mydlarski, for accepting me to be one of their students, and for offering me such an interesting, and challenging thesis project. Both of your continual support and guidance throughout my M.Eng. studies has been greatly appreciated, and I have most certainly learned a great deal from both of you.

I would also like to thank the Natural Sciences and Engineering Research Council (NSERC) of Canada, the Fonds de recherche du Québec - Natures et technologies (FRQNT), McGill University, and my two supervisors, for providing me with financial support throughout the course of my studies.

I would especially like to thank my lab partner and friend, Samer Afara, for working with me to redesign the wall-shear-stress sensor he had designed and built earlier, in his M.Eng. work. Your inputs were significant contributions to this work, and our new sensor was a key element to obtaining excellent data.

To my parents, Ingo and Mary, my brothers, Alex and Nick, the rest of my family, and to my friends, Kyran, Mike, Eric, Adam, and Nicky, your continual support and encouragement throughout my studies has been tremendous. To my girlfriend, Anouk, your patience, love, understanding, and encouragement have been absolutely amazing during my Master's. I also very much appreciate the visits (and bringing me some dinners) during my extremely long measurement days.

This project could not have been completed were it not for Mr. Chunilal Mistry, his son Bhavesh, and his employees at the Bhavesh Machine Shop, who machined the air channel, transition box, Venturi tube, and wall-shear-stress sensor components. I would also like to thank the technical staff of the Faculty of Engineering, especially Antonio (Tony) Micozzi, Andy Hofmann, and Mathieu Beauchesne for their inputs and help in machining the metal foam test sections. Many thanks to Professor Larry Lessard and

Professor Pascal Hubert for kindly granting me access to the Composites Laboratory and the oven there for heat-curing the epoxies used in attaching the metal foam to the test sections.

For their technical support and inputs, I would like to thank the following people: Jean-Pierre Bessette and Martin Richer from Polycontrols Inc.; Cassidy Clark from Erg Aerospace; Mark Heamon from Selee Corporation; Charles Clement from Crystex Composites LLC; Ariel Kemer for expertly welding the Venturi tube connections; and Éric Dubé from WeldPro Inc.

For help with a number of formalities of graduate school and thesis submission tasks, thanks go to Ms. Emily McHugh and Ms. Joyce Nault.

Last, but not least, I would also like to thank my other lab partners for their support, Jeffrey Poissant, Nirmalakanth (Nirma) Jesuthasan, Alexandre Lamoureux, Brandon Tulloch, Laura Yakuma, and Iurii Lokhmanets.

# Table of Contents

# Nomenclature

## English Symbols

| | |
|---|---|
| $a$ | Curve-fit constant used in the determination of the permeability |
| $A_{cs}$ | Cross-sectional area of the duct |
| $b$ | Curve-fit constant used in the determination of the dimensionless form-drag coefficient |
| $c_F$ | Dimensionless form-drag coefficient |
| $C$ | Venturi tube discharge coefficient |
| $d$ | Internal diameter of the cylindrical throat of the Venturi tube |
| $d_c$ , $d_p$ | Metal foam cell and pore diameters, respectively |
| $d_i$ , $d_l$ | Inner and outer diameters of a hollow ligament, respectively |
| $dp / dx$ | Gradient of time-averaged wall-static pressure in the test section |
| $D$ | Internal diameter of the upstream cylindrical section of the Venturi tube |
| $D_h$ | Hydraulic diameter of the rectangular test section |
| $D_{h-od}$ | Hydraulic diameter of the open domain of the test section |
| $D_i$ | Inner diameter of a laminar flow element tube |
| $Da$ , $Da_{d_l}$ | Darcy number based on $H^2$ and $d_l^2$, respectively |
| $E$ | Voltage supplied to the hot-wire by the CTA |
| $f_D$ , $\left(f_D\right)_{d_l}$ | Darcy friction factor based on $D_h$ and $d_l$, respectively |
| $f_{D-od}$ | Darcy friction factor based on $D_{h-od}$ |
| $Fo$ | Forchheimer number |
| $g$ | Acceleration due gravitational attraction of the earth |
| $H$ | Total test-section height |
| $i, j$ | Cartesian subscripts; indicial notation |
| $K$ | Permeability |
| $L$ | Length of the porous-metal-foam sample |
| $L_{dev,\,laminar}$ | Laminar-flow development length |
| $L_{dev,\,turbulent}$ | Turbulent-flow development length |

| | |
|---|---|
| $L_{LFE}$ | Length between the centers of the two pressure taps of an *LFE* tube |
| $\dot{m}$ | Mass flow rate of air flowing through the air channel |
| $\dot{m}_{calibration}$ | Mass flow rate of air flowing through the Venturi tube during calibration |
| $\dot{m}_{LFE}$ | Mass flow rate of air flowing through an *LFE* tube |
| $\dot{m}_{method}$ | Mass flow rate of air flowing through the Venturi tube as calculated from an iterative method |
| $\dot{m}_{od}$ | Mass flow rate in the open domain of the test section |
| $\dot{m}_{total}$ | Total mass flow rate in the test section |
| $\dot{m}_{Venturi}$ | Mass flow rate of air flowing through the Venturi tube |
| $\boldsymbol{n}$ | Unit normal vector, point from the porous to the open domain |
| $p$ | Static pressure (in the open domain); intrinsic phase-average static pressure (in the metal foam domain) |
| $p_{atm}$ | Absolute atmospheric air pressure in the laboratory |
| $p_1$ , $p_2$ | Absolute static pressure at the upstream and throat taps of the Venturi tube |
| $\Delta p$ | Differential pressure |
| $R$ | Coefficient of determination; ratio of the inner-to-outer ligament diameters |
| $R_a$ | Cold-wire electrical resistance (at the room temperature) |
| $R_{amb}$ | Electrical resistance of the sensor under ambient conditions |
| $R_{op}$ | Operating electrical resistance of the hot-wire |
| $R_{pr}$ | Combined resistance of the two prongs of the wall-shear-stress sensor |
| Re | Reynolds number |
| $\mathrm{Re}_d$ | Reynolds number at the throat of the Venturi tube |
| $\mathrm{Re}_{d_l}$ | Reynolds number based on the ligament diameter of the metal foam |
| $\mathrm{Re}_m$ | Reynolds number based on half of the open test section |
| $\mathrm{Re}_{od}^{D_h}$ | Reynolds number in the open domain of the test section |
| $T$ | Temperature |
| $t$ | Time variable; thickness of the porous-metal-foam sample |

| | |
|---|---|
| $t1$ | Open-height of an air channel (inlet or test sections) c-channel |
| $t2$ | Side-rail thickness |
| $u_*$ | Dimensionless velocity in the problem of interest |
| $u_{\infty *}$ | Dimensionless velocity in the central region of the porous domain |
| $u_{av}$ | Average fluid velocity in the cross-section of the air channel |
| $u_{av-od}$ | Average fluid velocity in the cross-section of the open domain |
| $u_{av-pd}$ | Average fluid velocity in the cross-section of the porous domain |
| $u_i, u_j$ | $i$ and $j$ components of velocity (in the open domain); superficial velocity |
| $u_t$ | Velocity tangential to the interface |
| $U$ | Reference velocity in the analytical solution for laminar flow in a rectangular duct (open; no foam) |
| $\overline{U}$ | Average dimensionless fluid velocity in the cross section of the test section |
| $U_{c_F}$ | Experimental uncertainty in the dimensionless form-drag coefficient |
| $U_K$ | Experimental uncertainty in the permeability |
| $v$ | Velocity (open domain); superficial velocity vector (porous domain) |
| $V$ | Total volume of a representative elementary volume |
| $V_b$ | Porous metal foam bulk volume |
| $V_{baro}$ | Output voltage of the electronic barometer |
| $V_f$ | Volume of the fluid phase contained within a porous medium or r.e.v. |
| $V_s$ | Volume of the solid structural matrix of the porous medium |
| $W_{channel}$ | Width of the cross-section of the rectangular air channel |
| $x$ | Cartesian coordinate |
| $x_i, x_j$ | Cartesian coordinate in the $i$ and $j$ directions |
| $X_{\text{int}erface}$ | Coefficient in the dimensionless form of the stress-jump condition |
| $y$ | Cartesian coordinate |
| $y_*$ | Dimensionless coordinate normal to the open-porous interface |
| $Y_{\text{int}erface}$ | Coefficient in the dimensionless form of the stress-jump condition |

**Greek Symbols**

| | |
|---|---|
| $\alpha$ | Overheat ratio of the wall-shear-stress sensor |
| $\beta_1$ | Coefficient related to excess viscous stress (interfacial stress-jump B.C) |
| $\beta_2$ | Coefficient related to excess inertial stress (interfacial stress-jump B.C) |
| $\delta_{ij}$ | Kronecker delta |
| $\varepsilon$ | Porosity |
| $\xi$ | Ratio of the throat-to-upstream absolute pressure of the Venturi tube |
| $\eta$ | Expansibility or expansion factor of the fluid within the Venturi tube |
| $\kappa$ | Isentropic constant of air |
| $\mu$ | Dynamic viscosity of air |
| $\rho$ | Density of air |
| $\rho_b$ | Bulk density of the porous medium |
| $\rho_s$ | Density of the solid material of the structural matrix of the porous medium |
| $\sigma_{ij}$ | Total stress tensor |
| $\tau_{od}^{UW}$ | Shear stress at the upper-wall of the problem of interest |
| $\tau_{od}^{I}$ | Open-domain shear stress at the interface |
| $\overline{\tau}_w$ | Time-averaged wall-shear stress at the top wall of the test section |
| $\phi$ | Ratio $d / D$ for Venturi tube |
| $\omega$ | Ratio of open-domain height to total test-section height |

# Chapter 1 – Introduction

## 1.1 Motivation and Overall Goal

Porous media are materials consisting of a solid or semi-solid matrix with interconnected voids, which allow the flow of one or more fluids through the material [Dullien (1992); Nield and Bejan (2013)]. A variety of man-made and natural porous media, such as textiles, paper, brick, limestone, sand, wood, and lungs, are encountered on a daily basis [Nield and Bejan (2013)]. Sand dunes and gravel beds [McLean and Nikora (2006)], suspended sediment layers (for example, at the bottom of lakes, reservoirs, and estuaries) [Higashino and Stefan (2012)], terrestrial and aquatic vegetation canopies [Finnegan and Shaw (2008); Kubrak et al. (2008); Dimitris and Panayotis (2011)], and urban landscapes such as cities [Hu et al. (2012)] can also be regarded as porous media, with fluid flows over and through them. Other man-made or engineered porous media include composite materials and highly-porous metal foams [Nield and Bejan (2013)].

Over the last 15 years, porous metal foams have emerged as a viable and attractive option in engineering applications that require high intrinsic porosity ($\varepsilon$) and large values of surface-area-to-volume ratio ($\alpha_{sv}$), such as devices used for heat transfer, filtration, chemical reactions, catalysis, and acoustical control [Ashby et al. (2000)]. Porous metal foams are characterized by high values of $\varepsilon$ (typically, 0.88 – 0.96) and very high values of $\alpha_{sv}$ (~ 10,000 $m^2/m^3$), and also offer other advantages. For example, porous-metal-foam ultra-compact heat exchangers offer the following benefits compared to conventional heat exchangers (shell-and-tube, plate, and compact, which are characterized by $\alpha_{sv}$ = 100 - 1,500 $m^2/m^3$) [Boosma and Poulikakos (2002); Boosma et al. (2003)]: higher rates of heat transfer for fixed pumping power; higher thermal effectiveness; lower core volume, weight, and costs for comparable rates of heat transfer; and less complex fabrication procedures. Recently, Nawaz et al. (2012) performed experiments on porous-metal-foam compact heat exchangers and concluded that they outperform geometrically similar louver-finned heat exchangers. Thus, porous-metal-foam heat exchangers are being considered for many applications involving thermal

management: examples include heat sinks for portable computers, heat pipes and loop heat pipes, vapor spreaders, industrial “micro” gas turbine recuperators, next-generation solar energy collectors, and thermal energy storage systems [Albanakis et al. (2009); Muley et al. (2012)].

It should also be noted that compared to polymer foams, metal foams offer higher strength and rigidity, are thermally and electrically conductive, and maintain their mechanical properties at significantly higher temperatures [Ashby et al. (2000)]. Furthermore, in comparison to ceramic foams, metal foams can deform elastically and plastically, and thus have the ability to absorb mechanical energy [Lefebvre et al. (2008)].

In many of the above-mentioned examples of porous media, fluid flows occur over and through these media. In the aforementioned applications of porous metal foams (which are the porous media of particular interest in this work) in thermal management devices, fluid flows also occur in adjacent open and porous domains [Maydanik (2005); Nield and Bejan (2013)]. Computational studies are being increasingly used for optimizing the thermofluid performance of devices that use porous metal foams. In such studies, a cost-effective approach to the modeling of fluid flows in adjacent open and porous (metal foam) domains is to use two different, but compatible, sets of volume-averaged governing equations [Whitaker (1999); Nield and Bejan (2013)]. At the interface between these domains, the phase-averaged fluid velocity and normal stress are assumed to be continuous, and a tangential stress-jump condition, with two adjustable coefficients, is imposed [Ochoa-Tapia and Whitaker (1998); Nield and Bejan (2013)].

Accurate experimental data for determining the above-mentioned two adjustable coefficients in the stress-jump condition at the interface between the open and porous-metal-foam domains, and also for providing guidance on laminar-turbulent transition of the flow in the open domain, in the problems of interest are urgently needed. The overall goal of the work presented in this thesis was to fulfill at least part of this need. In particular, an experimental investigation was undertaken of fully developed flows of air in straight, uniform rectangular ducts of high cross-sectional aspect ratio, containing

adjacent open and porous domains, with four different porous metal foams and three ratios of nominal open-to-porous gap heights (¼, ½, and 1). These particular flows, which are schematically illustrated in Figure 1.1, are akin to those studied in the seminal work of Beavers and Joseph (1967). The specific objectives are presented in the next section.

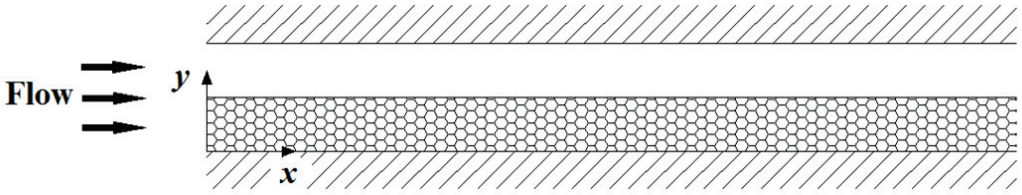


Figure 1.1: Schematic representation of the problems of interest

## 1.2 Specific Objectives

The specific objectives of this thesis are summarized below.

- Design and construction of a straight, rectangular air tunnel facility for an experimental investigation of fully developed flows of air in test sections with adjacent open and porous-metal-foams domains (see Figure 1.1), and implementation and calibration/benchmarking of instruments/set-ups for the following measurements:
    - Mass flow rate
    - Static-pressure distribution on the wall of the open domain
    - Shear-stress distribution on the wall of the open domain
- Experimental procedures and measurements for the following purposes:
    - Metal-foam characterization: geometric aspects of the metal matrix; porosity; intrinsic permeability; and dimensionless form-drag coefficient
    - Guidance for laminar-turbulent transition of the air flows in the open domains of the problems of interest (see Figure 1.1).
    - Two dimensionless coefficients in the interfacial stress-jump condition

## 1.3 Literature Review

There have been numerous publications on fluid flows in porous media. The goal in this section is not the presentation of an exhaustive review of this literature; instead, it is a review of publications that are directly related to and/or useful for the present work. This

review is subdivided into the following sections: (a) fluid flows and pressure drops in porous media; (b) determination of the intrinsic permeability and form-drag coefficient; and (c) fluid flows in adjacent open and porous domains.

### 1.3.1 Fluid Flows and Pressure Drops in Porous Media

The seminal work in the area of fluid flows in porous media is attributed to Henry Darcy (1856). Commissioned by the city of Dijon, a portion of his experiments dealt with water filtration and led to the development of a relationship that is today referred to as "Darcy's Law" or the Darcy equation [Nield and Bejan (2013)]. This equation represents Darcy's finding that for steady-state, unidirectional, creeping, isothermal flow of an incompressible Newtonian fluid (water) in an isotropic porous medium (filter), the ratio of the average cross-sectional fluid velocity (superficial velocity) to the gradient of the intrinsic phase-averaged pressure is equal to a constant value, $k$, dependent on both the geometry of the porous medium and the fluid under consideration [Lage (1998)].

The current form of the Darcy equation incorporates a slight, but important, modification: $k$, is replaced by the dynamic viscosity of the fluid divided by a different constant, $K$, denoted as the intrinsic permeability (from this point on, referred to as permeability), which is independent of the fluid but dependent on the geometry of the porous medium [Kaviany (1995); Dullien (1992); Nield and Bejan (2006)]. Lage (1998) calls it the Hazen-Darcy equation (referred to in this thesis as the Darcy equation), and acknowledges the related works of Hazen (1893) and Krüger (1918).

At fluid velocities greater than those involved in the study conducted by Darcy, Dupuit (1863), borrowing ideas from Prony (1804), reasoned that the gradient of the intrinsic-phase-averaged pressure could be calculated from a quadratic function of the superficial velocity. The quadratic term was the drag (or "*forme force*") the fluid experiences as it flows past the solid obstacles within the porous medium [Lage (1998)]. The resulting equation is commonly referred to as the Darcy-Forchheimer equation [Beavers et al. (1973); Givler and Altobelli (1994); Nield and Bejan (2013)]; however, Lage (1998) has

called it the Hazen-Darcy-Dupuit equation, as Forchheimer (1901) had not proposed the aforementioned extension, but only affirmed it.

Ward (1964) performed a dimensional analysis of the Darcy-Forchheimer equation, and expressed the quadratic term as a product of the fluid density, square of the superficial velocity, and a dimensionless form-drag coefficient, $c_F$, divided by the square root of the permeability. Several different porous media made of particles that were approximately spherical in shape were considered in the study by Ward (1964). The Fanning friction factor for these porous media was plotted against a Reynolds number, based on the permeability of the porous media. These plots demonstrated an asymptotic region at high Reynolds numbers, in which the friction factor was effectively constant, leading him to claim that the aforementioned drag coefficient was "universal" for all porous media.

Many authors have used the dimensionless form-drag coefficient divided by the square root of the permeability as a dimensional form of this coefficient, C, [Lage (1998); Boosma and Poulikakos (2003); Despois and Mortensen (2004)]. Some authors have referred to the dimensional form-drag coefficient as a non-Darcian permeability [Innocentini et al. (1999a, 1999b, 1999c); Moreira et al. (2004); Biasetto et al. (2007)]. Joseph et al. (1982) confirmed the usefulness of the dimensionless form-drag coefficient, but with reference to the works of Beavers and Sparrow (1969) and Schwartz and Probstein (1969), disagreed that it is a universal constant for all porous media.

A cubic term has been proposed as an extension to the Darcy-Forchheimer equation [Mei and Auriault (1991); Firdaouss et al. (1997); Wodie and Levy (1991); Lage et al. (1997)]. However, Lage and Antohe (2000) claimed there is no experimental support (or physical justification) for the inclusion of a cubic term. For flows in highly porous media, Brinkman (1949) added an additional term, analogous to the viscous term found in the Navier-Stokes equations, to account for the viscous shear stress on the fluid caused by the surfaces within the porous medium. This term incorporates the so-called Brinkman or effective dynamic viscosity of the fluid. It allows boundary-layer development along interfaces (such as those adjacent to open domains and solid walls) and enables the

inclusion of suitable boundary conditions, such as the no-slip condition at boundary walls [Givler and Altobelli (1994); Nield and Bejan (2013)]. Joseph et al (1982) recommend the use of the dynamic viscosity of the fluid, and Vafai and Tien (1981) use the dynamic viscosity of the fluid divided by the porosity, in place of the effective dynamic viscosity. Further discussions of the Brinkman term can be found in Nield and Bejan (2013).

### 1.3.2 Determination of the Permeability and Form-Drag Coefficient

If full details of the geometry of the porous medium are known, the permeability and dimensionless form-drag coefficient can be determined theoretically [Dullien (1992); Kaviany (1995); Nield and Bejan (2013)]. Thus, for fluid flows in beds of spherical particles, both the permeability and dimensionless form-drag coefficient can be calculated as functions of the porosity and mean particle diameter [Ergun (1952)]. For a close-packed bed of spherical particles of the same diameter, the permeability can be calculated using the Carman-Kozeny relationship [Nield and Bejan (2013)]. Additional expressions of this type can be found in Dullien (1992).

For fluid flows in porous metal foams, some authors have proposed both empirical and semi-empirical models to predict the permeability and form-drag coefficient. Edouard et al. (2008) critically reviewed many proposed models based on a variety of geometric properties, such as the pore diameter or window size, cell size, strut or ligament diameter, porosity, number of pores per inch (PPI), specific surface area, and tortuosity. Purely empirical models were not recommended due to the large experimental errors commonly found in the related pressure-drop and velocity data available in the published literature. Semi-empirical models were preferred, namely, those of du Plessis et al. (1994) and Lacroix et al. (2007), as these models gave the best predictions (±30%) of the experimental data collected in the work of Edouard et al. (2008). In the study of du Plessis et al. (1994) the pore diameter was calculated from the PPI designation provided by the manufacturer. However, the PPI designation has been found to be an inaccurate way of specifying or measuring the pore diameter [Onstad et al. (2012)].

Fourie and du Plessis (2002) built on the work of du Plessis (1994) and modeled the porous-metal-foam structure with tetrakaidecahedrons. Using the analogy of a cylinder in cross-flow to model the hydrodynamic stresses and recirculation in the metal foams at higher Reynolds numbers, an equivalent cylinder diameter and representative hydraulic diameter (RHD) were calculated. The permeability was calculated solely as a function of cell diameter, porosity, and tortuosity, whereas the dimensionless form-drag coefficient was also calculated as a function of the Reynolds number. Woudberg and du Plessis (2010) further refined the model of du Plessis et al. (1994), to make it applicable to high-porosity foams. Lacroix et al. (2007) used silicon carbide foams and modeled the foam structure as a dodecahedron cell. In the equations they put forth, the cell size (diameter of the dodecahedron) of the foam was the only parameter required for determining the permeability and form-drag coefficient. The authors stated they cannot give any physical reasoning to explain their model, but it predicted their experimental data well.

Calmidi (1998) represented the structure of high-porosity metal foams by dodecahedron-shaped cells, and then related the parameters of the dodecahedron cell to a unit-cube-cell made from cylindrical rods. The porosity and cell size of the foam (distance between two pentagonal faces of the dodecahedron) were used as inputs to a semi-empirical correlation for the determination of the permeability and form-drag coefficient. Also incorporated into the proposed semi-empirical correlation was the ratio of ligament diameter to pore diameter of the dodecahedral cell, which included a shape factor to account for the change in ligament cross-section, which was observed to be a function of the porosity.

When using the aforementioned or any other empirical or semi-empirical models found in the literature for the determination of the permeability and dimensionless form-drag coefficient, it should be noted that there are many discrepancies in the available experimental results: for example, pressure-drop data for metal foams available in the literature are inconsistent [Paek et al. (2000); Moreira et al. (2004)]. These discrepancies can be attributed to inadequacies in experimental procedures and analyses for determining the permeability and dimensionless form-drag coefficient. There are also inconsistencies and difficulties in the methods for determining the microstructure of the foam [Paek et al.

(2000); Madani et al. (2007)]. These, in turn, have adverse effects on the accuracy of related semi-empirical models.

Semi-empirical models are desirable from a practical standpoint, but not when large errors, such as those encountered in Edouard et al. (2008), are unacceptable. For a potentially more accurate approach, reliable experimental pressure-drop and superficial-velocity data are required from investigations of steady-state, unidirectional, incompressible flow of a Newtonian fluid in porous media with negligible boundary effects. Under these assumptions, the Darcy-Forchheimer equation is applicable, and the permeability and form-drag coefficient can be calculated by performing a least-squares curve-fit of the experimental data [Ward (1964); Beavers et al (1973); Givler and Altobelli (1994); Antohe et al. (1997); Calmidi (1998); Innocentini et al. (1999a, 1999b, 1999c); Boosma and Poulikakos (2002); Zeng and Grigg (2006); Biasetto et al. (2007)].

Dukhan and Minjeur II (2011) proposed that two permeabilities exist, one for fluid flow within the Darcy regime, and another in the Forchheimer regime, referred to as the Darcian and Forchheimer permeabilities, respectively. Miwa and Revankar (2009) performed experiments, only collecting data in the Darcy regime, and subsequently calculated the permeability of the metal foam (INCO) used in their study. The data of Innocentini et al. (1999a) appeared to be within the Darcy regime, and the form-drag contributed as low as one percent of the total pressure drop, but no comparisons similar to those undertaken by Ward (1964) were made. Investigations akin to that of Dukhan and Minjeur II (2011) require demarcation of the conditions when the fluid flow transitions from the Darcy regime to the quadratic Forchheimer regime. Boosma and Poulikakos (2002) calculated the permeability from data points within the Darcy regime and determined a transitional (from Darcy to Forchheimer regimes) Reynolds number based on the permeability. They maintained that all data points should be used for the determination of the permeability and form-drag coefficient.

Flow transition from Darcy to Forchheimer regimes has primarily been tied to values of the superficial velocity, Reynolds number (with a variety of parameters used as the length

scale), and Forchheimer number. Biasetto et al. (2007) have suggested a transitional superficial velocity of 0.1 m/s. Bonnet et al. (2008) used the pore diameter as a length scale and determined a transitional Reynolds number to be approximately 200. Miwa and Revankar (2009) stated that the pore diameter is an inappropriate length scale, as it varies widely in porous metal foams. They and other authors suggested that a more appropriate length scale is the square-root of the permeability. Givler and Altobelli (1994) and Lage et al. (1997) concluded that such a transition occurs at a permeability-based Reynolds number of unity, while Boosma and Poulikakos (2002), Boosma et al. (2003), and Miwa and Revankar (2009) proposed values of 10, 20, and 26.5, respectively.

Lage (1998) argued that a good indicator of the transition from Darcy to Forchheimer regimes is the ratio of form-drag to viscous-drag forces, often referred to as the Forchheimer number; this ratio could also be considered as a Reynolds number with the product of the permeability and dimensional form-drag coefficient as the length scale. Lage et al. (2005) and Zeng and Grigg (2006) reported critical Forchheimer numbers of unity and 0.11, respectively. The critical value proposed by Zeng and Grigg (2006) was determined from a more practical point of view, based on their finding that the aforementioned transition occurs when the form-drag term of the Darcy-Forchheimer equation accounts for ten percent of the overall pressure drop. Innocentini et al. (2010) reported that a Forchheimer number much less than unity ensures that the fluid flow is in the Darcy regime. The square-root of the permeability and the pore diameter are the primary length scales used in Reynolds numbers associated with high-porosity porous metal foams. Lacroix et al. (2007), Madani et al. (2007), and Edouard et al. (2008) all concluded that the strut or ligament diameter is the most suitable characteristic length scale of the foam microstructure, but no Reynolds number based on ligament diameter was found in the literature.

Determination of the permeability and form-drag coefficient from curve-fitting experimental data requires special care to be taken with regard to the assumptions made in modeling the flow with the Darcy-Forchheimer equation, namely, unidirectional, incompressible, steady-state flow in an isotropic porous medium with negligible

boundary effects. Bonnet et al. (2008) stated that for a porous foam to be considered homogenous, a minimum of ten pores must span each direction of the sample. They also investigated the compressibility effects of air flowing in porous metal foams and recast the Darcy-Forchheimer equation in terms of the gradient of the product of fluid density and pressure, as function of the mass-flux density of the fluid, in lieu of the superficial velocity. Many authors have used relatively thin foam samples and measured pressure gradients from two-point measurements (at the inlet and the exit of the sample). Bonnet et al. (2008) concluded that the behavior of the flow could not be properly characterized under these conditions. Very few authors have measured pressure distribution profiles in this context: those found in the literature included Beavers et al. (1973), Calmidi (1998), Zhao et al. (2001), Madani et al. (2007), and Bonnet and Topin (2008).

When assuming steady-state flow, it is important that the measured pressure profiles allow for the exclusion of non-steady entrance and exit effects from the calculation of the pressure gradient. Madani et al. (2007) found the pressure gradients in the entrance and exit regions to be higher than that in the fully developed region. Dukhan and Patel (2011) investigated the influence of the total axial length of a foam sample on the calculated values of the permeability and dimensionless form-drag coefficient. Foam-sample lengths greater than 100 cell diameters ensured that the values of these parameters were independent of the aforementioned influence. It should be noted that two-point pressure-drop data were collected, thus the above-mentioned requirement on the sample length also ensures that the entrance and exit effects on the pressure drop are minimized. Innocentini et al. (2010) investigated the effect of the length of the sample and how it is held when measuring the permeability. For highly-porous metal foams, the relative size of the sample and holder should be selected appropriately, to eliminate the presence of stagnant fluid zones and reduce the amount of radial diffusion of the fluid and underestimation of the pressure drop across the sample.

Lage et al. (2005) proposed a procedure to evaluate the permeability and dimensionless form-drag coefficient, by independently determining each term through the minimization of the pressure-drop contribution of the other. When calculating the permeability, the

viscous effect of the bounding wall of the porous medium is also isolated and subtracted from the pressure gradient. However, this study never stated a requirement on the height of the porous medium, transverse to the axial flow direction, between the two bounding walls of a rectangular or parallel-plate channel.

Dukhan and Ali (2012) determined a minimum-value requirement on the diameter of a porous-metal-foam sample, to minimize the boundary effects of the containing tube wall, in experiments for determining the permeability and form-drag coefficient. These boundary effects were minimized for sample diameters greater than or equal to 63.5 mm, equating to an approximate requirement of 15 and 30 cell diameters for the 10 PPI and 20 PPI foam samples, respectively. Of note, all fourteen ERG Aerospace aluminum foam samples used in their study were six inches long; and none of these samples met the minimum requirement for length set forth in a previous study by one of the authors [Dukhan and Patel (2011)]. Beavers et al. (1973) performed a similar experiment for beds of randomly packed spheres. The permeability and form-drag coefficient were unaffected when the equivalent hydraulic diameters of the bed were 12 times and 40 times the diameter of the spherical particles, respectively.

### 1.3.3 Fluid Flows in Adjacent Open and Porous Domains

The modeling of steady flows of incompressible Newtonian fluids in adjacent open and porous domains can be segregated into three basic levels of description: microscopic, mesoscopic, and macroscopic. The microscopic-scale description is an exact approach, in which the fluid flows in both the open and porous domains are modeled by the continuity and Navier-Stokes equations, and the no-slip boundary condition is applied at all fluid-solid boundaries. However, this approach requires an exact description of the topology of the porous medium, which poses a variety of difficulties for porous metal foams, such as the high local heterogeneity [Chandesris and Jamet (2007)]. The storage capacity and computer speed of modern computers also limits this approach, as numerical simulations at this level of complexity would require too much time to be of any practical use. The mesoscopic-scale description is a volume-averaged approach that treats the open and porous regions as one single solution domain with one set of continuity and momentum

equations to describe the fluid flow [Goyeau et al. (2003), Chandesris and Jamet (2006, 2007, 2009), Jamet and Chandesris (2009), and Jamet et al. (2009)]. This approach requires a heterogeneous transition zone to be defined in the vicinity of the interface between the open and porous domains. As outlined in Costa et al. (2008), the difficulty in this method is related to the description of such a transition zone, as it is nearly impossible to accurately (or reliably) describe the strong variations in the effective properties of the porous medium in this region. In the macroscopic-scale description, the open and porous regions are treated as two separate solution domains, each with their own set of governing equations. To couple the two domains, a suitable boundary condition is imposed at their interface. This approach is the most useful one for modeling practical problems, but it does have some difficulties related to the assigning of suitable values to the coefficients that are involved in the interfacial boundary condition [Chandesris and Jamet (2007)].

As the macroscopic-scale description is the most practical approach to modeling Newtonian fluid flows in adjacent open and porous domains, the remainder of this section is focused on the various interfacial boundary conditions available in the literature, as well as attempts at determining the various coefficients that arise in such conditions. The discussions will be limited to laminar fluid flows. For discussions on the modeling of turbulent fluid flows in adjacent open and porous domains, and the related approaches and challenges, the reader is referred to the works of Prinos et al. (2003), de Lemos and Silva (2006), McLean and Nikora (2006), Breugem et al. (2006), Chan et al. (2007), Finnigan and Shaw (2008), Saito and de Lemos (2010), Suga et al. (2010, 2011), Higashino and Stefan (2012), and de Lemos (2012).

Beavers and Joseph (1967) provided the seminal experimental and numerical research work in this area. They investigated steady Newtonian fluid flows in a uniform parallel-plate channel that was partially occupied by naturally homogenous and isotropic permeable blocks; these blocks were made from aloxite or metal foam (FOAMETAL). The flows in the adjacent open and porous domains were modeled using the continuity and Navier-Stokes, and the Darcy equation, respectively. The pressure and the normal

component of the fluid velocity were assumed to be continuous at the interface. Darcy flow was assumed, with a uniform superficial velocity prevailing in the entire porous domain up to the interface. To account for the observed boundary layer within the porous domain, a slip condition with one adjustable dimensionless coefficient was proposed to relate the velocity gradient in the open-domain side, evaluated at the interface, to the open-domain fluid velocity at the interface and the superficial velocity in the porous block. With the experimental data collected, the adjustable coefficient in the imposed slip condition was determined for each of the porous blocks. It was found that this dimensionless coefficient depends strongly on the exact location of the interface, properties of the porous medium, and the type of flow regime encountered [Kaviany (1995), Goyeau et al. (2003), Chandesris (2006, 2007)].

Neale and Nader (1974) modeled the flow in the open domain using the continuity and Navier-Stokes equations, and the Brinkman-extended Darcy equation for the flow within the porous domain. The velocity and also the normal and tangential components of the stress, based on the dynamic viscosity of the fluid in the open domain and an effective viscosity in the porous domain, were assumed to be continuous at the interface. They argued that the Brinkman term would implicitly resolve the boundary layer within the porous medium and remove the necessity of the velocity slip condition. Their solution matched that of Beavers and Joseph (1967), and it also had the advantage of describing the boundary layer within the porous domain. By comparing the two solutions, the coefficient in the slip condition of Beavers and Joseph (1967) was found to be equal to the square-root of the ratio of the effective dynamic viscosity to dynamic viscosity of the fluid. The difficulty involved with the model proposed by Neale and Nader (1974) is related to the determination of a suitable effective dynamic viscosity.

Vafai and Kim (1990) presented an analytical solution to the problems of interest, modeling the fluid flow in the open domain using the continuity and Navier-Stokes equations, and the Brinkman-Darcy-Forchheimer equation for the fluid flow within the porous domain. The effective dynamic viscosity was assumed to be equal to the dynamic viscosity of the fluid, and the velocities and the gradients of the velocity in the open and

porous domains were assumed to be continuous at the interface. They also discussed how the velocity profile was affected by changes in the Darcy number and product of the Reynolds number with a specially defined inertial parameter.

Ochoa-Tapia and Whitaker (1995a) modeled the flow in the open domain with the continuity and Stokes equations, and the extended Brinkman-Darcy equation in the porous domain, with the effective dynamic viscosity equal to the dynamic viscosity of the fluid divided by the porosity. They proposed a continuous velocity field at the interface and an interfacial tangential stress-jump condition, based on the excess viscous stress at the interface, which involved one dimensionless adjustable coefficient of order unity. In the second part of their study, Ochoa-Tapia and Whitaker (1995b) compared their theoretical model to the experimental data of Beavers and Joseph (1967) for the determination the aforementioned dimensionless coefficient. A variable-porosity model of the interface region was also investigated, as an alternative to the stress-jump condition, but it did not produce results that matched the experimental data. Although they successfully determined that the adjustable dimensionless coefficient is of order one, they could not deduce an empirical relationship for this coefficient. Ochoa-Tapia and Whitaker (1998) included inertial terms in their derivations. The continuity and Navier-Stokes equations were used to model the fluid flow in the open domain, and the Brinkman-Darcy-Forchheimer equation was employed to model the fluid flow in the porous domain. The interfacial stress-jump boundary condition was revisited, and an additional term was added to account for the excess inertial stress; it too contained a dimensionless adjustable coefficient of order one or less. In both studies, it was stated that experimental data should be used to determine these dimensionless coefficients.

Alazmi and Vafai (2001) discussed four interfacial heat-transfer conditions, and five of the aforementioned interfacial boundary conditions for fluid flows in adjacent open and porous domains. They compared and contrasted the effects of modifying a variety of parameters, namely, the Darcy number, an inertia parameter, Reynolds number, porosity, effective viscosity, and slip coefficients, on the velocity field, temperature field, and Nusselt number distribution. It was found that the effects of varying these parameters had

a much greater effect on the velocity field than on either the temperature field or Nusselt number distribution. Changing the effective dynamic viscosity from the dynamic viscosity of the fluid to a recommended value given by Givler and Altobelli (1994) had a relatively minimal effect on the velocity field, given that the range of values for the effective dynamic viscosity was quite wide. Following the analysis of Vafai and Tien (1981), the authors recommended that the effective dynamic viscosity be set equal to the dynamic viscosity of the fluid divided by the porosity.

Deng and Martinez (2005) also expressed the need for accurate determination of the dimensionless coefficient found in the interfacial conditions, to obtain meaningful solutions to the problems of interest. They used two different approaches to obtain an estimate of the value of the dimensionless coefficient in the stress-jump condition of Ochoa-Tapia and Whitaker (1995a). One was the two-domain macroscopic approach with the continuity and Navier-Stokes equations in the open domain, the extended Brinkman-Darcy equation in the porous domain, and the interfacial boundary condition of Ochoa-Tapia and Whitaker (1995a). In the second approach, a single-domain model was used. With each solution producing similar results, the dimensionless coefficient was estimated using a curve-fitting method. It was found that this coefficient was a function of the Reynolds number and the Darcy number, and it was of order one.

Kuznetsov (1997, 1999) extended the analytical approach provided in Vafai and Kim (1990) by incorporating the stress-jump condition of Ochoa-Tapia and Whitaker (1995a), and an effective dynamic viscosity, rather than using the continuity of the gradient of the velocity as an interfacial boundary condition. His analytical solution included the effective dynamic viscosity, and it was demonstrated that the selection of the value of this term, as well as the value of the stress-jump coefficient, could affect the velocity profile. This effect was also found to decrease with an increase in the inertial parameter, and decrease in Darcy number.

Costa et al. (2008) numerically investigated laminar fluid flows in the problems of interest. They modeled the fluid flow in the open domain with the continuity and Navier-

Stokes equations, the fluid flow in the porous domain with the Brinkman-Darcy-Forchheimer equation, and the interfacial boundary condition with the stress-jump condition of Ochoa-Tapia and Whitaker (1998). The mathematical model was solved with a control-volume finite-element method (CVFEM), and they proposed a novel procedure to implement the stress-jump condition. To validate their procedure, they compared their results with an adapted version of the analytical solution of Kuznetsov (1999) to include the second coefficient in the tangential stress-jump condition. The values of the two adjustable coefficients in the tangential stress-jump condition were varied, and their effect on the flow field was found to be significant. They concluded that for accurate numerical predictions, experimental data is required to determine these stress-jump coefficients.

A number of numerical investigations have been devoted to the evaluation of the aforementioned coefficients in the interfacial boundary conditions. Nabovati and Sousa (2007) used the lattice-Boltzmann method to investigate the flow characteristics at the interface, demonstrated that the Beavers and Joseph (1967) slip coefficient was a function of porosity, and proposed an equation to model this slip coefficient. Valdés-Parada et al. (2009) derived an analytical expression for the coefficient in the stress-jump condition put forward by Ochoa-Tapia and Whitaker (1995a), by combining ideas borrowed from the analyses of Goyeau et al. (2003) and Valdés-Parada et al. (2007).

Other than the seminal work of Beavers and Joseph (1967), there have been only a few experimental studies of fluid flows in adjacent open and porous domains. Beavers et al. (1970) performed an experimental investigation and collected pressure-drop data for laminar and turbulent fluid flows in a parallel-plate channel that contained adjacent open and porous-metal-foam domains (FOAMETAL). Their data validated the use of a velocity-slip model and indicated that the metal foam delayed the laminar-to-turbulent transition in the open domain, as determined from flow visualizations. The transitional Reynolds number, based on the hydraulic diameter of the parallel-plate channel, was found to be between 2765 and 3150.

Prinos et al. (2003) have experimentally (and also numerically) studied the characteristics of the turbulent flow of water in open channels with a porous bed. The porous bed was made up of a bundle of cylindrical rods, and their diameter and spacing were adjusted to achieve values of permeability ranging from $5.5490 \times 10^{-7}$ $m^2$ to $4.1070 \times 10^{-4}$ $m^2$ and porosity values from 0.4404 to 0.8286. Hot-film anemometry was used for measuring mean velocities and turbulent stresses in the channel, with a bed-porosity value of 0.8286. Emphasis was put on determining the effect the Darcy number had on the flow properties over and within the porous region. The velocities in the open domain were found to decrease with increasing values of Darcy number, due to the strong momentum exchange near the open-porous interface and the corresponding penetration of turbulence into the porous layer for highly permeable beds.

Arthur et al. (2009) took particle-image velocimetry (PIV) measurements to investigate the velocity profile of pressure-driven fluid flows in various models of porous media. Installed in a rectangular channel, the porous medium consisted of arrays of circular acrylic rods, positioned to create porosities ranging from 0.01 to 0.49. One of the models investigated involved flows with an open domain above the rods. The velocity profile near the interface was fitted with a fourth-order least-squares curve fit, and the gradient of the velocity was found from differentiating this curve fit. Such measurements could be used for validating the results of corresponding numerical predictions and determining the coefficients in the interfacial boundary condition.

Carotenuto et al. (2012) induced a shear-driven flow above and below a porous medium via a rotational rheometer to mimic a parallel-plate configuration. Sand papers of two different grits were used and considered as very thin porous media. Shear-induced flow above the porous medium allowed for determination of the velocity profile in the open domain as well as the fluid velocity at the interface. Flow induced from below directly determined the stress transferred through the porous layer to the fluid in the open domain, as well as the fluid velocity in the porous layer. For the finer-grit sandpaper, it was found that the stress transferred to the fluid within the open domain was smaller than the applied stress, but this difference was within the experimental error bounds.

With the relative dearth of experimental studies of fluid flow in adjacent open and porous domains, there is an explicit need for accurate measurements of data required for determining the two adjustable coefficients in the tangential stress-jump condition of Ochoa-Tapia and Whitaker (1998), and also for the checking and refining numerical simulations of such fluid flows. This need is even more urgent for flows in adjacent open and porous-metal-foam domains, as there appear to be no experimental studies of such flows in the published literature, except for the work of Beavers and Joseph (1967) and Beavers et al. (1970) to the best knowledge of the author.

## 1.4 Organization of the Thesis

In the earlier sections of this chapter (Chapter 1), the motivation and overall goals, specific objectives, and a literature review on topics relevant to this research were presented. In Chapter 2, the theoretical considerations that were used for designing the experimental set-ups and procedures, implementing (selecting, calibrating, and benchmarking) related instrumentation, and processing the experimental measurements are presented and discussed. Descriptions of the experimental apparatus and procedures proposed and used in this work are given in Chapter 3. In Chapter 4, the results are presented and discussed. Chapter 5 concludes the main body of this thesis, and contains a review of the thesis, a summary of the main contributions of this work, and also recommendations for extensions of this work.

# Chapter 2 – Theoretical Considerations

As was stated in Chapter 1, the focus of the work reported in this thesis was on experimental investigations of Newtonian fluid flows through straight rectangular ducts, with cross-sections of large aspect ratio (so the central regions of these ducts are akin to a parallel-plate channel) that were either entirely open (containing no porous medium), completely filled with a porous medium, or contained adjacent open and porous domains with a distinct interface parallel to the top and bottom walls. A longitudinal cross section of such a duct containing adjacent open and porous domains is illustrated in Figure 2.1. The porous media considered in this work were all porous metal foams.

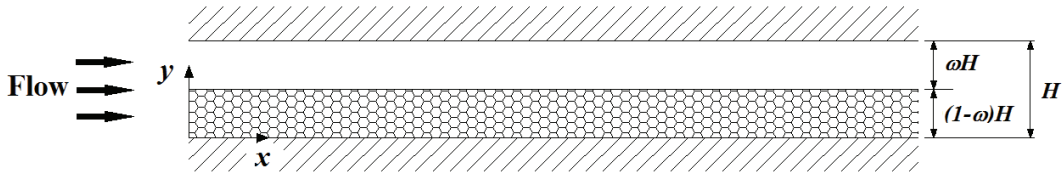


Figure 2.1: Schematic illustration of the longitudinal cross-section of a straight rectangular duct containing adjacent open and porous domains, and related notation

In this chapter, the theoretical considerations that were used in this work for designing the experimental set-ups and procedures, implementing (selecting, calibrating, and benchmarking) related instrumentation, and processing the experimental measurements are presented and discussed concisely. First, the assumptions invoked in the adopted mathematical models of fluid flows in the problems of interest are outlined. Then, the equations that govern Newtonian fluid flows in the open and porous domains within straight rectangular ducts are discussed, and the corresponding boundary conditions at solid (impermeable) walls and at the interface between the open and porous domains are presented. Following that, an analytical solution to the mathematical model of laminar, fully developed, Newtonian fluid flow through the adjacent open and porous domains (see Figure 2.1) is presented. This analytical solution was adapted from the works of Kuznetsov (1999) and Costa et al. (2008). Then, four different approaches for curve-fitting experimental data and determining the permeability and dimensionless form-drag

coefficient for flows through the porous metal foams are proposed and discussed. The definitions of several pertinent friction factors are then presented, along with analytical solutions (when possible) or empirical correlations (when available).

## 2.1 Assumptions

The following assumptions were invoked in the adopted mathematical models of fluid flows in adjacent and porous domains (see schematic in Figure 2.1):

- The same Newtonian fluid saturates both the open and porous domains
- Steady-state (statistically) conditions prevail
- The fluid is incompressible and isothermal, thus, its mass density and dynamic viscosity, evaluated at mean values of temperature and pressure in the region of interest, are constants throughout the open and porous domains. Furthermore, fully developed fluid flow prevails.
- The open and porous domains are separated by a sharp interface parallel to the bottom and top walls, and the location of this interface is known *a priori*
- The porous medium (metal foams investigated in this work) is homogenous and isotropic. In particular, the porosity and permeability of the porous metals foams are uniform and constant throughout, from the bottom wall of the channel right up to the interface between the open and porous domains.

## 2.2 Governing Equations and Boundary Conditions

The full unsteady, three-dimensional equations that govern the Newtonian fluid (air) flows considered in this work, in both the adjacent open and porous domains, are the continuity and Navier-Stokes equations [Batchelor (1967); White (1991)]. As was discussed in Section 1.3.3, the macroscopic approach is the most practical and effective way of the modeling fluid flows in adjacent open and porous domains, and this approach is adopted in this work. In this approach, the fluid flow in the open domain is modeled using the above-mentioned the continuity and Navier-Stokes equations, and in the porous domain, the volume-averaged forms of these equations are used.

### 2.2.1 Volume-Averaged Continuity and Momentum Equations

In this approach, the porous domain is treated as a continuum, in which the dependent variables of interest are averaged over a representative elementary volume (r.e.v), shown schematically in Figure 2.2 [Nield and Bejan (2013)].

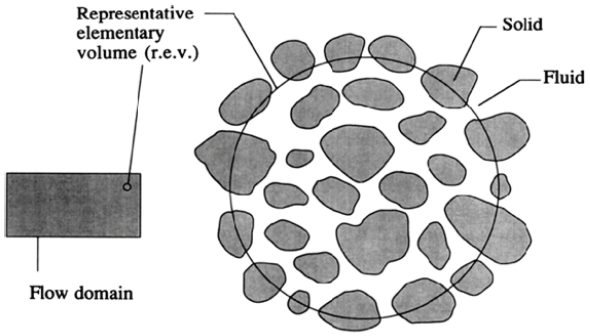


Figure 2.2: A representative elementary volume [Nield and Bejan (2013)]

The selected size of the r.e.v. (see Figure 2.2) is such that it is small compared to the overall dimensions of the problem of interest, but large enough to yield statistically meaningful local averages of the dependent variables. For complete derivations of the volume-averaged forms of the governing continuity and Navier-Stokes equations, the reader is referred to the work of Whitaker (1999). Two types of average values are considered for any physical variable, $\psi$ : the phase-average (further referred to as the superficial average), denoted by $\langle\psi\rangle$; and the intrinsic-phase-average (also referred to as the intrinsic-average), denoted by $\langle\psi\rangle^f$ . These averages are defined as follows:

$$\langle\psi\rangle = \frac{1}{V}\int_{V_f}\psi dV \;\; ; \;\; \langle\psi\rangle^f = \frac{1}{V_f}\int_{V_f}\psi dV \tag{2.1}$$

In Eq. 2.1, $V$ represents the volume of the r.e.v.; and $V_f$ represents the volume of the fluid phase contained within $V$ . The phase-average is related to the intrinsic-phase-average using the porosity, $\varepsilon$ , by the Dupuit-Forchheimer relation [Nield and Bejan (2013)], as shown in the equation:

$$\langle \psi \rangle = \varepsilon \langle \psi \rangle^{f} \quad ; \quad \varepsilon = V_f / V \tag{2.2}$$

Using Eq. 2.2, and invoking the assumption of constant fluid properties, the volume-averaged continuity and the Navier-Stokes equations within the porous medium, in terms of intrinsic-phase-average quantities, can be cast in the following forms, respectively:

$$\frac{\partial}{\partial x_i}\left(u_i\right) = 0 \tag{2.3}$$

$$\rho\left(\frac{1}{\varepsilon}\frac{\partial}{\partial t}\left(u_i\right) + \frac{1}{\varepsilon^2}\frac{\partial}{\partial x_j}\left(u_i u_j\right)\right) = -\frac{\partial p}{\partial x_i} + \frac{\mu}{\varepsilon}\frac{\partial^2 u_i}{\partial x_j^2} - \left(\frac{\mu}{K} + \frac{\rho c_F}{\sqrt{K}}\left\|\boldsymbol{v}\right\|\right)u_i \tag{2.4}$$

In these equations, for simplicity of notation, the superficial velocity vector is denoted by $\boldsymbol{v}$, its components in the Cartesian coordinate directions are denoted by $u_i$ and $u_j$, in the $i$ and $j$ directions, respectively; $p$ is used to denote the intrinsic-phase-average static pressure of the fluid; $\rho$ is the density of the fluid; $\mu$ is the dynamic viscosity of the fluid; $K$ is the intrinsic permeability of the porous medium (hereafter referred to simply as the permeability); and $c_F$ is the dimensionless form-drag coefficient (also referred to as the Forchheimer coefficient in the literature). It should be noted here that traditionally, the $\mu/\varepsilon$ term was not used; rather, the so-called Brinkman dynamic viscosity of the fluid, $\mu_B$, or effective dynamic viscosity of the fluid, $\mu_{eff}$, was used in its place [Nield and Bejan (2013)], and it was thought that $\mu_B$ needed to be determined from experimental data. However, Whitaker (1999) did a rigorous derivation of the volume-averaged equations, and showed that it was, indeed, correct to use $\mu/\varepsilon$ in the volume-averaged momentum equations. It should also be noted that the time-derivative term in Eq. 2.4 is zero under steady-state conditions.

### 2.2.2 Boundary Conditions at Solid Walls

With respect to the schematic in Figure 2.1, at the inner surfaces of the bottom and top walls of the duct, the no-slip and impermeability conditions apply:

$$\text{at } y = 0,\ u_1, u_2, u_3 = 0\ ;\ \text{and at } y = H,\ u_1, u_2, u_3 = 0 \tag{2.5}$$

## 2.3 Conditions at the Interface Between the Open and Porous Domains

At the interface between the open and porous domains, the normal and tangential components of the fluid velocity, the static pressure in the open domain and the intrinsic-phase-average pressure in the porous domain, and the normal stresses in the open and porous domains (indicated by the subscripts '*od*' and '*pd*', respectively) are assumed to be continuous [Nield and Bejan (2013)], as expressed below in Eq. 2.6, with the total stress tensor given by Eq. 2.7:

$$\left(v\right)_{od}^{I} = \left(v\right)_{pd}^{I}\ ;\ \left(p\right)_{od}^{I} = \left(p\right)_{pd}^{I}\ ;\ \left(n_j n_i \sigma_{ij}\right)_{od}^{I} = \left(n_j n_i \sigma_{ij}\right)_{pd}^{I} \tag{2.6}$$

$$\left(\sigma_{ij}\right) = \mu\left(\frac{\partial u_i}{\partial x_j} + \frac{\partial u_j}{\partial x_i}\right) - p\delta_{ij} \tag{2.7}$$

The notation used in Eqs. 2.6 and 2.7 is borrowed from Costa et al. (2008): the first-order tensor $n_i$ (or $n_j$) is a unit vector normal to the interface; $\delta_{ij}$ is the Kronecker delta function; the components of the total stress tensor, $\sigma_{ij}$, in the open domain are calculated from the static pressure and the components of the fluid velocity in the open domain, whereas, in the porous domain they are calculated from the intrinsic-phase-average static pressure and the components of the superficial velocity; and the superscript '*I*' indicates conditions at the interface between the open and porous domains.

Following the arguments put forward by Ochoa-Tapia and Whitaker (1998), if the porosity, $\varepsilon$, and the permeability, $K$, of the porous medium are assumed to be uniform throughout it, right up to the interface between the open and porous domains, then the implied excess tangential stress at the interface has to be accounted for by the interfacial condition presented in the following equation:

$$\left[\frac{\mu}{\varepsilon}\left(\frac{\partial u_t}{\partial n}\right)_{pd} - \mu\left(\frac{\partial u_t}{\partial n}\right)_{od}\right]^I = \left[\beta_1 \frac{\mu}{\sqrt{K}} u_t + \beta_2 \rho u_t^2\right]^I \tag{2.8}$$

In this equation, $u_t$ is the absolute value of the component of the fluid velocity tangential to the interface; $n$ is a local coordinate normal to the interface and points from the porous domain to the open domain; and $\beta_1$ and $\beta_2$ are adjustable coefficients connected to the implied excess viscous stress and the implied excess inertial stress, respectively, at the interface. As is discussed in Ochoa-Tapia and Whitaker (1995b, 1998), the two adjustable coefficients in the interfacial boundary condition expressed in Eq. 2.8 are of order unity or less and are to be determined using experimental data.

## 2.4 Analytical Solution to the Problems of Interest for Laminar Flows

The problems of interest (see Figure 2.1) are akin to that considered in the now classical investigation of Beavers and Joseph (1967). In the experimental investigation, straight rectangular ducts with cross-sections of high aspect ratio ($W_{channel} / H$, where $H$ is the total height and $W_{channel}$ is the width of the duct cross-section) were used (related details are provided in Chapter 3), and they contained the adjacent open and porous domains. In the central portion of these rectangular ducts, because of the high-aspect ratio of their cross section, the fluid flow was, for all practical purposes, similar to that in a parallel-plate channel containing adjacent open and porous domains, akin to that illustrated in Figure 2.1. Also shown in this figure is the following notation: $H$, $\omega H$, and $(1-\omega)H$ are the total, open-domain, and porous-domain heights; and $\omega$ is the ratio of the open-domain height to the total-channel height.

An analytical solution can be now obtained by invoking the following assumptions, in addition to those in Section 2.1 [Kuznetsov (1999); Costa et al. (2008)]:

- The interface between the open and porous domains is flat and parallel to the top and bottom walls of the channel
- Fluid flow is steady and laminar

- Fully developed flow prevails: thus, the velocity component in the $y$ direction, $v$, is zero; the velocity in the $x$ direction, $u$, is invariant in this direction and is only a function of the $y$ coordinate; $(\partial p / \partial y) = 0$ throughout the region of interest; and $(dp / dx) =$ constant.

Here, $u$ and $v$ are the actual velocity components in the open domain, and they represent the corresponding components of the superficial velocity inside the porous domain; and $p$ is the actual static pressure in the open domain, and it denotes the intrinsic-phase-average static pressure of the fluid inside the porous domain.

At this stage, $H$ and $U = \left(-dp/dx\right)\left(H^2/\mu\right)$ are taken as the reference length and velocity, respectively, and the following dimensionless variables and parameters are introduced, following Costa et al. (2008): $u_* = u/U$; $y_* = y/H$; $\mathrm{Re} = \rho UH/\mu$, which is the Reynolds number based on $U$ and $H$; and $Da = K/H^2$, which is the Darcy number. In the context of the assumptions introduced above and the aforementioned dimensionless variables and parameters, the $x$-direction momentum equations in the open and porous domains can be cast in the following dimensionless forms, respectively:

$$0 = 1 + \frac{d}{dy_*}\left(\frac{du_*}{dy_*}\right) \tag{2.9}$$

$$0 = 1 + \frac{d}{dy_*}\left(\frac{1}{\varepsilon}\frac{du_*}{dy_*}\right) - \left(\frac{c_F \,\mathrm{Re}\,|u_*|}{\sqrt{Da}} + \frac{1}{Da}\right)u_* \tag{2.10}$$

The dimensionless form of the stress-jump condition at the interface between the open and porous domains is the following:

$$\left[\frac{1}{\varepsilon}\left(\frac{du_*}{dy_*}\right)_{pd} - \left(\frac{du_*}{dy_*}\right)_{od}\right]^I = \left[\beta_1 \frac{1}{\sqrt{Da}}u_* + \beta_2 \,\mathrm{Re}\,u_*^2\right]^I \tag{2.11}$$

In Eq. 2.11, $y_*$ is the dimensionless coordinate normal to the interface and points from the porous domain to the open domain.

An analytical solution can be derived for the dimensionless velocity field, $u_*$, by making the following assumptions: two boundary layers exist within the porous domain, one adjacent to the interface, located at $y_* = (1-\omega)$, and the other one next to the bottom wall of the channel, located at $y_* = 0$; and these two boundary layers merge in the central region of the porous domain, where $du_*/dy_* = 0$. With these assumptions, Eq. 2.10 reduces to a simple quadratic algebraic equation in the central portion of the porous domain (where $du_*/dy_* = 0$), and the positive root of this quadratic equation is the solution for the dimensionless velocity in this region, $u_* = u_{\infty *}$:

$$u_{\infty *} = \frac{-1+\sqrt{1+4Da^2F}}{2DaF}; \qquad F = \frac{c_F \,\mathrm{Re}}{\sqrt{Da}} \tag{2.12}$$

The dimensionless velocity field within the boundary layer near the bottom wall can now be obtained by integrating Eq. 2.10 with respect to $y_*$, subject to the following boundary conditions: $u_* = 0$ at $y_* = 0$; and $u_* = u_{\infty *}$ where the two boundary layers merge; and noting that $du_*/dy_* = 0$ where the two boundary layers merge, $u_{\infty *}$ can be determined. This solution is represented by the following set of equations:

$$u_* = \left(u_{\infty *} + u_{1*}\right)\left(\frac{z_1 - 1}{z_1 + 1}\right)^2 - u_{1*}$$

$$u_{1*} = 2u_{\infty *} + \frac{3}{2DaF}; \qquad z_1 = A\exp\left(By_*\right) \tag{2.13}$$

$$A = \frac{1+\alpha_1}{1-\alpha_1}; \qquad B = \sqrt{\frac{2\varepsilon F\left(u_{\infty *} + u_{1*}\right)}{3}}; \qquad \alpha_1 = \sqrt{\frac{u_{1*}}{u_{\infty *} + u_{1*}}}$$

The dimensionless velocity field within the boundary layer adjacent to the interface can be obtained by integrating Eq. 2.10 with respect to $y_*$, subject to the following boundary conditions: $u_* = u_*^I$ at $y_* = (1-\omega)$ ; and $u_* = u_{\infty *}$ and $du_*/dy_* = 0$ where the two boundary layers merge. The solution is represented by the following set of equations:

$$u_* = \left(u_{\infty *} + u_{1*}\right)\left(\frac{1-z_2}{1+z_2}\right)^2 - u_{1*}$$
$$z_2 = C\exp\left[B\left(y_* - 1 + \omega\right)\right]; \quad C = \frac{1-\alpha_2}{1+\alpha_2}; \quad \alpha_2 = \sqrt{\frac{u_*^I + u_{1*}}{u_\infty + u_{1*}}} \tag{2.14}$$

In the open domain, the solution for the dimensionless velocity field can be obtained by integrating Eq. 2.9 with respect to $y_*$, subject to the following boundary conditions: $u_* = 0$ at $y_* = 1$; and $u_* = u_*^I$ at $y_* = (1-\omega)$. The solution is the following:

$$u_* = -0.5\left(1-y_*\right)^2 + \left[\left(\frac{u_*^I}{\omega}\right) + 0.5\omega\right]\left(1-y_*\right) \tag{2.15}$$

In the experimental investigation undertaken in this work, values of the shear stress at the upper wall of the open domain, $\tau_{od}^{UW}$, located at $y = H$, and the pressure gradient, $dp/dx$, in the fully developed region were measured. Using these measurements, the dimensions of the open and porous domains of the channel, and an overall force balance on the open domain (from the interface between the open and porous domains to the inner surface of the upper wall), the open-domain shear stress at the interface, $\tau_{od}^I$, can be calculated using the following equation:

$$\tau_{od}^I = (-dp/dx)\omega H - \tau_{od}^{UW} \tag{2.16}$$

It should be noted that this equation applies to not only laminar flows, but also turbulent flows in a time-averaged sense.

Then, using the measured values of $\tau_{od}^{UW}$, $dp/dx$, the dimensions of the open and porous domains, and the calculated value of $\tau_{od}^{I}$, the following dimensionless quantities can be calculated using Eqs. 2.12 to 2.15: the dimensionless velocity in the central region of the porous domain, $u_{\infty *}$; the dimensionless variable $u_{1*}$; and the dimensionless quantities *B* and *C*. After that, the following equations can be used to calculate the dimensionless velocity at the interface, $u_{*}^{I}$, and the dimensionless velocity gradients at the interface in the open and porous domains, $(du_{*}/dy_{*})_{od}^{I}$ and $(du_{*}/dy_{*})_{pd}^{I}$, respectively:

$$\begin{aligned} u_{*}^{I} &= [0.5\omega^{2} - \overline{\tau}_{od}^{I}\omega / \{(-dp/dx)H\}] \\ (du_{*}/dy_{*})_{od}^{I} &= [0.5\omega - (u_{*}^{I}/\omega)] \\ (du_{*}/dy_{*})_{pd}^{I} &= -\frac{4(u_{\infty *} + u_{1*})}{(1+C)^{3}}(1-C)CB \end{aligned} \tag{2.17}$$

After the above-mentioned calculations, the terms $Y_{interface}$ and $X_{interface}$ in the following the dimensionless form of the interfacial stress-jump condition can be calculated:

$$\begin{aligned} Y_{interface} &= \left[\frac{1}{\varepsilon}\left(\frac{du_{*}}{dy_{*}}\right)_{pd}^{I} - \left(\frac{du_{*}}{dy_{*}}\right)_{od}^{I}\right] \Bigg/ \left[\frac{1}{\sqrt{Da}}u_{*}^{I}\right] \\ X_{interface} &= \left[\mathrm{Re}\left(u_{*}^{I}\right)^{2}\right] \Bigg/ \left[\frac{1}{\sqrt{Da}}u_{*}^{I}\right] \\ Y_{interface} &= \beta_{1} + X_{interface}\beta_{2} \end{aligned} \tag{2.18}$$

Thus, from each set of experimental measurements corresponding to laminar flow in the channel with adjacent open and porous domains, the corresponding set of terms $Y_{interface}$ and $X_{interface}$ in Eq. 2.18 can be obtained. Then, a least-squares linear-curve-fit to these pairs of terms ($Y_{interface}$ and $X_{interface}$) can be done, and the intercept and the slope of this linear-curve-fit gives the stress-jump coefficients $\beta_1$ and $\beta_2$.

## 2.5 Determination of the Permeability and Form-Drag Coefficient

The permeability and dimensionless form-drag coefficient are two parameters that are critically important for modeling fluid flow through a porous medium. As was discussed in Section 1.3.2, a number of semi-empirical correlations for determining these two parameters for porous metal foams akin to the ones used in the present work are available in the literature. Although such semi-empirical correlations are desirable from a practical point of view, they are usually not generally applicable, even for the same batch of porous metal foams. The reason for this lack of generality is that porous metal foams with the same nominal PPI designation and bulk density, and made by the same manufacturer, can have significantly different geometric characteristics, due to inevitable differences incurred in the foam topology during the manufacturing process [Moreira et al. (2004); Edouard et al. (2008)].

Thus, whenever possible, the permeability and dimensionless form-drag coefficient should be determined experimentally, directly with the porous metal foam to be used in the application of interest or with a sample cut from this particular metal foam. This is the approach that was adopted in this work. The specific experimental set-up involved measurements related to fully developed Newtonian fluid flow in a straight rectangular duct with a high-aspect-ratio cross-section filled completely with the porous metal foam of interest, in a set-up that was akin to that illustrated schematically in Figure 2.1, but with $\omega = 0$. With this set-up, the following assumptions were invoked:

- The porous metal foam is homogenous and isotropic
- The Newtonian fluid saturates the entire porous metal foam that is filled inside the rectangular duct
- Steady-state (statistically) conditions prevail
- The fluid is incompressible and isothermal, thus, its mass density and dynamic viscosity, evaluated at mean values of temperature and pressure in the region of interest, are constants throughout the open and porous domains.
- The pressure drop in the fluid flow is caused primarily by the effects of the Darcy and Forchheimer terms within the porous medium; or, in other words, the contributions of

the Brinkman term (within the porous medium and also at the walls of the duct) to this pressure drop are negligibly small

- The fluid flow is fully developed and one-dimensional in the region where the measurements are made

With the above-mentioned assumptions, Eq. 2.4 reduces to the following simple form:

$$-\frac{dp}{dx} = \frac{\mu}{K}u + \frac{\rho c_F}{\sqrt{K}}u^2 \tag{2.19}$$

In Eq. 2.19, $u$ denotes the superficial velocity and it is effectively constant in the region of interest (equal to the average value of the superficial velocity in the rectangular duct, in the region where the experimental measurements are made); and $dp/dx$ is the axial gradient of the pressure, and it too is constant in the region of interest. Thus, with experimental data for $u$ and $dp/dx$, and also the corresponding values of $\mu$ and $\rho$, the values of the permeability, $K$, and dimensionless form-drag coefficient, $c_F$, can be determined. In the following subsections, four different approaches in analyzing the experimental data for the determination of $K$ and $c_F$ are presented along with related comments. Experimental uncertainties in the values of $K$ and $c_F$ were determined following the methods outlined in Kline-McClintock (1953).

### 2.5.1 Approach 1

In this approach, which is the one that is most commonly used in the literature, $N$ pairs of experimental data points $\{ u_i , (dp/dx)_i \}$ and overall average values (over all experimental runs) of the mass density and dynamic viscosity of the fluid, $\rho_{av}$ and $\mu_{av}$, respectively, are used in a least-squares quadratic-curve-fit (or regression analysis), passing through the origin (0,0), to determine the values of the permeability, $K$, and the dimensionless form-drag coefficient, $c_F$, as described, for example, in Antohe et al. (1997). This approach is represented mathematically in the following set of equations:

$$a \triangleq \frac{\mu_{av}}{K};\;\; b \triangleq \rho_{av} \cdot \frac{c_F}{\sqrt{K}};\;\; \zeta_i \triangleq \left(-\frac{dp}{dx}\right)_i;\;\; Denom = \left(\sum_{i=1}^{N} u_i^2\right)\left(\sum_{i=1}^{N} u_i^4\right) - \left(\sum_{i=1}^{N} u_i^3\right)^2$$

$$a = \left[\left(\sum_{i=1}^{N} u_i \zeta_i\right)\left(\sum_{i=1}^{N} u_i^4\right) - \left(\sum_{i=1}^{N} u_i^2 \zeta_i\right)\left(\sum_{i=1}^{N} u_i^3\right)\right] \Big/ \left[Denom\right] \tag{2.20}$$

$$b = \left[\left(\sum_{i=1}^{N} u_i^2 \zeta_i\right)\left(\sum_{i=1}^{N} u_i^2\right) - \left(\sum_{i=1}^{N} u_i \zeta_i\right)\left(\sum_{i=1}^{N} u_i^3\right)\right] \Big/ \left[Denom\right]$$

Once $a$ and $b$ in the above set of equations are computed using the aforementioned experimental data, $K$ and $c_F$ can be obtained using the following equations: $K = \mu_{av} / a$ and $c_F = b\sqrt{K} / \rho_{av}$.

### 2.5.2 Approach 2

This approach is suggested in this work as a possible improvement of the above-mentioned Approach 1. In this approach (Approach 2), $N$ sets of experimental data points and values of the fluid mass density and dynamic viscosity for the corresponding experimental runs (calculated at the mean values of the temperature and pressure for each particular experimental run), $\{u_i$, $(dp/dx)_i$, $\rho_i$, and $\mu_i\}$, are used in a least-squares quadratic-curve-fit (or regression analysis), passing through the origin (0,0), to determine the values of the permeability, $K$, and the dimensionless form-drag coefficient, $c_F$. This approach is represented mathematically in the following set of equations:

$$a \triangleq \frac{1}{K};\;\; b \triangleq \frac{c_F}{\sqrt{K}};\;\; \zeta_i \triangleq \left(-\frac{dp}{dx}\right)_i$$

$$Denom = \left(\sum_{i=1}^{N} \mu_i^2 u_i^2\right)\left(\sum_{i=1}^{N} \rho_i^2 u_i^4\right) - \left(\sum_{i=1}^{N} \mu_i \rho_i u_i^3\right)^2$$

$$a = \left[\left(\sum_{i=1}^{N} \mu_i u_i \zeta_i\right)\left(\sum_{i=1}^{N} \rho_i^2 u_i^4\right) - \left(\sum_{i=1}^{N} \rho_i u_i^2 \zeta_i\right)\left(\sum_{i=1}^{N} \mu_i \rho_i u_i^3\right)\right] \Big/ \left[Denom\right] \tag{2.21}$$

$$b = \left[\left(\sum_{i=1}^{N} \rho_i u_i^2 \zeta_i\right)\left(\sum_{i=1}^{N} \mu_i^2 u_i^2\right) - \left(\sum_{i=1}^{N} \mu_i u_i \zeta_i\right)\left(\sum_{i=1}^{N} \mu_i \rho_i u_i^3\right)\right] \Big/ \left[Denom\right]$$

Once $a$ and $b$ in the above set of equations are computed using the aforementioned experimental data, $K$ and $c_F$ can be obtained using the following equations: $K = 1/a$ and $c_F = b\sqrt{K}$.

### 2.5.3 Approach 3

In this approach, Eq. 2.19 is divided by product of the superficial velocity and the dynamic viscosity of the fluid, and recast as follows:

$$\left(-\frac{dp}{dx}\right)\left(\frac{1}{\mu u}\right) = \frac{1}{K} + \frac{\rho c_F}{\mu\sqrt{K}}u \tag{2.22}$$

With this form of the equation and $N$ sets of experimental data points and values of the fluid mass density and dynamic viscosity for the corresponding experimental runs, $\{u_i$, $(dp/dx)_i$, $\rho_i$, and $\mu_i\}$, a least-squares linear-curve-fit can be used to determine the permeability, $K$, and the dimensionless form-drag coefficient, $c_F$. This approach is represented by the following set of equations:

$$\begin{aligned}
a \triangleq \frac{1}{K};\ b \triangleq \frac{c_F}{\sqrt{K}};\ x_i \triangleq \frac{\rho_i u_i}{\mu_i};\ y_i \triangleq \left(-\frac{dp}{dx}\right)_i\left(\frac{1}{\mu_i u_i}\right) \\
Denom = N\left(\sum_{i=1}^{N} x_i^2\right) - \left(\sum_{i=1}^{N} x_i\right)^2 \\
a = \left[\left(\sum_{i=1}^{N} x_i^2\right)\left(\sum_{i=1}^{N} y_i\right) - \left(\sum_{i=1}^{N} x_i\right)\left(\sum_{i=1}^{N} x_i y_i\right)\right] \Big/ \left[Denom\right] \\
b = \left[N\left(\sum_{i=1}^{N} x_i y_i\right) - \left(\sum_{i=1}^{N} x_i\right)\left(\sum_{i=1}^{N} y_i\right)\right] \Big/ \left[Denom\right]
\end{aligned} \tag{2.23}$$

Once $a$ and $b$ in the above set of equations are computed using the aforementioned experimental data, $K$ and $c_F$ can be obtained using the following equations: $K = 1/a$ and $c_F = b\sqrt{K}$.

### 2.5.4 Approach 4

In Approaches 1 and 2, described in Subsections 2.5.1 and 2.5.2, respectively, even if the coefficient of determination $\left(R^2\right)$ for the quadratic-curve-fit is high, say, above 99.9%, the resulting values of $K$ and $c_F$ are not necessarily uniquely determined: thus, for example, a small change in the value of either one of these two parameters, with the corresponding adjustment of the other parameter, can yield another quadratic-curve-fit with a similarly high value of the coefficient of determination. Thus, Approaches 1 and 2 produce pairs of $K$ and $c_F$ values that together reproduce the set of experimental data that were used to determine them, but they cannot be necessarily be taken as reliable and generally valid unique *individual* values of each of these parameters for modeling fluid flow in the porous media of interest. Approach 3, described in Subsection 2.5.3, is not afflicted by this difficulty; this matter is discussed further in Chapter 4.

It is possible to formulate another approach, denoted here as Approach 4, that could also overcome the above-mentioned difficulty that plagues Approaches 1 and 2. In this context, it is useful to note again that the Darcy and Forchheimer terms in Eq. 2.19 account for two different phenomena that contribute to the total pressure drop required for the fluid flow through the porous medium: the Darcy term ( $\mu u / K$ ) accounts for the viscous drag exerted on the fluid by the porous medium, and it is the dominant contributor to the overall pressure drop at very low flow rates (the so-called Darcy regime); and the Forchheimer term ( $\rho c_F u^2 / \sqrt{K}$ ) accounts for the form drag exerted on the fluid as it flow porous medium (the matrix of porous-metal-foam ligaments and nodes in the cases of interest), and it is the dominant contributor to the overall pressure drop at high flow rates. Thus, if it is possible to obtain accurate experimental data at very low flow rates, at which the contribution of the Forchheimer term to the overall pressure drop can be considered negligible (compared to that of the Darcy term) and dropped from Eq. 2.19, then a least-squares linear-curve-fit can be used to determine the permeability, $K$. This value of $K$ can then be assumed to be valid for all flow rates, and used along with experimental data obtained over a wide range of flow rates, and a least-squares quadratic-curve-fit (keeping all terms in Eq. 2.19), to determine the value of the dimensionless

form-drag coefficient, $c_F$. This line of thinking (procedure) is the essence of Approach 4, which is the one that is recommended in this work, but only if it is possible to obtain accurate experimental data for flow rates in the Darcy regime.

Thus, in Approach 4, for determining $K$ from $N$ sets of data points $\{u_i,\ (dp/dx)_i,\ \rho_i,$ and $\mu_i\}$ with fluid flow in the Darcy regime, and assuming $(-dp/dx) = (\mu/K)u$, a least-squares linear-curve-fit passing through the origin (0,0) is used as follows:

$$a \triangleq \frac{1}{K};\quad \zeta_i \triangleq \left(-\frac{dp}{dx}\right)_i;\quad a = \left[\sum_{i=1}^{N} \mu_i u_i \zeta_i\right] \Big/ \left[\sum_{i=1}^{N} (\mu_i u_i)^2\right] \tag{2.24}$$

Once $a$ in the above equation is computed using the aforementioned experimental data for fluid flow in the Darcy regime, the permeability ($K$ = 1/$a$) can be calculated. With this value of permeability and the full set of experimental data points $\{u_i,\ (dp/dx)_i,\ \rho_i,$ and $\mu_i\}$, inside and outside the Darcy regime, and keeping all terms in Eq. 2.19, a least-squares quadratic-curve-fit is used to determine $c_F$ as follows:

$$c_F = \left[K\left(\sum_{i=1}^{N} \rho_i u_i^2 \zeta_i\right) - \left(\sum_{i=1}^{N} \mu_i \rho_i u_i^3\right)\right] \Big/ \left[\sqrt{K}\left(\sum_{i=1}^{N} \rho_i^2 u_i^4\right)\right];\ \text{with } \zeta_i = \left(-\frac{dp}{dx}\right)_i \tag{2.25}$$

The application of the first part of Approach 4 requires the determination of the range of flow rates that corresponds to the Darcy regime. This is not a trivial task. A simple plot of the experimental data for $(dp/dx)_i$ versus $u_i$ could be examined for deviation from linearity to obtain an indication of when the flow is not in the Darcy regime, but this approach would only provide qualitative guidance, at best. Several quantitative criteria for determining the departure of the fluid flow from the Darcy regime have been proposed in the literature. One such criterion is related to the value of a Reynolds number based on the square-root of the permeability of the porous medium as the length scale:

$$\mathrm{Re}_K = \left(\rho u \sqrt{K}\right) \Big/ \mu \tag{2.26}$$

However, determining the value of this Reynolds number requires *a priori* knowledge of the value of the permeability of the porous medium. Furthermore, in the literature, there is also no consensus on a strict limiting or critical value of this Reynolds number, below which the fluid flow could be considered to be in the Darcy regime. Thus, borrowing from Zeng and Grigg (2006), in this work, a criterion for delineating the experimental data pertaining to the Darcy regime was linked to the maximum allowable contribution of the Forchheimer term to the overall pressure drop. This criterion can be expressed in terms of the so-called Forchheimer number, which is the ratio of form drag to viscous drag exerted by the porous medium on the fluid flowing through it:

$$Fo = \left(\rho c_F u^2 / \sqrt{K}\right) \Big/ \left(\mu u / K\right) = \left(\rho u c_F \sqrt{K}\right) \Big/ \mu \tag{2.27}$$

Innocentini et al. (2010) state that for values of Forchheimer number well below unity, the fluid flow through the porous medium is in the Darcy regime. Zeng and Grigg (2006) recommend a critical Forchheimer number of $Fo = 0.11$, which was obtained by setting a practical limit of 10% to the contribution of the Forchheimer term to the pressure drop.

## 2.6 Friction Factors

In this section, definitions of friction factors are presented for both laminar and turbulent fluid flows in straight rectangular ducts of uniform cross-section, that are fully open (no porous media), completely filled with porous metal foams, and containing adjacent open and porous-metal-foam domains. Analytical solutions (when possible) or empirical correlations (when available) are also presented along with some comments.

### 2.6.1 Fully Developed Laminar Flows in Straight Rectangular Ducts of Uniform Cross-Section

The Darcy friction factor, $f_D$, for such flows is defined as follows:

$$f_D = \{(-dp/dx)D_h\} \Big/ (0.5\rho u_{av}^2) \tag{2.28}$$

In the above equation, $dp/dx$ is the pressure gradient in the direction of the flow; $u_{av}$ is the average fluid velocity in the cross section of the duct; and $D_h$ is the hydraulic diameter of the rectangular duct, defined as follows:

$$D_h = 4A_{cs} / P_w \tag{2.29}$$

In this equation, $A_{cs}$ is the cross-sectional area of the duct and $P_w$ is its wetted perimeter. With respect to the notation given in Figure 2.1, the following expression for this Darcy friction factor can be analytically determined for steady, fully developed, two-dimensional, laminar flow of a constant-property Newtonian fluid in a straight rectangular duct with uniform cross section, that is fully open ($\omega$ = 1):

$$\Lambda = \frac{W_{channel}}{2H}; \quad \lambda_n = (2n+1)\pi; \quad \bar{U} = \frac{1}{12} - \frac{8}{\Lambda}\sum_{n=0}^{\infty}\frac{\tanh(\lambda_n \Lambda)}{\lambda_n^5}; \quad \mathrm{Re} = \frac{\rho u_{av} D_h}{\mu}$$
$$f_D = \frac{8}{\bar{U}\,\mathrm{Re}}\left(\frac{W_{channel}/H}{1+(W_{channel}/H)}\right)^2 \tag{2.30}$$

In the above equations, $\bar{U}$ is an average dimensionless velocity of the fluid in the cross section of the rectangular duct; $W_{channel}$ is the width of the rectangular duct; and Re is the Reynolds number of the flow based on $u_{av}$ and $D_h$.

### 2.6.2 Fully Developed Turbulent Flows in Straight Rectangular Ducts of Uniform Cross-Section

In this work, the Darcy friction factor for statistically steady, fully developed, two-dimensional, turbulent flows of a constant-property Newtonian fluid in straight rectangular ducts with uniform cross section, that is fully open ($\omega$ = 1), was calculated using a correlation proposed by Jones (1976). In this correlation, a correction factor, $\varphi^*$,

and a modified Reynolds number, $\mathrm{Re}^*$, are used. The proposed correction factor, $\varphi^*$, is a complicated function of the geometry of the rectangular duct, but Jones (1976) also presented the following simplified relation that is accurate to ±2%:

$$\varphi^* \simeq \frac{2}{3} + \frac{11}{24}\frac{H}{W_{channel}}\left(2 - \frac{H}{W_{channel}}\right) \tag{2.31}$$

The modified Reynolds, $\mathrm{Re}^*$, is related to the Reynolds number, $\mathrm{Re}$, defined earlier in Eq. 2.30, as follows:

$$\mathrm{Re}^* = \varphi^* \mathrm{Re} \tag{2.32}$$

Jones (1976) proposed that this modified Reynolds number be used in the following correlation to obtain the Darcy friction factor, $f_D$:

$$\frac{1}{\sqrt{f_D}} = 2.0 \log_{10}(\mathrm{Re}^* \sqrt{f_D}) - 0.8 \tag{2.33}$$

This correlation predicts the experimental data analyzed by Jones (1976) to within ±5%.

### 2.6.3 Fully Developed Flows in Straight Rectangular Ducts of Uniform Cross-Section Filled with Porous Media

For such flows of constant-property Newtonian fluids, several different definitions of the friction factor have been proposed in the published literature. A commonly used definition is a modified version of the Darcy friction factor given in Eq. 2.28, in which the hydraulic diameter is replaced by the square-root of the permeability. This definition has been used, for example, by Paek et al. (2000) and Dukhan and Minjeur II (2011), in investigation of flows in porous metal foams. It has also been used by Ward (1964) and Beavers et al. (1973) in studies of porous media consisting beds of spherically shaped particles. In another definition of friction factor for such flows, the hydraulic diameter is

replaced by an effective pore diameter, as in Bonnet et al. (2008). Lacroix et al. (2007), Madani et al. (2007), and Edouard et al. (2008), have recommended the strut or ligament diameter as the most suitable length scale for the microstructure of porous metal foams; and Jin and Leong (2008) have presented a modified Darcy friction factor based on a so-called hydraulic ligament diameter for such foams.

Following the practice that is commonly used to characterize the cores of compact heat exchangers [Kays and London (1998)], the friction factor for porous media could be based on a hydraulic diameter related to the specific area (surface area per unit volume), $\alpha_{sv}$, as follows: $D_{h-pd} = 4/\alpha_{sv}$. Correlations that give the specific area in terms of other parameters that characterize the topology of porous metal foams are available in the published literature, for example, in the work of Calmidi (1998). However, such correlations are afflicted by high uncertainties and are difficult to generalize.

In this work, for fully developed flows of constant-property Newtonian fluids in straight rectangular ducts of uniform cross section, completely filled with porous metal foams, in the definition of the Darcy friction factor, an effective ligament diameter, $d_l$, is suggested as the characteristic length. An expression for this Darcy friction factor can be derived by dividing both sides of Eq. 2.19 by $\rho u^2$ and subsequently multiplying both sides by $d_l$. The resulting equation can be recast in the following form:

$$\left(f_D\right)_{d_l} = \frac{\left(-dp/dx\right)d_l}{0.5\rho u^2} = \left[\frac{2}{Da_{d_l}}\frac{1}{\mathrm{Re}_{d_l}} + \frac{2c_F}{\sqrt{Da_{d_l}}}\right];\ Da_{d_l} = \frac{K}{d_l^2};\ \mathrm{Re}_{d_l} = \frac{\rho u d_l}{\mu} \qquad (2.34)$$

In this equation, $u$ is the superficial velocity; $Da_{d_l}$ is the Darcy number based on the effective ligament diameter; and $\mathrm{Re}_{d_l}$ is the Reynolds number defined with the effective ligament diameter as the characteristic length.

### 2.6.4 Fully Developed Flows in Straight Rectangular Ducts of Uniform Cross-Section Containing Adjacent Open and Porous Domains

For fully developed laminar or turbulent flows of constant-property Newtonian fluids in straight rectangular ducts containing adjacent open and porous domains, if assumptions akin to those in Section 2.5 are invoked, then Eq. 2.19 applies in the porous domain. Thus, in terms of the dimensionless variables and parameters introduced in Section 2.4, the expression given in Eq. 2.12 can be used to estimate the dimensionless superficial velocity, $u_{\infty *}$, in the bulk of the porous domain. In turn, this expression, in conjunction with the experimental measurements obtained for the flows of interest (which include the total mass flow rate in the rectangular duct, $\dot{m}_{total}$), can be used to estimate the mass flow rate in the open domain of the duct, $\dot{m}_{od}$, and the corresponding Reynolds number based on an approximation of the hydraulic diameter of the open domain, $\mathrm{Re}_{od}^{D_h}$, as follows:

$$u_{av-pd} = u_{\infty *} U; \quad \dot{m}_{od} = \dot{m}_{total} - \rho u_{av-pd}(1-\omega)(HW_{channel}); \quad D_{h-od} = 2(\omega H)$$
$$\mathrm{Re}_{od}^{D_h} = \{\dot{m}_{od} / (\omega HW_{channel})\} D_{h-od} \big/ \mu \tag{2.35}$$

Finally, the Darcy friction factor for the open domain, $f_{D-od}$, can be defined as follows:

$$f_{D-od} = \left\{\left(-dp/dx\right) D_{h-od}\right\} \Big/ \left(0.5 \rho u_{av-od}^2\right) \tag{2.36}$$

The theoretical considerations presented in this chapter were used for designing the experimental set-ups and procedures that are described in Chapter 3, and also for processing the experimental measurements and obtaining the results that are presented in Chapter 4.

# Chapter 3 – Experimental Apparatus and Procedures

Descriptions of the experimental apparatus and procedures that were designed, implemented, and used in this work are presented and discussed in this chapter.

## 3.1 Overview of the Experimental Apparatus

The experimental apparatus that was designed and constructed for this work is schematically presented in Figure 3.1. It consists of the following elements, listed in order, from the upstream to the downstream ends: i) a straight rectangular duct (inlet and test sections), hereafter referred to as the air channel; ii) transition box; iii) Venturi tube; iv) laminar flow elements; v) flow-rate control valves; and vi) blower.

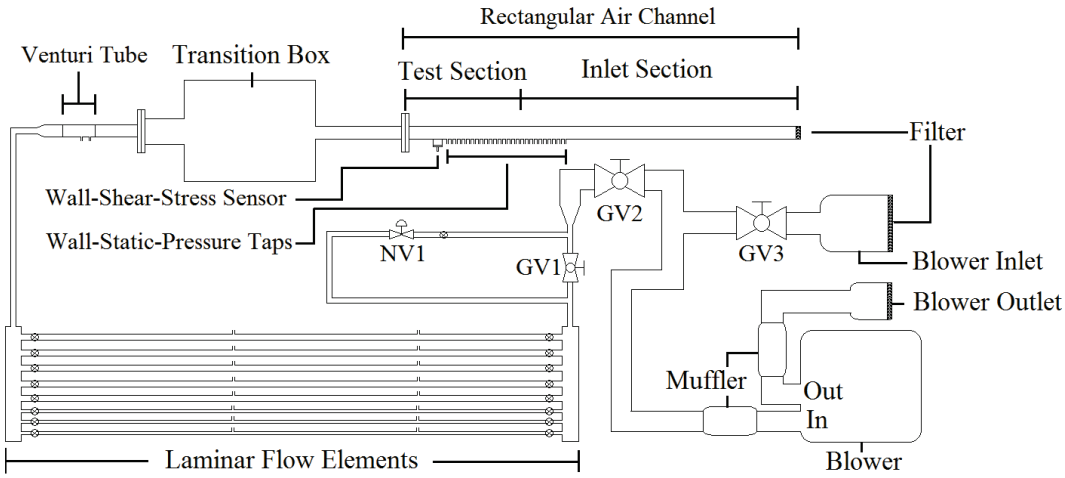


Figure 3.1: Schematic of the experimental apparatus

A 10-horsepower centrifugal air blower (Regenair R7100A) was operated in suction mode and air was drawn through a filter into the straight rectangular air channel. The inlet section was designed to ensure that the airflow became fully developed prior to entering the test section. The test section was instrumented with 64 static-pressure taps and a shear-stress sensor on its upper wall; and it was designed so that it could be run empty (fully open, or no porous metal foams inside), completed filled with different porous-metal-foam samples, and containing adjacent open and porous-metal-foam domains akin

to the one shown schematically in Figure 2.1. Downstream from this test section, the air flowed through a duct of rectangular cross-section to a duct of circular cross section via an aluminum all-welded transition box, and then through two flow-rate measurement devices, a Venturi tube and a bank of laminar flow elements. The airflow rate was controlled by a needle valve (NV1) at low flow rates, and a globe valve (GV1) at higher flow rates. Downstream from these flow-control valves, the airflow was fed through a globe valve (GV2) to the main (or common) portion of a T-junction and then to a muffler that was connected to the blower. Another globe valve (GV3) was used to connect the blower via the branch portion of the aforementioned T-junction to a path of relatively low flow resistance: this set-up ensured that the blower was not starved of air and not overheated even at low flow rates through the test section. In this context, it should be noted that the blower was never operated with the GV3 globe valve fully closed.

In the following section, the porous metal foams used in this work and the procedures that were employed to characterize their geometric parameters are discussed. In the subsequent sections, the key aspects of the above-mentioned experimental apparatus and the related procedures are presented and discussed.

## 3.2 Porous Metal Foams and their Geometrical Characterization

Four different porous metal foams were used in this work: a 40 pores per inch (PPI) aluminum-alloy (6101-T6) Duocell® foam from ERG Aerospace Corporation; and 20, 40, and 60 PPI iron-alloy (FeCrAlY) sintered METPORE foams from Selee Corporation (a Porvair company). A single sample of the aforementioned ERG foam and two samples of each of the above-mentioned METPORE foams were purchased. The ERG foam will hereafter be referred to as the ERG40 foam; and the METPORE foams, taking into account their PPI designation and the two samples of each of them, will be referred to in the remainder of this thesis as M20-1, M20-2, M40-1, M40-2, M60-1, and M60-2. For the purposes of geometrical characterization, for each of these foams, a sample piece, cut from the same manufactured piece that was used in the test section, was also purchased.

Although not explicitly mentioned on the website of the ERG Aerospace Corporation, or in any of their data-specification sheets, the ERG Duocell® foam is believed to be manufactured using an investment-casting process that produces connected solid ligaments or fibers, as discussed in Ashby et al. (2000). In contrast, the METPORE foams are characterized by hollow ligaments, and manufactured using a special sintering process that is discussed in Zhao et al. (2001), who refer to these foams as Porvair foams.

### 3.2.1 Dimensional Parameters of the Structural Matrix

The structure of the porous metal foams is characterized by the following dimensional parameters: i) ligament diameter ($d_l$); ii) pore diameter ($d_p$); and iii) cell diameter ($d_c$). Calmidi (1998) and Lacroix et al. (2007) have argued that the cellular structure of the porous metal foams can be approximated by a collection of dodecahedron cells, akin to that shown in Figure 3.2 (left). Others, for example, Jin and Leong (2008) and Zhao et al. (2001), have proposed a collection of tetrakaidecahedron cell shapes, akin to that illustrated in Figure 3.2 (right), to represent the porous metal foams.

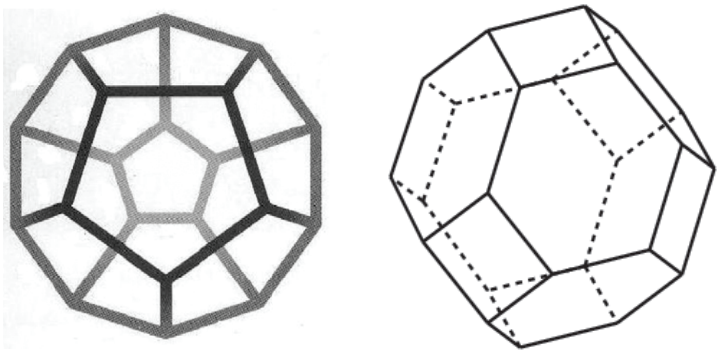

Figure 3.2: Schematic of a dodechedron cell (left) and a tetrakaidecahedron cell (right)

Calmidi (1998) has also discussed the variation of the shape of the ligament cross-section as a function of porosity, which is illustrated schematically in Figure 3.3: at a porosity of about 0.85, the cross-section of the ligaments is effectively circular, and their diameter decreases with increasing values of porosity; and at porosity values greater than 0.90, the cross-section of the ligaments transitions to a triangular shape. The ligament diameter varies along its length, with the thickest point at each end of the ligament and the thinnest

point at its center. In this work, the ligament cross-section was assumed to be effectively circular for porosity values of less than 0.94, and for a given ligament, the diameter was taken as the arithmetic mean of its highest value, $d_1$, near a vertex, and lowest value, $d_2$, which occurs roughly at its midpoint, as displayed in Figure 3.4.

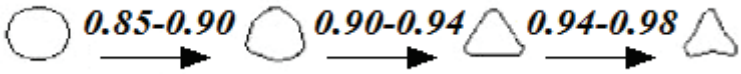


Figure 3.3: Cross-sectional variation with porosity of a ligament [Calmidi (1998)]

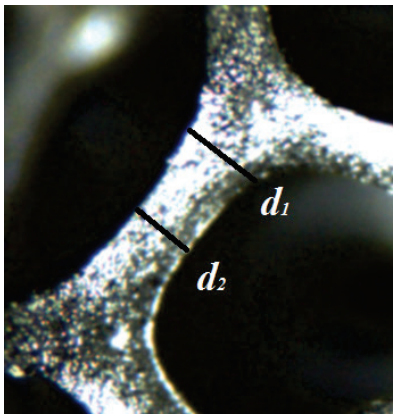


Figure 3.4: Photomicrograph showing highest and lowest ligament diameters, $d_1$ and $d_2$

Both the pore and the cell diameters were approximated by the diameter of fitted circles, as illustrated in Figure 3.5. It should also be noted again that for each of the porous metal foams used in this work, the ligament, pore, and cell diameters were measured using a sample piece, cut from the same manufactured piece that was used in the test section. These dimensional parameters of the structural matrix of each of the porous metal foams used in this work were measured using a Carton model SPZT50 trinocular stereo microscope, a TUCSEN model IS1000 10 megapixel (MP) microscope camera, related ISCAPTUREv2.6 image capturing software, and a supplied calibration slide. The measurements of the ligament, pore, and cell diameters were accomplished using the following procedure: i) the porous-metal-foam sample was placed under the microscope, an appropriate magnification was selected, and the foam sample was put into focus; ii) the camera was set at a resolution of 2MP; iii) images of 20 ligaments, 10 pores, and 10 cells

were acquired and saved using the ISCAPTURE software; iv) the porous-metal-foam sample was removed and gauge blocks were used to bring the calibration slide into focus (leaving the microscope settings unchanged) and an image of it was also acquired and saved; and v) using the ISCAPTURE software and the image of the calibration slide as a reference, the ligament, pore, and cell diameters were determined.

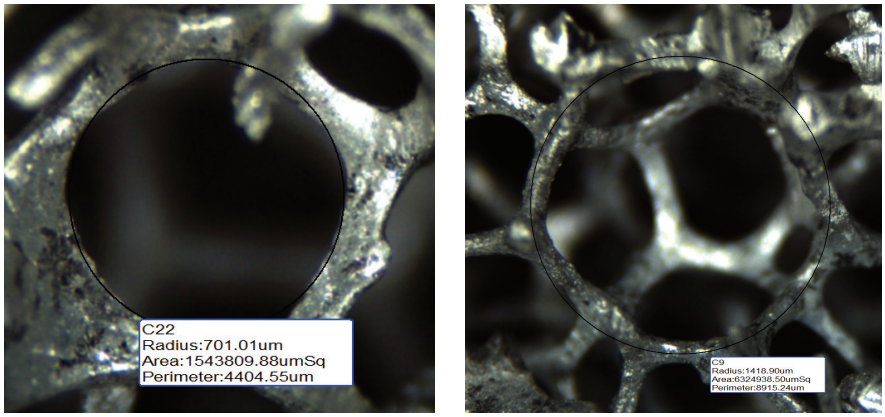


Figure 3.5: Schematic of a pore diameter (left) and a cell diameter (right)

### 3.2.2 Porosity

The porosity, as defined in Eq. 2.2, can be cast as a function of the bulk density of the medium, $\rho_b$, and the density of the solid material of its structural matrix, $\rho_s$.

$$\varepsilon \triangleq \left(V_f / V_b\right) = \left[\left(V_b - V_s\right)/V_b\right] = \left[1 - \left(V_s / V_b\right)\right] \simeq \left[1 - \left(\rho_b / \rho_s\right)\right] \tag{3.1}$$

In this equation, $V_f$ is the void volume within the porous medium; $V_s$ is the volume of its solid structural matrix; and $V_b$ is the total volume of the porous medium. The porosity as defined in Eq. 3.1 applies to porous metal foams with a matrix consisting of solid ligaments, as in the Duocell® foam used in this study. For porous metal foams with hollow ligaments, the porosity can be calculated using the following equation:

$$\varepsilon = \left[1 - \rho_b \Big/ \left\{\rho_s \left(1 - R^2\right)\right\}\right];\ R = \left(d_i / d_l\right) \tag{3.2}$$

In Eq. 3.2, $d_i$ is the average inner diameter of the hollow ligaments. The value of $R$ was difficult to determine for the METPORE foam samples used in this study. However, Zhao et al. (2001) also used METPORE foams with the same nominal relative density, ($\rho_b / \rho_s$) = 5%, as that of the foams used in this work, so their $R$ values and ligament diameters (summarized below) were adapted for this work using linear interpolation.

| Foam Parameters | Sample #1 | Sample #2 | Sample #3 |
|---|---|---|---|
| **PPI rating** | 10 | 30 | 60 |
| **$\rho_b / \rho_s$ (nominal)** | 5% | 5% | 5% |
| **$d_l$ (μm)** | 287 | 215 | 124 |
| ***R*** | 0.56 | 0.51 | 0.35 |

Table 3.1: $R$ values and ligament diameters reported in Zhao et al. (2001)

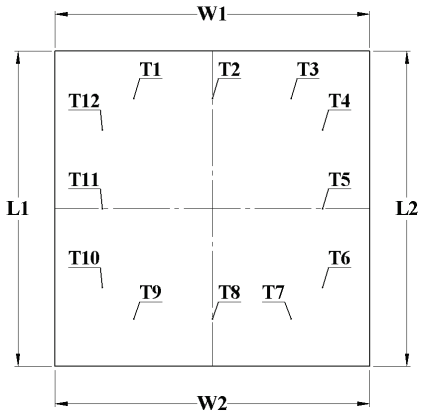


Figure 3.6: Schematic of width, length and thickness measurement locations

The bulk volume of each porous-metal-foam sample (rectangular parallelepiped) was determined from the following measurements at the locations indicated in Figure 3.6: the length, $L$, width, $W$, accurate to ±0.0005"; and thickness, $t$, accurate to ±0.0001", at twelve locations, three equally spaced locations along each side, approximately three-quarters of an inch away from the edge. As the samples had some variation in thickness, their average length, average width, and average, minimum, and maximum thicknesses of the sample were used to calculate the corresponding average, minimum, and maximum bulk volume. Each sample was weighed three times on a digital scale (Acculab VI-350), with a 350 g capacity and repeatability of ±0.01 g; and the average of the three measurements was taken to be the bulk mass of the piece. The bulk density of each piece

was then calculated by dividing the bulk mass by the bulk volume. The solid density of the FeCrAlY of the Selee foams ( $\rho_s$ = 7.2 g/cc$^3$) was supplied by the manufacturer, and the solid density of the Al-6101-T6 of the ERG foam ( $\rho_s$ = 2.70 g/cc$^3$) was taken from the "standard" density data reported on MatWeb, a material property database.

## 3.3 Air Channel

As is shown schematically in Figure 3.1, the air channel consisted of sequentially connected inlet and test sections, both of which were straight rectangular ducts with fixed nominal inside width, $W_{channel}$ = 6". It was designed so that the test section could be set up with different open-domain heights and a fixed length of 18" (nominal), with and without the porous-metal-foam samples, and also with a solid aluminum plate ( $\varepsilon$ = 0) replacing the porous metal foam. The inlet section could also be set up with different heights and lengths, in various desired configurations. The test section (with respect to the notation given in Figure 2.1) and the inlet section (always fully open, and its height denoted by $H_{inlet\ channel}$) of this air channel could be configured as follows: with a solid aluminum plate (replacing the porous domain in the test section) and the heights of the open domains in the test and inlet section of $\omega H$ = $H_{inlet\ channel}$ = 1/8", 1/4", or 1/2" (nominal); test section completely filled with different samples of the porous metal foams ( $\omega$ = 0) and mated with the fully-open inlet section, with $H$ = $H_{inlet\ channel}$ = 1/2" (nominal); and with adjacent open and porous-metal-foam domains in the test section, with the open domain matched to fully-open inlet section, with (1 - $\omega$)$H$ = 1/2" (nominal) and $\omega H$ = $H_{inlet\ channel}$ = 1/8", 1/4", or 1/2" (nominal). Assembled and exploded isometric views of the full air channel are shown in Figure 3.7, along with the corresponding lengths (in inches) of the test section and the various portions of the inlet section. Details of the cross-sections of test and inlet sections are given later, in Subsections 3.3.1. and 3.3.2, respectively. It should be noted here that the overall length of the inlet section could be and was adjusted so that the airflow in this section was always fully developed before it entered the test section (details given in Subsection 3.3.1).

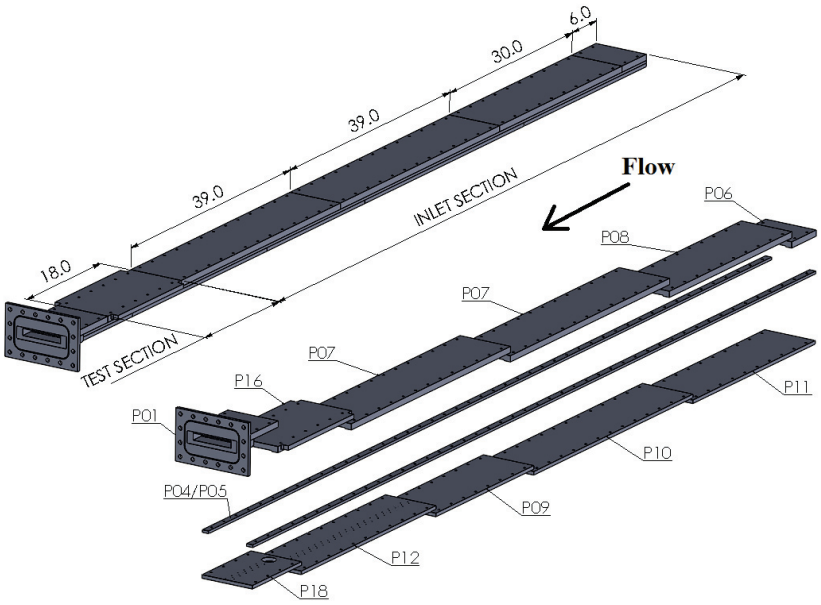


Figure 3.7: Assembled and exploded isometric views of the air channel

With reference to Figure 3.7, the inlet section could be configured using various combinations of the following elements: up to four c-channels (2 x P07, P08, P06); two pairs of side rails, which were used to modify the channel height (2 x P04 or 2 x P05); up to three rectangular bottom plates (P09, P10, P11); and a portion of the wall-static-pressure-tap plate (P12), which was used to determine wall-static-pressure distribution in the inlet section, immediately prior to the entrance of the test section. The test section was designed to accommodate adjacent open and porous-metal-foam or solid-aluminum domains, and it was comprised of the following elements: a flange assembly (P01) to mate the air channel to the transition box; a test-section c-channel (P16); a wall-static-pressure-tap plate (P12); and a wall-shear-stress-sensor plate (P18). The following table summarizes the various parts used to configure the air channel to run experiments with the desired values of the open-domain heights in the test section.

| $\omega H$ | Test Section Parts | Additional Parts |
|---|---|---|
| **1/8" (3.175 mm)** | P01, P16, P18, P12 | 1 x P07, P06, P09 |
| **1/4" (6.350 mm)** | | 2 x P04, 2 x P07, P06, P09, P10 |
| **1/2" (12.70 mm)** | | 2 x P05, 2 x P07, P08, P06, P09, P10, P11 |

Table 3.2: Air channel configurations and associated parts

### 3.3.1 Inlet Section

The cross-section of the inlet section is schematically illustrated in Figure 3.8: the coarse-hatched regions correspond to a solid aluminum base plate and a c-channel; and the fine-hatched regions correspond to the side rails. The fully-open height of the inlet channel, $H_{inlet\ channel}$, is determined by adding the open-height of the c-channel, $t1$, and side-rail thickness, $t2$. These dimensions (nominal) and the corresponding lengths of the inlet section are summarized in the table below.

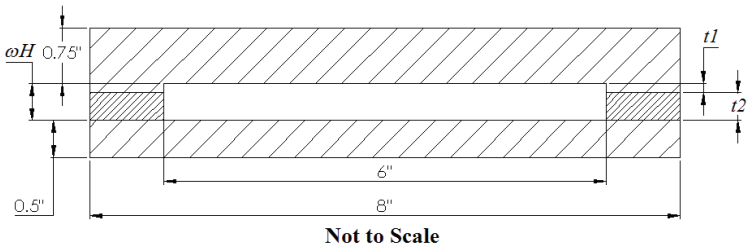


Figure 3.8: Cross-section of the inlet section

| $H_{inlet\ channel}$ | $t1$ (mm) | $t2$ (mm) | Length (mm) |
|---|---|---|---|
| **1/8" (3.175 mm)** | 3.175 | --- | 1143.0 |
| **1/4" (6.350 mm)** | | 3.175 | 2133.6 |
| **1/2" (12.70 mm)** | | 9.525 | 2895.6 |

Table 3.3: Some cross-sectional dimensions and corresponding lengths of the inlet section

The length of the inlet section was adjusted to ensure that fully developed airflow entered the test section: the Langhaar relation, $L_{dev,\,laminar} / D_h = 0.06\,\mathrm{Re}_{D_h}$ [Fox (2006)], was used for laminar flows; and for turbulent flows, the relation $L_{dev,\,turbulent} / D_h = 10$ is considered adequate. Assuming the flow is laminar for $\mathrm{Re}_{D_h} \le 2000$, the maximum values of development length corresponding to the different values of $H_{inlet\ channel}$ and also the ratio $L_{inlet} / L_{dev,laminar}$ are summarized in Table 3.4. For $H_{inlet\ channel}$ = 1/8" and 1/4" (nominal), the length of the inlet section exceeds the maximum laminar-flow development lengths by roughly a factor of 1.5. However, for $H_{inlet\ channel}$ = 1/2", due to space limitations in the laboratory, the length of the inlet section was only slightly larger than the maximum development length for laminar flow.

| $H_{inlet\ channel}$ | $D_h$ (mm) | $L_{dev,\ laminar}$ (mm) | $L_{inlet}/L_{dev,\ laminar}$ |
|---|---|---|---|
| **1/8" (3.175 mm)** | 6.2200 | 746.4 | 1.53 |
| **1/4" (6.350 mm)** | 12.192 | 1463.0 | 1.46 |
| **1/2" (12.70 mm)** | 23.446 | 2813.5 | 1.03 |

Table 3.4: Maximum laminar-flow development lengths in the inlet section

### 3.3.2 Test Section

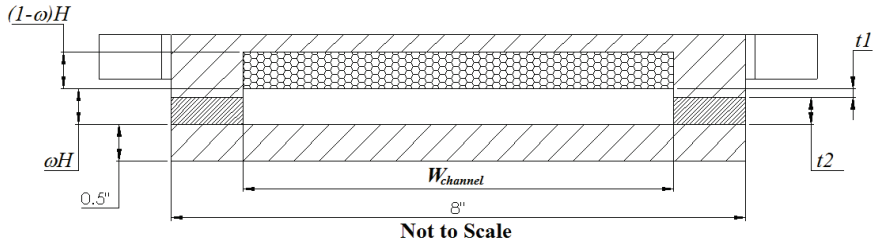


Figure 3.9: Cross-section of the test section

The cross-section of the test section is schematically illustrated in Figure 3.9: the coarse-hatched region at the bottom of the figure corresponds to either the wall-static-pressure-tap plate (P12) or the wall-shear-stress-sensor plate (P18), as the bottom of the test section is comprised of both these plates; the coarse-hatched region at the top of the figure corresponds to the solid aluminum plate that forms the base of the c-channels that house the porous metal foams (or the solid aluminum plate); the fine-hatched regions indicate the side rails; and the region with the honeycomb-pattern corresponds to the porous metal foam (or a solid aluminum plate) that resides within the c-channel of the test section. The height of the porous metal foam (or the solid aluminum plate) contained inside the test section is denoted by $(1-\omega)H$, and $\omega H$ indicates the open-domain height. Eight different test-section c-channels were used: a c-channel with a solid aluminum plate (rather than any of the porous-metal-foam samples) integrated within it, for use in calibration of the wall-shear-stress sensor and also benchmarking tasks (referred to as the calibration c-channel); and seven other c-channels that contained the seven different porous-metal-foam samples described in Section 3.2. The average values of the geometrical dimensions of the c-channel width, $W_{channel}$, open-domain height of the c-

channel, $t1$, and porous-metal-foam height, $\omega H$, for each of these eight test-section c-channels are summarized in Chapter 4. Details of the test-section c-channel containing the Duocell® foam, the test-section c-channels housing the METPORE foams, and the wall-static-pressure taps and related connections are provided in the following three subsections.

### 3.3.2.1 Test-Section C-Channel with the Duocell® Foam

This test-section c-channel is schematically illustrated in Figure 3.10: the hatched region represents solid aluminum; and the region with the honeycomb-pattern corresponds to the Duocell® foam.

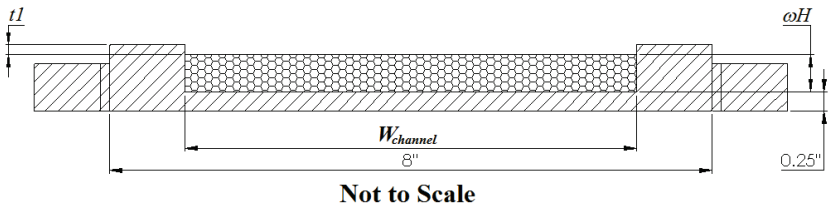


Figure 3.10: Cross-section of the test-section c-channel with the Duocell® foam

The ERG40 test-section c-channel was purchased fully machined and assembled, with the 40 PPI aluminum (6101-T6) foam brazed into an aluminum c-channel. The cost of this particular c-channel was quite high, thus only one was purchased. A photograph of a cross-section of this ERG40 test-section c-channel is given below in Figure 3.11.

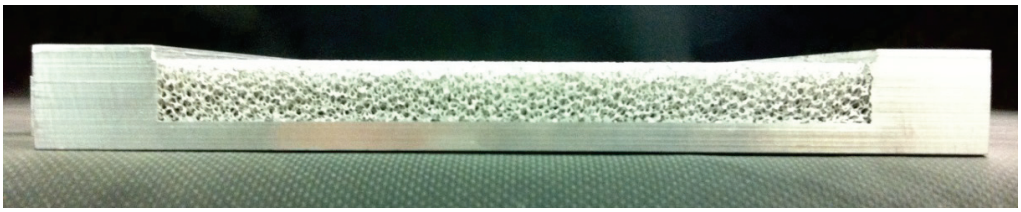

Figure 3.11: Photograph of a cross-section of the ERG40 test-section c-channel

### 3.3.2.2 Test-Section C-Channels with the METPORE Foams

Figure 3.12: METPORE-foam-aluminum-base-plate combination within an oven prior to the start of the heating cycle for curing the epoxy

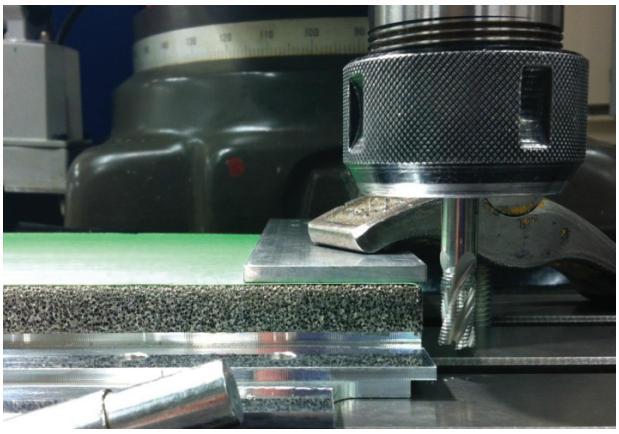

Figure 3.13: Milling set-up of the METPORE-foam-aluminum-base-plate combination

The Selee Corporation did not offer manufacturing capabilities akin to those provided by ERG Aerospace. Thus, the six test-section c-channels that housed the six METPORE porous metal foams were designed and constructed by the author in the following manner: i) 0.5"x6"x24" pieces of each of the six METORE foams were purchased; ii) each of these pieces was then laser cut into two pieces, a 0.5"x6"x18" piece to be attached to a c-channel and used in the test section, and a 0.5"x5.5"x5.5" piece to serve as a sample piece for determining the above-mentioned structural parameters and porosity of the foam; iii) then the 0.5"x6"x18" pieces were each bonded to an aluminum base plate, using

a thermally conductive two-part epoxy (Duralco 133 purchased from Cotronics Corporation), and this combination was cured for four hours at 250ºF, and then for another four hours at 350 ºF, to achieve optimum adherence properties, in an oven at atmospheric pressure, in the McGill University Composites Laboratory; iv) the aforementioned pieces of foam supplied by Selee Corporation had extremely rough edges, so the next step was to machine (in the McGill Engineering Machine Tool Laboratory) the sides of each of the foam pieces (epoxied to the aluminum base plate) to achieve the desired dimensions to acceptable precision; and v) after this machining, two side rails were attached to each base plate and bonded to the epoxied foam, using the same thermal epoxy mentioned above, to obtain the final test-section c-channel with the foam epoxied within it. Photographs of a METPORE-foam-aluminum-base-plate combination (clamped between two steel plates, with a silicon gasket in between each steel plate and foam, to avoid damaging the foam) inside the oven prior to the start of the heating cycle for curing the epoxy, set up on a milling machine, and as a fully-assembled test-section c-channel (view of a cross-section) are presented in Figures 3.12 to 3.14, respectively.

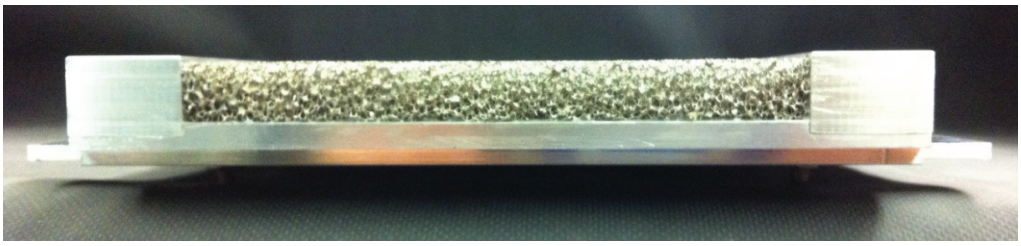

Figure 3.14: Cross-section of a METPORE foam test-section c-channel

#### 3.3.2.3 Wall-Static-Pressure Taps and Related Connections

The wall-static-pressure taps in the P12 plate (see Figure 3.7) were used to obtain time-averaged measurements within the test section. This plate was instrumented with 64 wall-static-pressure taps, across three parallel longitudinal rows: 22 such taps along the longitudinal centerline of the plate (center row); 21 such taps located along a straight line located 0.5" to the right of the longitudinal centerline (right row); and 21 such taps located along a straight line located 0.5" to the left of the longitudinal centerline (left row). On any one of these rows, the axial distance between two successive taps was 1.5"

and the first tap on each row was located at an axial distance of 0.75", 1.25", and 1.75" away from the upstream edge of the wall-static-pressure-tap plate (P12), for the center, left, and right rows, respectively. These wall-static-pressure taps were numbered from 1 to 64: tap # 1 was the first one on the center row, tap # 2 was the first one on the left row; tap # 3 was the first tap on the right row; and this sequential numbering pattern was continued along the length of the plate (P12). The wall-shear-stress-sensor plate (P18) also included 17 wall-static-pressure taps, similar to those discussed above for plate P12 (they were incorporated into this plate for future works).

At each wall-static-pressure tap location, a #21 (~4.0 mm) diameter hole was first drilled to a depth of 3/8" (~9.5 mm), and then a 1/32" (~0.8 mm) diameter hole was drilled through the remainder of the 1/2" (12.7 mm) aluminum plate (P12 or P18), to form the base of the pressure-tap hole. Threads were then cut into the curved surface of the #21-diameter hole, using a #10-32 tap, to a depth of 1/4" (~6.4 mm). A Clippard Minimatic brass pneumatic fitting with a captivated o-ring (Model 11792-5) was then screwed into the aforementioned tapped hole, and used to connect a 1/16" pressure tubing (Scanivalve #Vinl-063) to the pressure tap. Although these pneumatic fittings contained a captivated o-ring, to fully ensure there was no air leakage through the threaded connection of these fittings to the pressure taps, the base of each fitting was also epoxied in place (after being screwed into the threaded hole) using a thin bead of Lepage Marine Epoxy.

In this context, it should also be noted that a further 21 blind holes on the P12 plate, and 6 blind holes on P18 plate, were drilled to a depth of 3/8", using a drill of diameter 3/32" (~2.4 mm): these blind holes are intended for the potting of calibrated thermocouples to measure the average test-section temperature in future works. In this work, two shielded and calibrated thermocouples were potted in the aforementioned blind holes in the P12 plate of the air channel, one immediately upstream and the other immediately downstream of the test section, using a thermally conductive silicone paste (Omega OT-201). This thermocouple connection was secured to the P12 plate using a combination of electrical tape (inner layer) and aluminum tape (outer layer).

The determination of the test-section wall-static-pressure distributions required multiple pressure-drop measurements to be taken. For this task, the lines (1/16" pressure tubing) connected to the test-section-wall-static-pressure taps were connected at their other ends to a mechanical multiplexer (Scanivalve 48D9), which included a solenoid drive and controller (Scanivalve model CTLR10(P)/S2-26). The mechanical multiplexor allowed up to 48 such pressure lines (from the test-section wall-static-pressure taps), and one such pressure line (connected to a wall-static-pressure tap designated as the reference tap), to be linked to the differential pressure transducers used in this work. Details of these differential pressure transducers are presented in Section 3.6. The solenoid-drive controller was operated using a data acquisition and control unit (HP 3497A), a personal computer, and a LabVIEW program [Afara (2012)].

## 3.4 Transition Box

An aluminum-alloy (6061-T6) transition box (all-welded construction) was located downstream of the air channel and upstream of the two flow-measurement sections (the Venturi tube and the laminar-flow elements), as illustrated in Figure 3.1. This transition box allowed the air to flow from a rectangular cross-section duct to a duct of circular cross-section, and had flanges with captivated o-rings to allow airtight connections.

## 3.5 Flow-Measurement Devices

The design, construction, and calibration of two devices for measuring mass flow rates are described in this section: a Venturi tube for high flow rates; and a bank of laminar-flow elements (LFEs) for lower flow rates.

### 3.5.1 Venturi Tube

The Venturi tube design and calibration are described in the following two subsections.

#### 3.5.1.1 Design

A Venturi tube, with a machined convergent section, was designed in accordance with the ISO 5167-4:2003 standard. A detailed engineering drawing of this Venturi tube is provided in Appendix A; and an assembly drawing of the Venturi tube, upstream and

downstream tubes, and various fittings is given in Figure 3.15, with item numbers for the various components.

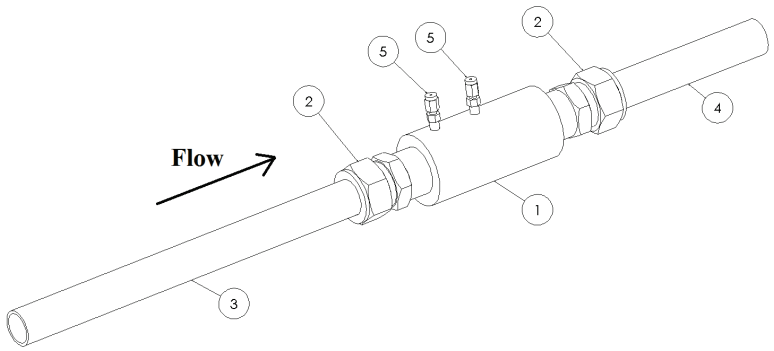


Figure 3.15: Schematic of the assembled Venturi tube

One-inch (1") 316 stainless steel Swagelok compression fittings (SS-1610-1-16WBT; Item 2) were welded to each end of the Venturi tube (Item 1). Attached to these compression fittings were two pieces of one-inch (1") 316L Swagelok stainless steel seamless tubing (SS-T16-S-083): a 10"-long upstream tube (Item 3), which ensured fully developed turbulent flow at the entrance to the Venturi tube; and a 5"-long downstream tube (Item 4). Two 316 stainless steel Swagelok reducing compression fittings (SS-100-R-4; Item 5) were welded to the upstream and downstream pressure taps of the Venturi tube: a suitable length of 1/16" outer diameter 304 stainless steel tube (Scanivalve TUBN-063) was connected to each of the two reducing compression fittings, to enable connection of 1/16" vinyl pressure tubing (Scanivalve VINL-063) to the taps of the Venturi tube. Air temperature at the entrance of the Venturi tube was measured using a thermocouple was attached to the outer surface of the upstream tube using a thermally conductive silicone paste (Omega OT-201), and secured to the tube using an inner layer of electrical tape and an outer layer of aluminum tape. Thermal insulation was then wrapped around the complete Venturi-tube assembly.

All dimensions of the Venturi tube fell within the acceptable ranges of the ISO standard, except for the throat diameter, which was 0.629" (~16.0 mm), as the standard only covers diameters between 50 mm and 250 mm. This necessitated a calibration of the Venturi tube. This calibration and the use of the Venturi tube are discussed in the next subsection. Additional details of the calibration are provided in Appendix A.

### 3.5.1.2 Calibration

The Venturi tube was calibrated at Polycontrols Technologies Inc. (Brossard, Québec). The calibration data were used to calculate the mass flow rate of air passing through the Venturi tube, using Eq. 3.3, adapted from the ISO 5167-4:2003 standard (this approach is necessary to allow accurate determination of the mass flow rates at temperatures and pressure that are slightly different from those at which the calibration was done).

$$\dot{m}_{Venturi} = \frac{C}{\sqrt{1-\phi^4}} \eta \frac{\pi}{4} d^2 \sqrt{2\Delta p \rho_1} \tag{3.3}$$

In Eq. 3.3, $\dot{m}_{Venturi}$ is the mass flow rate through the Venturi tube; $C$ is the discharge coefficient relating the actual mass flow rate to the theoretical mass flow rate through the Venturi tube (in the theoretical calculation, $C$ is set equal to 1); $\phi$ is the ratio of the cylindrical throat diameter to the internal diameter of the upstream cylindrical section; $\eta$ is the expansibility factor (used to account for the compressibility of air), calculated using Eq. 3.4; $d$ is the throat diameter; $\Delta p$ is the pressure differential between the upstream and downstream pressure taps; and $\rho_1$ is the density of air at the upstream pressure tap. The throat diameter, $d$, of the Venturi tube was determined to be 0.6290" ±0.0002"; the internal diameter of the upstream section, $D$, was measured to be 0.8348" ±0.0001"; so the diameter ratio, $\phi = d / D = 0.7535$.

$$\eta = \sqrt{\left\{\left(\kappa \xi^{2/\kappa}\right)/\left(\kappa - 1\right)\right\}\left\{\left(1-\phi^4\right)/\left(1-\phi^4 \xi^{2/\kappa}\right)\right\}\left\{\left(1-\xi^{(\kappa-1)/\kappa}\right)/\left(1-\xi\right)\right\}} \; ; \; \xi \geq 0.75 \tag{3.4}$$

In Eq. 3.4, $\kappa$ is the isentropic constant for air, which was taken to be 1.4; and $\xi$ is the ratio of the throat absolute pressure, $p_2$, divided by the inlet absolute pressure, $p_1$.

The discharge coefficient, $C$, was calculated for each calibration point by dividing the calibration mass flow rate by the theoretical mass flow rate. In Section 5.5.3 of the ISO

5167-4:2003 standard, the recommended value of $C$ is 0.995, for 50 mm $\leq D \leq$ 250 mm, $0.4 \leq \phi \leq 0.75$, and upstream Reynolds number between $2\text{x}10^5$ and $1\text{x}10^6$. Theses ranges do not apply to the Venturi tube used in this work. Thus, taking guidance from Annex B of ISO 5167-4:2003, $C$ pertaining to the calibration data was cast as a function of the throat Reynolds number, $\text{Re}_d$:

$$\text{Re}_d = \left(4\dot{m}_{Venturi}\right)/\left(32\mu d\right) \tag{3.5}$$

$$C = D_0 + D_1 \text{Re}_d + D_2 \text{Re}_d^2 + D_3 \text{Re}_d^3 + D_4 \text{Re}_d^4 \tag{3.6}$$

The constants $D_0$, $D_1$, $D_2$, $D_3$, and $D_4$ in this equations are 0.935223, $2.8073 \cdot 10^{-6}$, $-5.04017 \cdot 10^{-11}$, $3.61026 \cdot 10^{-16}$, and $-9.16218 \cdot 10^{-22}$, respectively. This curve-fit had a coefficient of determination $\left(R^2\right)$ value of 0.96861.

The mass flow rate through the Venturi tube for a given differential pressure reading was calculated using an iterative method: 1) with the measured values of $\Delta p$, $p_1$ and $T_1$, obtain the values of $\eta$ and $\rho_1$ using Eq. 3.4 and property data for air; 2) start with $C_{guess}$ = 0.98 and calculate $\dot{m}_{Venturi}$ using Eq. 3.3 and $\text{Re}_d$ using Eq. 3.5; 3) using this value of $\text{Re}_d$ in Eq. 3.6, calculate a new discharge coefficient, $C_{new}$; and 4) repeat until $\left|C_{new} - C_{old}\right|/C_{new} \leq 10^{-10}$. At the end of this iterative method, the converged value of $C$ was used to calculate the final value of $\dot{m}_{Venturi}$. The uncertainty in the mass flow rate obtained using this iterative method was taken as the average absolute percentage difference between the calculated values and the corresponding values of the calibration mass flow rate for each of the calibration points. The calculated mass flow rates, calibration mass flow rates, and percentage differences are listed in Appendix A. This uncertainty was determined to be 0.135% of reading, and the maximum absolute percentage difference over the entire calibration range was 0.376%. The uncertainty in the values of $\dot{m}_{Venturi}$ during the calibration of the Venturi tube was ±0.2% of reading. Using

these two uncertainties ( $\delta\dot{m}_{calibration} / \dot{m}_{calibration}$ and $\delta\dot{m}_{method} / \dot{m}_{method}$ ) in Eq. 3.7 [Kline and McClintock (1953)], $\delta\dot{m}_{Venturi} / \dot{m}_{Venturi}$ was determined to be 0.241%.

$$\left(\delta\dot{m}_{Venturi} / \dot{m}_{Venturi}\right) = \sqrt{\left(\delta\dot{m}_{calibration} / \dot{m}_{calibration}\right)^2 + \left(\delta\dot{m}_{method} / \dot{m}_{method}\right)^2} \tag{3.7}$$

### 3.5.2 Laminar Flow Elements

The bank of LFEs consist of eight Swagelok 316L stainless steel seamless round tubes: five 1/2" tubes (SS-T8-S-049) and three 3/8" tubes (SS-T6-S-049), each tube of 0.049" wall thickness. It was constructed by connecting these eight tubes at each end to an eight-port Smartflow manifold (Burger & Brown Engineering Inc). A check-valve connected to each port of the two manifolds allowed a given LFE tube to be included or excluded from the flow circuit of the experimental apparatus (see Figure 3.16).

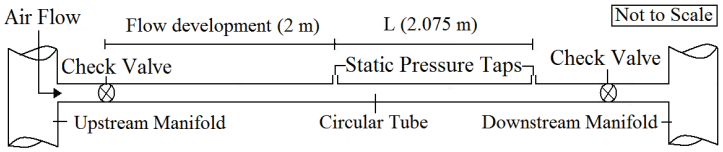


Figure 3.16: Schematic of a LFE tube

For each LFE tube, a flow development length of 2 m ensured that the airflow became fully developed before the first wall-static-pressure tap. The location of the second wall-static-pressure tap was chosen so that the centers of the two taps were separated by an axial distance of 2.075 m ±0.005 m. Each of the aforementioned taps were made from a 1/16" outer diameter 304 stainless steel tube (Scanivalve TUBN-063) connected to the LFE tube using a specially-designed fixture, machined from a solid block of stainless steel with welded Swagelok compression fittings. A thermocouple was attached to the outer surface of each LFE tube, at the midpoint between the two wall-static-pressure taps, using a thermally conductive silicone paste (Omega OT-201) and two successive layers of electrical tape and aluminum tape, and thermal insulation was wrapped around this connection. As this bank of LFEs was used for measurements of low rates of flow, the

flow in each tube was laminar ($\mathrm{Re}_{D_i} \leq 2000$): thus, this mass flow rate could be determined from the measured static-pressure difference, $\Delta p_{LFE}$, using the following equation which is obtained from the analytical Poiseuille solution:

$$\dot{m}_{LFE} = \left(\rho \pi D_i^4 \Delta p_{LFE}\right) \Big/ \left(128 \mu L_{LFE}\right) \tag{3.8}$$

In Eq. 3.8, which applies to each LFE tube, $\dot{m}_{LFE}$ is the mass flow rate of air; $D_i$ is the inner diameter; $\Delta p_{LFE}$ is the measured pressure drop across the two pressure taps; $L_{LFE}$ is the length between the centers of the two pressure taps; and $\mu$ is the dynamic viscosity of air at the measured temperature in between these pressure taps. For this bank of LFEs, the inner diameters of the 1/2" and 3/8" tubes were determined to be 0.402" (~10.2 mm) and 0.277" (~7.0 mm), respectively, with an accuracy of ±0.5% [Afara (2012)].

The table below summarizes the flow-measurement configurations (of the LFE tube-bank; or the Venturi tube) for the ranges of test-section Reynolds number investigated in this work, along with the associated experimental uncertainty in the calculation of the mass flow rate for each configuration, calculated using the procedure of Kline and McClintock (1953).

| Test Section Re | Flow-Measurement Configuration | $\delta\dot{m}/\dot{m}$ (%) |
|---|---|---|
| **0-125** | 1-3/8" LFE Tube | 2.22 |
| **126-375** | 3-3/8" LFE Tube | 2.97 |
| **376-550** | 3-1/2" LFE Tube | 2.97 |
| **551-900** | 5-1/2" LFE Tube | 3.54 |
| **901-maximum** | Venturi | 0.241 |

Table 3.5: Flow-measurement configurations

## 3.6 Instruments Used for Pressure Measurements

Two differential-pressure transducers were used to measure pressure differences throughout the experimental apparatus; and an electronic barometer was employed to

measure the atmospheric pressure within the laboratory. The various differential pressures measured in this work are illustrated schematically in the figure below:

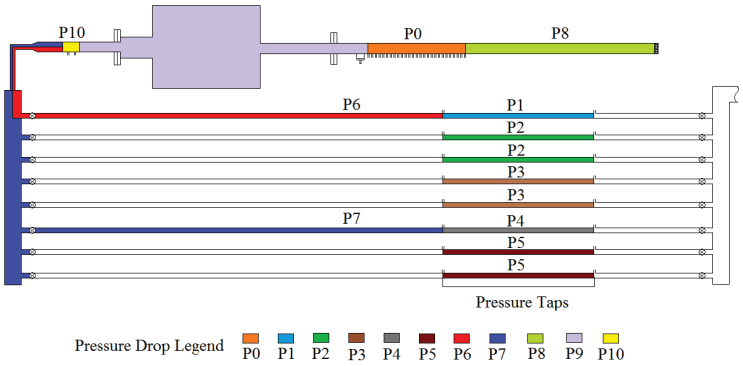


Figure 3.17: Schematic illustration of the differential-pressure drops and related notation

The appropriate differential-pressure transducer was connected to the appropriate pressure taps using suitable lengths of 1/16" vinyl pressure tubing (Scanivalve VINL-063) and an assembly of automated pneumatic valves (Clippard Minimatic, Model EV-2M-12VDC). For each differential pressure, the high- and low-pressure taps were connected to the high- and low-pressure ports, respectively, of an appropriate pressure transducer (described in the next subsection), using the 1/16" vinyl pressure tubing and related automated pneumatic valve for each line. By actuating the appropriate pair of these automated valves, the desired two lines to the high- and low-pressure ports of the appropriate pressure transducer could be selected. With reference to Figure 3.17 and starting from the upstream end of the experimental facility, the following differential pressures (DPs) were measured and recorded: P8, the DP between a pressure tube exposed to the atmospheric pressure in the laboratory and the reference wall-static-pressure tap used in the test section; P0, represents each of a set of test-section wall-static-pressure DPs, each one between the reference tap and a selected tap, chosen using the mechanical multiplexer (Scanivalve 48D9) mentioned earlier; P9, the DP between the reference tap and the upstream tap of the Venturi tube; P10, the DP across the upstream and throat pressure taps of the Venturi tube; P6, the DP between the reference tap and the upstream pressure tap of the first 1/2" LFE tube; P7, the DP between the reference tap and the upstream pressure tap of the first 3/8" LFE tube; P1, the DP between the upstream and

downstream pressure taps of the first 1/2" LFE tube; P2, the average of the DPs between the upstream and downstream pressure taps of the second and third 1/2" LFE tubes; P3, the average of the DPs between the upstream and downstream pressure taps of the fourth and fifth 1/2" LFE tubes; P4, the DP between the upstream and downstream pressure taps of the first 3/8" LFE tube; and P5, the average of the DPs between the upstream and downstream pressure taps of the second and third 3/8" LFE tubes. A final pair of automated pneumatic valves allowed for the shorting of the selected pressure transducer to measure the zero-offset DP reading.

### 3.6.1 Differential-Pressure Transducers and their Calibration

The following two DP transducers were used in this work: an Omega PX938-04WD10V DP transducer with a range of 0-4 in. $H_20$ (~ 0-1000 Pa); and an Omega PX838-40WD10V DP transducer with a range of 0-40 in. $H_20$ (~ 0-10,000 Pa). These two DP transducers will herein be referred to as the PX938 and PX838 transducers. The voltage output from each DP transducer was connected, via a BNC connector box (NI BNC-2110), to a 16-bit data acquisition card (NI PCI-6221), which had a maximum sampling frequency of 250 kHz and variable analog voltage input ranges of ± 1, 2, 5, and 10 VDC. The DP measurements were taken with this data acquisition card set to ±10 VDC, and 128 samples were taken at a frequency of 8 Hz. For each selected DP measurement, once the corresponding pair of automated valves was activated, a 10-second delay was provided prior to recording any data, for stabilization of the pressures within the various connecting lines (and achieving effectively steady-state transducer output voltage).

Prior to performing any DP measurements, both the PX938 and PX838 DP transducers were calibrated using an Askania manometer (see Figure 3.18) with an applied differential pressure range of 0-150 mm $H_2O$. In the calibration set-up, the high- and low-pressure ports of the transducer were each connected to the corresponding ports of the Askania manometer via two Swagelok T-junctions made of stainless steel. For zeroing this manometer, the third port of each of these T-junction was attached to a Swagelok stainless-steel quarter-turn plug valve, which allowed both ports of the manometer to be connected to the ambient environment inside the laboratory. To minimize any noise in

the transducer signal due to vibrations of the supporting table or stand, the transducer was placed on a piece of 3" foam (sponge).

Figure 3.18: Illustration of the Askania manometer used in this work

Before starting the calibration, the computer (containing the NI PCI-6221 data acquisition card) and data acquisition unit (HP 3497A) were powered on and the transducer was supplied with 20.0 VDC from a laboratory-grade power supply. A minimum of two hours was given for all the electronics to warm up and stabilize. A calibrated thermocouple was placed on the Askania manometer to measure the temperature of the water in its reservoir. This temperature was used to determine the density of the water [Kell (1975)], which was then used in the calculation of the applied differential pressure. The Askania manometer was first levelled and subsequently zeroed. Once zeroed, the plug valves used for this task were closed, the zero offset height of the Askania manometer was noted (in mm $H_20$), and the zero-output voltage of the transducer was measured. The Askania manometer was then sequentially set to a series of desired values of differential pressure. For each such desired differential pressure, the transducer output voltage was monitored, allowed to stabilize, and then the reading was recorded. Two full calibration tests were performed for each of the two differential-pressure transducers.

For each transducer, all of the data from the two full calibration tests (the applied differential pressures and the corresponding calibration voltages) were used for a least-squares linear-curve-fit passing through the (0,0) data point. These calibration data and the linear-curve-fits for the two transducers are plotted in Figure 3.19. The resulting values of the calibration constants are 99.1274 Pa/V (PX938) and 980.782 Pa/V (PX838). For each transducer, the experimental uncertainty was taken as the average absolute percentage differences between the applied differential pressures (from the Askania

manometer) and the corresponding differential pressures obtained from the calibration constant and using the measured voltage. These experimental uncertainties for the PX938 and PX838 transducers were found to be 1.98% and 0.079%, respectively.

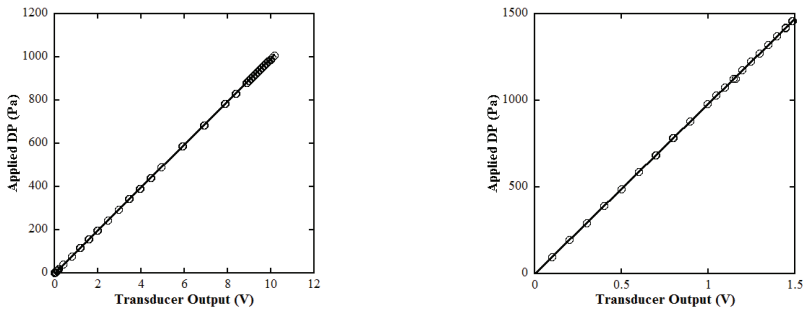


Figure 3.19: Omega PX938 (left) and PX838 (right) calibration data and linear-curve-fit

### 3.6.2 Absolute Pressures

The absolute atmospheric air pressure in the laboratory, $p_{atm}$, was measured using an electronic barometer (Vaisala PTA 427; accurate to ±40 Pa). This barometer was supplied with 20.0 VDC; its output voltage, $V_{baro}$, in the range 0-5.0 VDC, was measured using an HP 3497A data acquisition unit. The $p_{atm}$ [Pa] was calculated using the following calibration equation: $p_{atm} = 133.367\left(39.3064 V_{baro} + 599.875\right)$. The absolute pressures at various points of interest in the airflow path were calculated by subtracting P8 and other appropriate DPs (discussed earlier; see Figure 3.17) from the atmospheric pressure, $p_{atm}$.

## 3.7 Air Properties

The values of the density and dynamic viscosity of the air within the experimental apparatus were determined from the corresponding measurements of the absolute pressure and temperature and correlations fitted to well-established reference values [Incropera et al. (2007); Afara (2012)]. The absolute pressure was measured using the procedures outlined in the previous section. The temperature was measured using calibrated Type-E (chromel-constantan) 30-gauge thermocouples, installed at 12 locations (labelled T##) in the experimental apparatus, schematically depicted in Figure 3.20. The thermocouples used in this work were constructed and calibrated in the Heat Transfer Laboratory by

Afara (2012), over the range 5-62 ºC with an accuracy of ±0.02 ºC, and connected to an Omega thermocouple connector box, which was then connected to the HP 3497A data acquisition unit. Each temperature measurement was taken as the average of 25 readings of the corresponding thermocouple, taken at a frequency of 4 Hz, using a specially designed LabVIEW program written by Afara (2012). With reference to the notation in Figure 3.20, starting at the upstream end of the experimental apparatus, the above-mentioned thermocouples (T40-T51) were used to measure temperature at the following locations: T49, inlet to the air tunnel; T40, test-section inlet; T50, test-section outlet; T51, the Venturi-tube inlet; and T41-T48, the eight LFE tubes.

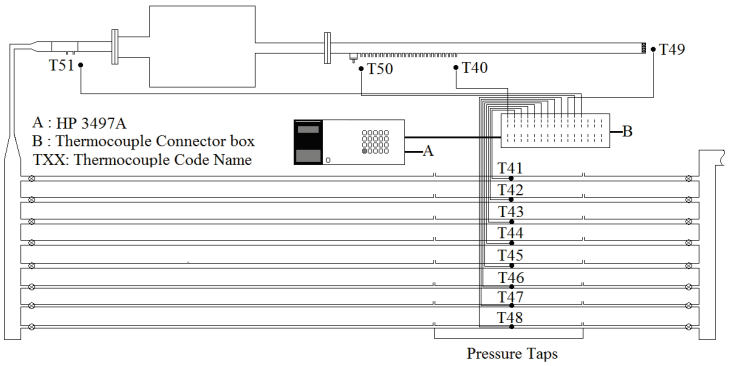


Figure 3.20: Schematic illustration of the locations of the temperature measurements

## 3.8 Set-up for Permeability and Dimensionless Form-Drag Coefficient

In this set-up, the air channel was configured for airflow only through the metal foam in each of the test-section c-channels discussed earlier. In this configuration, with reference to Figure 3.7, the wall-static-pressure-tap plate (P12) was positioned to allow measurement of the wall-static-pressure distribution over the full length (18") of the metal foam in the test-section c-channels. The inlet section of the air channel was configured to the nominal 1/2" height, and the test section was configured to the nominal 1/8" open-domain height. To ensure the air did not flow within the open-domain of the test section in this configuration, a variety of gaskets were used. The gaskets were purchased from Stockwell Elastomerics Inc. They were made of BISCO® BF-2000 ultra-soft silicone foam and had thicknesses that were approximately 40-50% larger than the measured open-domain gap heights of the test-section metal-foam c-channels, to ensure proper

sealing on assembly, without crushing or compressing the metal foam. Furthermore, the gaskets were custom-matched to each test-section metal-foam c-channel to ensure proper sealing along the side-walls of these channels.

The pattern of holes on the wall-static-pressure-tap plate (P12) was also water-jet cut into each of the above-mentioned gaskets. The holes in these gaskets were 1/16" (~1.6 mm) in diameter, which was twice the diameter of the wall-static-pressure tap holes; this was done to ensure the gasket would not block the pressure-tap holes. The holes in the gaskets were not made any larger to make sure that they had no (or only a very minimal) effect on the differential static-pressure readings obtained using the pressure taps. However, there was a possibility that these holes could close when the gaskets were compressed to seal the open-domain gap in the test-section c-channels. To avoid such closure, a small tube (Scanivalve TUBN-031), 0.031" in diameter and 0.75" (~19 mm) in length, was inserted into each pressure-tap hole prior to installing the gasket. As the wall-static-pressure-tap plate (P12) formed the bottom of the channel, to stop these small (0.031" diameter) tubes from falling into the pressure-tap holes, a size-001 o-ring (McMaster-Carr 9452K111) was placed around each of these small tubes. This technique worked perfectly, as after each experiment with this set-up, upon disassembling the test section, it was observed that none of the small tubes had fallen into the pressure-tap holes, and also none of them had protruded past the surface of the gasket into the metal foam.

## 3.9 Wall-Shear-Stress Sensor

A wall-shear-stress sensor was used for determining instantaneous and time-averaged values of the shear stress at the top wall of the problems of interest illustrated in Figure 2.1 (in the experimental apparatus, the air channel was set up so that this wall corresponded to the lower wall of the test section; in particular, the portion of it depicted as plate P18 in Figure 3.7).

### 3.9.1 Initial Design

A wall-shear-stress sensor initially designed, fabricated, and used by Afara (2012) is schematically illustrated in Figure 3.21.

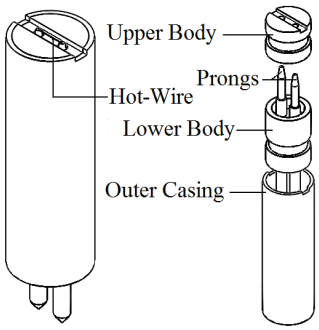


Figure 3.21: Schematic of a wall-shear-stress sensor designed by Afara (2012) - assembled view (left) and exploded view (right), not to scale

In the wall-shear-stress sensor designed by Afara (2012), which was based on an earlier design of a cylindrical-cavity-hot-wire probe by Spazzini et al. (1999), a 2.5μm-diamter tungsten hot-wire was soldered to two prongs with tips flush-mounted with the top surface of the sensor (Figure 3.21). The prongs were made of gold-plated size-12 sewing needles (John James JG12012), with one end of each prong sanded down to allow soldering of the tungsten hot-wire. Underneath the hot-wire was a narrow, 1 mm wide, and shallow, 0.1 mm deep, rectangular cavity, which reduced the heat loss from the hot-wire to the substrate, and also enhanced the frequency response of the sensor as compared to conventional hot-film sensors. The upper and lower bodies of the sensor were fabricated from a glass-mica composite material (Crystex Composites MM400), and then inserted and glued into the outer casing, made of a seamless stainless steel tube (New England Small Tubes) with outer and inner diameters of 0.025" and 0.210", respectively. This tube provided support to and protected the upper and lower bodies of the sensor, and it also facilitated insertion of the sensor into the bottom wall of the test section (plate P18 in Figure 3.7). The bottoms of the two prongs were designed to enable an electrical connection to a standard TSI single-normal hot-wire probe support (TSI 1150-18).

### 3.9.2 Improved Design

The wall-shear-stress sensor designed by Afara (2012) performed quite well, as described in Afara (2012) and Afara et al. (2013), so many of its key features, described in the previous subsection, were retained. However, it was redesigned, jointly by Mr. Afara and the author, to incorporate the following improvements: reduction in the number of parts;

simplification in the machining and assembly processes; elimination of third-party components (TSI probe support); an air-tight seal when inserted into the bottom wall of the test section (plate P18 illustrated in Figure 3.7); and improved alignment of the rectangular cavity below the hot-wire with identical notches (cuts) in the outer casing of the sensor, leading to a better collapse of the calibration data for two different orientations of a vector normal to the hot wire of the sensor with respect to the main flow direction, 0º and 180º (in principle, they should give identical measurements of the wall-shear stress). The redesigned sensor is illustrated in Figure 3.22.


Figure 3.22: Schematic of redesigned sensor (left) and photograph of the hot-wire (right)

In the redesigned sensor (Figure 3.22), an o-ring groove was incorporated into the outer tube of the lower body (size-011 Silicone 70, 0.312"x0.437"x0.070"), to provide an airtight seal when the sensor was inserted into the lower wall of the test section (plate P18 in Figure 3.7). A 3/16" (~4.8 mm) diameter glass-mica rod (Crystex Composites MM400), 0.5" (12.7 mm) in length, was inserted within the upper body, and fixed in place with JB Weld glue (24 hours were then allotted for the JB Weld glue to harden fully). The glass-mica is a delicate material to machine, so inserting and gluing it into the upper body provided good support over its whole length and greatly facilitated the machining (in the glass mica material) of the rectangular cavity and also the holes for the prongs. These machining tasks were done in one single set-up on a milling machine, ensuring that the hot-wire was as parallel as possible with the walls of the rectangular cavity, which was also well aligned with the corresponding notches (cuts) in the outer casing of the upper body.

In the redesigned sensor, the ends of the prongs away from the soldered hot-wire were not connected to a TSI probe support. Rather, a piece of insulated 22-gauge solid aluminum wire was soldered to this end of each of the two prongs; and then the other ends of the two solid aluminum wires were soldered to a 50-Ω impedance Amphenol female BNC connector (Digi-Key Corporation ACX1048-ND). Following these steps, a shorting fixture and a procedure similar to that outlined in Afara (2012) was used to determine the combined electrical resistance of the two prongs of the new sensor, $R_{pr}$. This resistance is needed for calculating the cold-wire electrical resistance of the sensor (which, in turn, is necessary for determining its operating resistance, as is discussed in the next subsection).

Once the combined electrical resistance of the prongs was determined, the following sensor-assembly steps were followed sequentially: i) the female BNC connector was de-soldered from the ends of the two 22 gauge wires (which remained soldered to the prongs at their other ends); ii) the prongs were inserted into the holes drilled for them in the upper body, and they were then pushed through these holes so that their ends protruded from the top surface of the upper body; iii) these ends of the prongs were then pressed against a precision-ground flat gauge block to make them flush with the top surface of the upper body; iv) a low-electrical- and low-thermal-conductivity epoxy (Cotronics EE4525) was then injected into the bottom of the upper body, until all openings and cavities were entirely filled with this epoxy, and the assembly was left undisturbed for 24 hours to allow the epoxy to cure and harden fully; v) the female BNC connector was again soldered to the ends of the two 22 gauge wires; vi) JB Weld glue was applied to the bottom of the assembled upper body and around the threads of the female BNC connector; vii) the upper-body assembly was then inserted through the lower body and mounted within a jig, mimicking the sensor-mounting block used in the test section (discussed in the next subsection), to ensure that the upper and lower bodies are concentrically aligned; and viii) the complete assembly was left undisturbed for another 24 hours to allow full hardening of the JB Weld glue. At this stage, the body of the sensor, its prongs, and connector are completely assembled. A hot-wire was then soldered to the tips of the two prongs (see Figure 3.22), using a special procedure that is outlined fully in Afara (2012), so it is not be repeated here.

### 3.9.3 Fixtures and Procedure for Insertion into Test Section

The various fixtures that were designed, constructed, and used for appropriately aligning a stopper plate and safely (and reliably) flush-mounting the wall-shear-stress sensor in plate P18 of the test section (see Figure 3.7) are illustrated below in Figure 3.23. These fixtures and the related procedures were adapted from those proposed earlier by Afara (2012). The adaptations were needed to accommodate the changes incorporated in the body of the redesigned sensor and also in the newly designed test section.

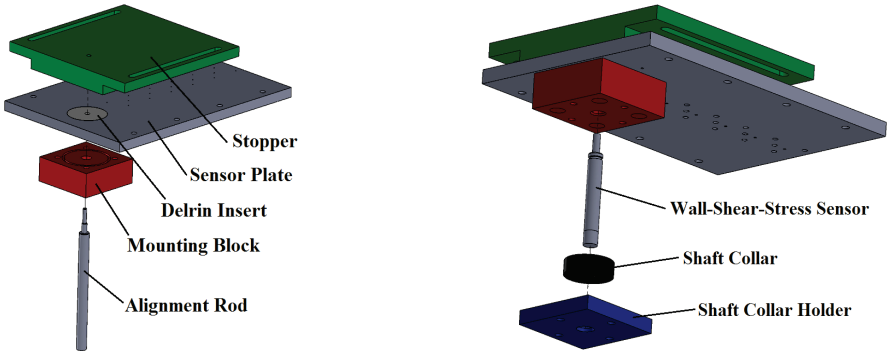


Figure 3.23: Fixtures used for aligning the stopper plate (left) and flush-mounting of the wall-shear-stress sensor (right)

With reference to the fixtures illustrated in Figure 3.23, the wall-shear-stress sensor was flush-mounted in a cylindrical Delrin insert, press-fitted and glued in the plate P18 (Figure 3.37). The sensor-mounting block (installed on to plate P18) incorporated a captivated o-ring on its top surface. A photograph of the wall-shear-stress sensor flush-mounted in the Delrin insert of plate P18 is given in Figure 3.24.

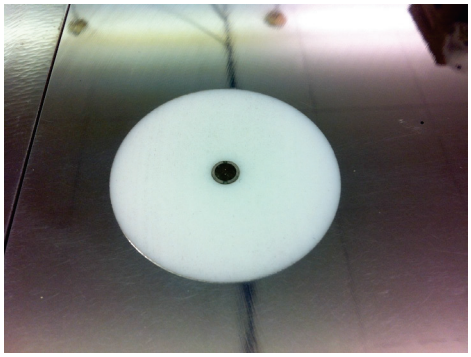

Figure 3.24: The wall-shear-stress sensor flush-mounted in the Delrin insert of plate P18

### 3.9.4 Related Instrumentation and Settings

The wall-shear-stress sensor was connected to a constant-temperature anemometer (CTA; DISA 55M01) using a 5 m BNC cable (RG58/U-50Ω). The electrical resistance of this cable was compensated for by connecting it to the CTA, shorting it, and then zeroing the CTA. With the sensor connected, the CTA was switched to the "resistance measurement" position and the electrical resistance of the sensor under ambient conditions, $R_{amb}$, was measured. The cold-wire electrical resistance (at the room temperature), $R_a$, was found by subtracting the previously measured prong resistance (discussed earlier in subsection 3.9.2), $R_{pr}$, from the electrical resistance of the sensor under ambient conditions.

The operating electrical resistance of the hot-wire, $R_{op}$, was obtained by multiplying the cold-wire resistance ($R_a$) by the selected overheat ratio, $\alpha$ (= $R_{op} / R_a$). In conventional hot-wire anemometry, typically, $\alpha$ = 1.8 is selected for optimal operation of the sensor [Brunn (1996)]. In this work, however, an overheat ratio of 1.5 was selected for the hot-wire of the wall-shear-stress sensor for the following reasons: 1) several preliminary experiments with different overheat ratios showed that when it was set to 1.5, the most stable and consistent operation of the sensor was obtained; and 2) observations of the sensor under a microscope showed that when it was operated with an overheat ratio above 1.5, the hot-wire did not stay taut between the two prongs, but deflected or buckled due to the related thermal expansion (it should be noted here that the prongs could not move outward to take up the thermal expansion of the hot-wire, as over most of their lengths, except for the portions immediately below their tips, they are glued into the holes in the upper body of the sensor). It should also be noted that when the CTA is first set to the "run" position, there is a spike in the measured voltage, which then decreases slightly to a steady-state value after approximately 20-30 seconds. This behaviour can be attributed to excess heat losses from the hot wire to the relatively cool substrate when it is first powered on, and the time required for both the wall-shear-stress sensor and the Delrin insert in plate P18 to reach essentially steady temperatures.

In this work, the sensor was aligned (that is, its hot-wire was oriented) to yield the maximum CTA voltage output at a test-section Reynolds number of approximately 2000, and then this alignment was maintained during all subsequent calibrations and measurements. As the calibrations and all subsequent measurements were done with the sensor inserted in the same plate (P18) and maintained in the same position, heat losses from the hot wire to the Delrin piece (inserted in plate P18) were intrinsically taken into account, and there was also no need for concern about any errors resulting from angular or flush-mounting off-sets. Nevertheless, special care was taken to ensure that the sensor was indeed flush-mounted and remained in the aforementioned alignment during the calibrations and also during all subsequent measurements.

### 3.9.5 Calibration

This task was done using the calibration c-channel discussed earlier in Subsection 3.3.2, with the test section configured to achieve three different open-domain heights. For laminar flows ( $\mathrm{Re} \leq 2000$), the analytical solution (Subsection 2.6.1, Eq. 2.30) was used to obtain the following relationship between the time-averaged wall-shear stress, $\overline{\tau}_w$, and the average velocity, $u_{av}$, in the test section:

$$\overline{\tau}_w = \frac{\mu u_{av}}{2\overline{U}H}\left[1 - 8\sum_{n=0}^{\infty}\frac{1}{\lambda_n^2 \cosh\left(\lambda_n \Lambda\right)}\right]$$
$$\overline{U} = \frac{1}{12} - \frac{8}{\Lambda}\sum_{n=0}^{\infty}\frac{\tanh\left(\lambda_n \Lambda\right)}{\lambda_n^5}; \qquad \Lambda = \frac{W_{channel}}{2H}; \quad \lambda_n = (2n+1)\pi \tag{3.9}$$

For fully developed turbulent flows in straight ducts of rectangular cross-section, an empirical correlation proposed by Zanoun et al (2003) was used for calibrating the wall-shear-stress sensor. Their correlation applies to an aspect ratio (width/height) of 12:1, which corresponds to the lowest value of aspect ratio considered in this work, and values of Reynolds numbers (based on wall-friction velocity) greater than those investigated in this work. Thus, before using this correlation for calibrating the wall-shear-stress sensor, it was benchmarked for the turbulent flows investigated in this work ($4000 \leq \mathrm{Re} \leq$

~14,000): this was done by using the measured time-averaged wall-static-pressure distributions in the test section to calculate the corresponding values of the time-averaged wall-shear stress, and then comparing these values to those yielded by the aforementioned correlation. The results of these benchmarking tests showed that the aforementioned correlation was accurate to within the ±2.5% of the experimental data for the turbulent flows investigated in this work, so it was adopted as the reference in the corresponding runs for calibrating the wall-shear-stress sensor (the aforementioned time-averaged wall-static-pressure measurements were not done in the calibration runs, to avoid making them overly time consuming). The empirical correlation of Zanoun et al. (2003), adapted to the notations and variables used in this work, is presented in the following equation:

$$\overline{\tau}_w = 0.029\rho u_{av}^2 \,\mathrm{Re}_m^{-0.243}; \quad \mathrm{Re}_m = \left\{\rho u_{av}\left(H/2\right)\right\}\Big/\mu \tag{3.10}$$

For each configuration of the test section used in the calibration tests, many preliminary experiments were performed to determine the appropriate number and frequency of the samples of the voltage supplied to the wall-shear-stress sensor by the CTA. These rates and total number of samples are summarized in Table 3.6. In this table, a block of data is defined as one set of samples taken at the specified sampling frequency. For example, for the 1/8" height of the test-section open-domain, one block consists of 131072 samples taken at a sampling frequency of 80000 Hz. For each test-section configuration, the sensor voltage was sampled for approximately 60 seconds during the calibration tests and for roughly 20 seconds while performing the final measurements.

| | Calibration | | | Final Measurements | | |
|---|---|---|---|---|---|---|
| **Test-Section Open-Domain Height** | **Blocks** | **Samples in Block** | **Frequency (Hz)** | **Blocks** | **Samples in Block** | **Frequency (Hz)** |
| **1/8" (3.175 mm)** | 40 | 131072 | 80000 | 100 | 16384 | 80000 |
| **1/4" (6.350 mm)** | 25 | 131072 | 50000 | 65 | 16384 | 50000 |
| **1/2" (12.70 mm)** | 20 | 65536 | 20000 | 25 | 16384 | 20000 |

Table 3.6: Rates and total number of samples of the wall-shear-stress sensor voltage

The laminar-flow solution (Eq. 3.9) is applicable for $\mathrm{Re} \leq 2000$; and Eq. (3.10), the correlation of Zanoun et al. (2003), is applicable for $\mathrm{Re} \geq 4000$. In the transition-flow regime ($2000 < \mathrm{Re} < 4000$), no specific benchmark or reliable correlation was available, and numerous preliminary tests showed that the fluid flow and the related wall-shear stress could not be assumed to be steady (even statistically). Thus, in the calibration runs, data corresponding to flows in the transition-flow regime were discarded. Instead, using test-section configurations with three different open-domain heights (see Table 3.6), and a series of laminar ($\mathrm{Re} \leq 2000$) and turbulent ($\mathrm{Re} \geq 4000$) flows in each of them, a full set of calibration data points, with values of the time-averaged wall-shear stress uniformly distributed (effectively) in the range 0.02 Pa $< \overline{\tau}_w <$ 1.8 Pa, were obtained. It was then assumed that the hot-wire of the sensor, which always resides inside the viscous sub-layer, responds to the wall-shear stress that it is exposed to, regardless of the flow regime.

In the above-mentioned calibration runs, 21-24 values of Reynolds number were considered for each test-section configuration (only data points in the laminar and turbulent regimes were retained); and the calibration runs were done before and after performing measurements with the metal-foam test sections. The air temperature within the laboratory was meticulously monitored in all runs, and once the test section was configured for a particular calibration run, a minimum of one hour was given to allow the air temperature within the test section to reach a steady-state value and the ambient resistance of the sensor, $R_{amb}$, to stabilize.

In numerous preliminary tests, following recommendations in conventional hot-wire anemometry [see Brunn (1996), for example], the square of the time-averaged voltage supplied to the hot-wire by the CTA ($E^2$) was plotted against the time-averaged wall-shear stress ($\overline{\tau}_w$). However, this practice produced a fair amount of scatter, as can be seen in Figure 3.25 in which the calibrations data points from 36 individual calibration runs are presented. In this context, an analysis of the conditions and data pertaining to these preliminary tests led to the following findings: 1) the temperature could be maintained to within ±0.15 ºC about a mean temperature for a given experimental run; however, over a

month-and-a-half or so of performing experiments, the temperature was approximately 23 ºC ±1.5 ºC; 2) the corresponding changes in the cold-wire electrical resistance ($R_a$) and the operating electrical resistance of the hot-wire ($R_{op} = \alpha R_a$) for a fixed selected value of the overheat ratio ($\alpha$ = 1.5) were not insignificant; and 3) these changes in the value of $R_{op}$ produced corresponding notable changes in $E^2$ for the same values of $\overline{\tau}_w$, and the aforementioned scatter in the calibration data. Based on these findings, it was deduced that plotting the time-averaged power supplied to the hot-wire of the sensor by the CTA ($E^2 / R_{op}$) against $\overline{\tau}_w$ would reduce the aforementioned scatter in the calibration data. This deduction was based on the realization that $E^2 / R_{op}$ is proportional to difference in the operating temperature of the hot-wire and the air temperature, which would be affected only negligibly by a variation of ±1.5 ºC in the temperature of the air. Additional tests confirmed this deduction, so it is considered as one of the original contributions of this work. Based on the findings of these preliminary tests, in all final calibration runs, the values of $E^2 / R_{op}$ were plotted against $\overline{\tau}_w$.

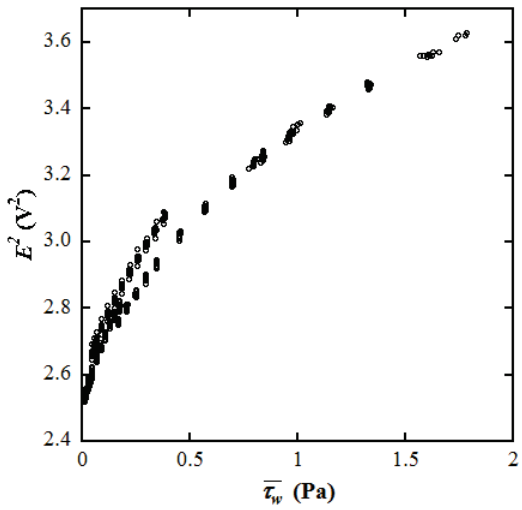


Figure 3.25: $E^2$ versus $\overline{\tau}_w$ calibration data for the wall-shear-stress sensor

The data from the aforementioned 36 individual calibration runs, spanning the above-mentioned three different configurations of the test section (see Table 3.7), are plotted as

$E^2 / R_{op}$ versus $\overline{\tau}_w$ in Figure 3.26. The relatively smooth variation of the calibration points in this figure show that it is, indeed, possible to obtain a calibration curve for the wall-shear-stress sensor that is independent of both the test-section open-domain height and the flow regime. Nevertheless, rather than curve-fitting one correlation to all of the calibration data points, improved curve-fits could be achieved by using two correlations akin to the King's Law [Brunn (1996)], $E^2 / R_{op} = A + B\overline{\tau}_w^n$: one correlation (denoted as "low" in Figure 3.26) was used for $\overline{\tau}_w \leq$ 0.2 Pa; and the other correlation (labelled as "high" in Figure 3.26) was used for $\overline{\tau}_w >$ 0.2 Pa. The calibration coefficients $A$, $B$, and $n$ were determined to be 0.114438, 0.0441871, and 0.64662, respectively, for the "low" correlation; and 0.105426, 0.0482701, and 0.412647, respectively, for the "high" correlation. The root-mean-square of the percentage differences between the experimental (obtained in the calibration runs) and predicted values of $E^2 / R_{op}$ for the same value of $\overline{\tau}_w$ were found to be 6.94% and 4.63% for the "low" and the "high" correlations, respectively.

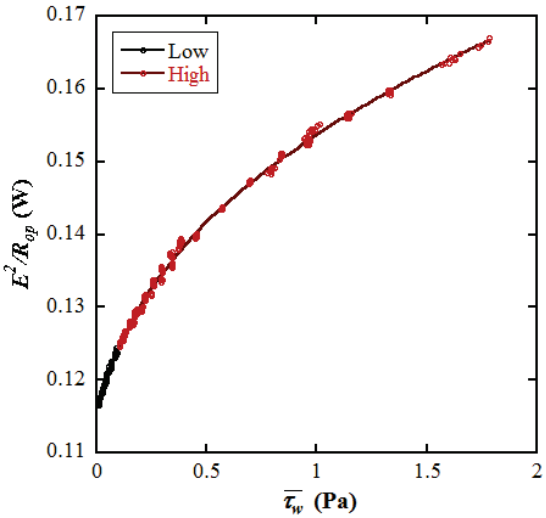


Figure 3.26: $E^2 / R_{op}$ versus $\overline{\tau}_w$ calibration data and correlations for the wall-shear-stress sensor

# Chapter 4 – Results and Discussion

In this chapter, results obtained from the following aspects of this work are presented and discussed: 1) benchmarking tests carried out prior to undertaking the final experiments; 2) characterization of the porous metal foams used in this work; 3) experiments undertaken for determining the permeability and dimensionless form-drag coefficient for the porous metal foams, and a Darcy friction factor based on the ligament diameter for fully developed flows in straight rectangular ducts filled with these metal foams; and 4) experiments on flows in adjacent open and porous domains.

## 4.1 Benchmarking Tests

The results presented and discussed in this section pertain to tests undertaken to benchmark the following: 1) gradients of time-averaged wall-static pressure; 2) establishment of fully developed flow in the air channel upstream of the test section; 3) the correlation of Zanoun et al. (2003); and 4) wall-shear-stress measurements when the sensor is operated over lengthy periods of time.

### 4.1.1 Gradients of Time-Averaged Wall-Static Pressure

As was discussed in Chapter 3, Section 3.6, two differential-pressure (DP) transducers were used in this work to measure the distributions of the time-averaged drop in the wall-static pressure in the inlet and test sections of the air channel (see Figure 3.1 and 3.7): an Omega PX938-04WD10V DP transducer (PX938) with a range of 0-4 in. $H_20$ (0~1000 Pa); and an Omega PX838-40WD10V DP transducer (PX838) with a range of 0-40 in. $H_20$ (0~10000 Pa). The experimental uncertainties for the PX938 and PX838 transducers were found to be 1.98% and 0.079%, respectively.

The gradients of the time-averaged wall-static-pressure obtained from the above-mentioned DP measurements were benchmarked using comparisons to the corresponding values (for the same values of Reynolds number) obtained from the analytical values for laminar flows (see Eqs. 2.30 and 3.9) and the Jones (1976) correlation for turbulent flows

(see Eq. 2.33). For laminar flows, the following results were obtained in these benchmarking tests: the average absolute percentage difference between the values of the corresponding measured and analytical pressure gradients was 8.34%; the highest of these values (as high as 19.56%) pertained to two data points obtained with the air channel configured to the nominal height of 1/2" (see Table 3.2), for which the DPs measured were of the order of 0.2-0.5 Pa and the accuracy of PX938 DP transducer was quite poor; exclusion of these two data points brought the average absolute percent difference down to 3.96%, which was comparable to the uncertainty associated with the values of the experimentally determined mass flow rate (used in the calculation of the values of the analytical pressure gradient). For the turbulent flows, the benchmarking tests yielded the following results: the average absolute percentage difference between the values of the corresponding pressure gradients obtained from the measurements and the correlation of Jones (1973) was 13.21%, which is higher than the ±5% uncertainty associated with this correlation. This higher percentage difference is caused by a contribution to it by the uncertainty associated with the gap (open-domain) height of the calibration c-channel (discussed earlier in Chapter 3, Section 3.3.2).

### 4.1.2 Establishment of Fully Developed Flow Upstream of the Test Section

Benchmarking tests were undertaken to ensure this fully developed flow condition was indeed established, for all configurations of the test section and the full range of Reynolds number investigated in this work. Sample results of these tests, for the test section of nominal 1/4" height (see Table 3.2) are presented in Figure 4.1. In this figure, the essentially linear variations of the measured drop in time-averaged wall-static pressure, $\Delta p = (p_{ref} - p)$, with the axial coordinate, $x$, in the inlet section of the air channel (see Figures 3.1 and 3.7), for the highest values of the Reynolds number considered in both the laminar ($\mathrm{Re} = 1958$) and turbulent ($\mathrm{Re} = 10870$) flow regimes, demonstrate that fully developed flow was established upstream of the test section. Similar results were obtained for all other air channel configurations (see Table 3.2). As these results pertain to the maximum values of the Reynolds number for the laminar and turbulent flows considered,

it was assumed that fully developed conditions were also achieved upstream of the test section for all other flows investigated in this work.

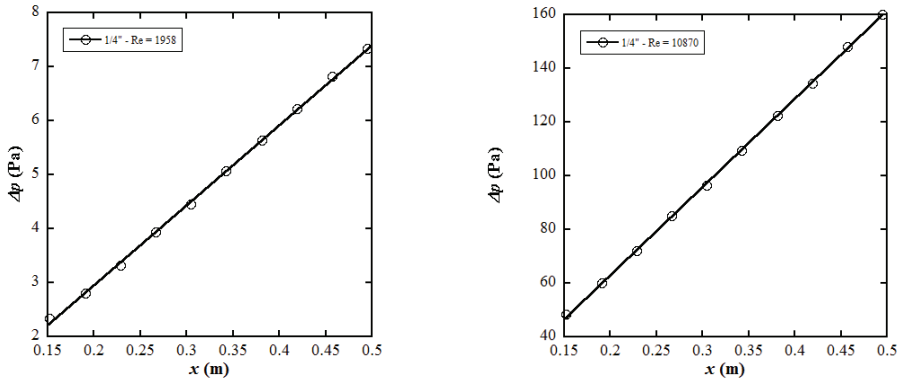


Figure 4.1: Variation of $\Delta p = (p_{ref} - p)$ with the axial coordinate, *x*, in the inlet section of the air channel, for a nominal height of 1/4", for Re = 1958 (left) and 10870 (right)

### 4.1.3 Correlation of Zanoun et al. (2003)

The empirical correlation of Zanoun et al. (2003), presented in Eq. 3.10, gives the time-mean wall-shear-stress, $\overline{\tau}_w$, as a function of a Reynolds number, $\mathrm{Re}_m = \rho u_{av}(H/2)/\mu$. Before this correlation was used for calibrating the wall-shear-stress sensor, it was benchmarked to assess its applicability to the turbulent flows investigated in this work. These benchmarking tests were done in an open (no metal foam) test section, with the air channel configured for a nominal 1/2" height (see Table 3.2 for related details). In particular, for Reynolds number, $\mathrm{Re} = \rho u_{av} D_h / \mu$, in the range $4000 \leq \mathrm{Re} \leq 14{,}000$, the measured time-mean wall-static-pressure distributions in the test section (fully developed flow) was used in an overall force balance to calculate the corresponding values of the time-mean wall-shear-stress, and then these values were compared to those yielded by the correlation of Zanoun et al. (2003).

The results of these benchmarking tests are presented in Table 4.1. The absolute values of the percentage difference between the wall shear stress obtained using the gradient of the measured time-mean wall-static-pressure distribution, $\overline{\tau}_{w-dp/dx}$, and that yielded by the correlation of Zanoun et al. (2003) for the same Reynolds number, $\overline{\tau}_{w-Zanoun}$, show the

following: maximum value of 5.10% at Re = 4042.4; and an average value of 1.46%, which is within the stated uncertainty of ±2.5% of the aforementioned correlation. Based on these results, the correlation of Zanoun et al. (2003) was considered to be satisfactory for use in the experiments undertaken for calibrating the wall-shear-stress sensor.

| Re | $Re_m$ | $\tau_{w\text{-}dp/dx}$ (Pa) | $\tau_{w\text{-}Zanoun}$ (Pa) | \|% Diff\| |
|---|---|---|---|---|
| 4042.4 | 1095.30 | 0.0417 | 0.0439 | 5.10 |
| 5062.5 | 1371.70 | 0.0635 | 0.0653 | 2.66 |
| 6124.7 | 1659.50 | 0.0906 | 0.0913 | 0.82 |
| 7100.1 | 1923.80 | 0.1153 | 0.1184 | 2.64 |
| 8109.0 | 2197.20 | 0.1474 | 0.1496 | 1.47 |
| 9135.3 | 2475.30 | 0.1834 | 0.1847 | 0.71 |
| 10057.0 | 2725.10 | 0.2188 | 0.2191 | 0.13 |
| 11056.0 | 2995.80 | 0.2579 | 0.2592 | 0.48 |
| 12009.0 | 3253.80 | 0.3016 | 0.3003 | 0.42 |
| 12823.0 | 3474.50 | 0.3386 | 0.3368 | 0.54 |
| 13810.0 | 3742.10 | 0.3885 | 0.3844 | 1.06 |
| | | | **Average \|% Diff\|** | 1.46 |

Table 4.1: Results of test undertaken to benchmark the correlation of Zanoun et al. (2003)

### 4.1.4 Wall-Shear-Stress Measurements

When the wall-shear-stress sensor was used for collecting data for fluid flow in the test sections with adjacent open and porous domains, for each combination of porous metal foam and test-section open-domain height, the following sequence of experiments were conducted: 1) calibration of the wall-shear-stress sensor; 2) measurement of all relevant experimental data; and 3) another calibration of the wall-shear-stress sensor. Including equipment warm-up and channel set-up times, each of the above-mentioned sequence of experiments could take approximately 16 hours. During this time, the air temperature was maintained to within ±0.15 ºC, about a mean temperature for a given experimental run. Furthermore, over the month and a half of performing experiments, the temperature was maintained at 23 ºC ±1.5 ºC. Although this level of temperature stability may be considered quite acceptable, benchmarking runs were undertaken to assess the performance of the wall-shear-stress sensor over a time period of approximately 16 hours. For this task, the test section was configured to each desired open-domain height using the calibration c-channel. For each such configuration, absolute percentage differences

between the measured time-averaged wall-shear-stress values obtained using the sensor over the full range of values of the Reynolds number and the corresponding values yielded by the analytical solution, for laminar flows, and the Zanoun et al. (2003) correlation, for turbulent flows, were examined.

For laminar flows, the above-mentioned percentage difference could be as high as 18.16% when data from two laminar-flow runs for the nominal open-domain height of 1/2" were included; however, if the data from the two aforementioned laminar-flow runs were excluded, the average percentage difference reduced to 7.27%, which is comparable to the 6.94% uncertainty in the 'low' calibration curve of the wall-shear-stress sensor (see Subsection 3.9.5). In this context, it should be noted that in all of the laminar-flow benchmarking runs, values of the wall shear stress were all below 0.2 Pa and fell within the 'low' calibration range. It should also be noted that large absolute percentage differences were found, as high as 26.17%, for wall-shear-stress values below 0.02 Pa. For turbulent flows, the average value of the above-mentioned percentage difference over all benchmarking runs was 4.03%, which is within the uncertainties of 6.94% and 4.63% associated with the 'low' or 'high' calibration curves, respectively, for the wall-shear-stress sensor (see Subsection 3.9.5). The highest value of the above-mentioned percent difference for all turbulent-flow benchmarking runs was 13.46%. These results of the benchmarking runs were considered as confirmation that the wall-shear-stress sensor performed satisfactorily (within its stated uncertainty) over the above-mentioned 16-hour time periods, except when very low wall-shear-stress values ($\leq$ 0.02 Pa) were measured.

## 4.2 Metal-Foam Characterization

In this section, the results of the experiments undertaken to determine the geometrical aspects and the porosity of the porous metal foams used in this work are presented.

### 4.2.1 Geometric Aspects

The measured values of the following geometric dimensions of the test-section c-channels with the porous metal foams (see Figure 3.9) are summarized in Table 4.2: open-domain height, $\omega H$; metal-foam-domain height, $(1-\omega)H$; and channel width, $W_{channel}$. All

dimensions are presented in millimeters, and of note is the variation in the metal-foam-domain height (thickness) of each of the METPORE porous metal foams. All such foams purchased for this work (see details in Section 3.2) were stated by the manufacturers to have a nominal foam thickness of 0.5" (12.7 mm), but the values measured in this work were found to deviate from this nominal height by as much as ±12.26% (the highest deviations were associated with the M20-2 foam). The values of the thickness, $t2$, of the side rails P04 and P05 (see Figure 3.7) which were used for obtaining values of the test-section open-domain height, $(1-\omega)H$, beyond those of just the porous-metal foam c-channels were measured to be 3.1713 mm and 9.6064 mm, respectively.

| Foam / Measurement | M20-1 | M20-2 | M40-1 | M40-2 | M60-1 | M60-2 | ERG40 | Calibration |
|---|---|---|---|---|---|---|---|---|
| $\omega H$ (mm) | 1.5862 | 1.5425 | 2.7776 | 2.7266 | 3.5964 | 4.2857 | 2.8234 | 3.1702 |
| $(1-\omega)H$ (mm) | 14.2872 | 14.3585 | 13.1169 | 13.1897 | 12.3266 | 11.6207 | 12.7000 | --- |
| $W_{channel}$ (mm) | 147.71 | 147.82 | 147.91 | 147.82 | 147.48 | 147.65 | 152.40 | 152.40 |

Table 4.2: Geometric aspects of test-sections c-channels

| Foam / Measurement | M20-1 | M20-2 | M40-1 | M40-2 | M60-1 | M60-2 | ERG40 |
|---|---|---|---|---|---|---|---|
| $d_l$ (µm) | 312.73 | 299.33 | 139.63 | 127.64 | 86.15 | 77.34 | 241.32 |
| Std. Dev. (µm) | 68.08 | 43.74 | 18.24 | 12.40 | 16.27 | 11.29 | 20.74 |
| $d_p$ (µm) | 1427.74 | 1459.60 | 698.44 | 703.00 | 548.61 | 559.47 | 1262.10 |
| Std. Dev. (µm) | 340.62 | 170.31 | 115.38 | 98.64 | 76.43 | 85.76 | 177.27 |
| $d_c$ (µm) | 3069.28 | 3422.12 | 1556.11 | 1605.45 | 1239.78 | 1206.12 | 2758.45 |
| Std. Dev. (µm) | 140.18 | 162.87 | 74.06 | 65.45 | 69.77 | 62.20 | 169.67 |
| Measured PPI | 17.8 | 17.4 | 36.4 | 36.1 | 46.3 | 45.4 | 20.1 |

Table 4.3: Ligament, pore, and cell diameters of the porous metal foams

The measured values of the following dimensional structural parameters of each porous metal foam (see Subsection 3.2.1) used in this work are summarized in Table 4.3: ligament diameter, $d_l$; pore diameter, $d_p$; and the cell diameter, $d_c$. Also included in this table are the standard deviations for each of these dimensional parameters, based on measurements on the following structural features for each porous metal foam: 20 ligaments, 10 pores, and 10 cells. It should be noted that the nominal pores-per-inch (PPI) designation provided by the manufacturer for each porous metal foam is not an accurate

reflection of the actual (measured) PPI value (determined from the measured average pore size): in particular, for ERG40, the measured PPI value is half of its nominal value. This finding confirms that of Onstad et al. (2011), who also concluded that the manufacturer's PPI value is inaccurate. This finding is especially important to note, as many empirical correlations in the literature (including brochures and information supplied by Selee and other manufacturers of porous metal foams) for determining other geometric aspects of the porous metal foam contain the PPI as a variable.

### 4.2.2 Porosity

For each porous metal foam, three different values of porosity were calculated using the average, minimum, and maximum values of the thickness of its sample. The final results are presented below in Table 4.4. These results showed that the values of porosity based on the values of minimum and maximum thicknesses had a maximum deviation of only ±0.54% from the corresponding value calculated using the value of average thickness. Therefore, for each porous metal foam, the value of porosity was taken as that obtained from the average length, width, and thickness of its sample.

| Measurement\Foam | M20-1 | M20-2 | M40-1 | M40-2 | M60-1 | M60-2 | ERG40 |
|---|---|---|---|---|---|---|---|
| $\rho_{b-avg}$ (kg/m$^3$) | 496.69 | 384.66 | 498.66 | 455.55 | 484.38 | 449.11 | 222.42 |
| $\rho_{b-min}$ (kg/m$^3$) | 502.29 | 391.26 | 500.42 | 462.25 | 515.7 | 470.94 | 223.97 |
| $\rho_{b-max}$ (kg/m$^3$) | 490.97 | 380.68 | 495.35 | 450.82 | 464.51 | 425.67 | 221.74 |
| $\rho_s$ (kg/m$^3$) | 7220 | 7220 | 7220 | 7220 | 7220 | 7220 | 2700 |
| $R = d_i / d_t$ | 0.58 | 0.57 | 0.38 | 0.36 | 0.28 | 0.27 | 0.00 |
| $\varepsilon_{avg}$ | 0.897 | 0.921 | 0.919 | 0.928 | 0.927 | 0.933 | 0.918 |
| $\varepsilon_{min}$ | 0.896 | 0.920 | 0.919 | 0.927 | 0.922 | 0.930 | 0.917 |
| $\varepsilon_{max}$ | 0.898 | 0.922 | 0.920 | 0.928 | 0.930 | 0.936 | 0.918 |

Table 4.4: Measurements pertaining to the porosity of the porous metal foams

## 4.3 Permeability and Dimensionless Form-Drag Coefficient

In this section, some background considerations, the implications of four different approaches for processing the experimental data, the reasons for the adoption of one of

these approaches, and the final results for the permeability and dimensionless form-drag coefficient for the porous metal foams investigated in this work are presented.

### 4.3.1 Background Considerations

Test sections with three METPORE foams (one for each of the three PPI designations), namely, the M20-1, M40-1, and M60-2, and also the ERG40 foam were selected for the experiments that were conducted for determining the coefficients in the interfacial stress-jump condition (discussed later in Section 4.5). The aforementioned three test sections with the METPORE foams were selected because they showed the more consistent open-domain heights, as was determined from 30 measured points in each case.

Two experimental runs were conducted for determining the permeability and dimensionless form-drag coefficient using each of the selected metal-foam test sections; and only one such run was performed using the test sections containing the remaining three METPORE test sections. The following experimental data were collected during each of these experimental runs (11 runs in total): the mass flow rate of air, and the time-averaged wall-static-pressure distributions within the test section. This data was used to determine the superficial velocity flowing through the metal foam and the time-averaged axial pressure gradient in the fully developed region. A plot of the time-averaged axial pressure gradient as a function of the superficial velocity for the test sections containing the M20-1, M40-1, M60-2, and ERG40 metal foams is presented below in Figure 4.2: only the first experimental run for each of these test sections is presented in this figure; and the last digit in the notation used denotes the number of the experimental run, 1 or 2.

The experimental data presented in Figure 4.2 show that the foam with the smallest pore size presented the most resistance to the airflow (as was expected). The ERG40 and M20-1 foams have essentially similar pore sizes, and the resistance that these two foams presented to the flow is almost identical. The difference in pore size for the M40-1 and M60-2 foams was slightly more pronounced than that for the ERG40 and M20-1 foams, and this difference is reflected in the corresponding plots in Figure 4.2.

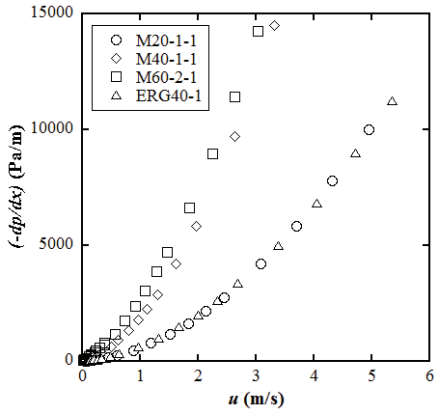


Figure 4.2: Data from four experimental runs for the determination of $K$ and $c_F$

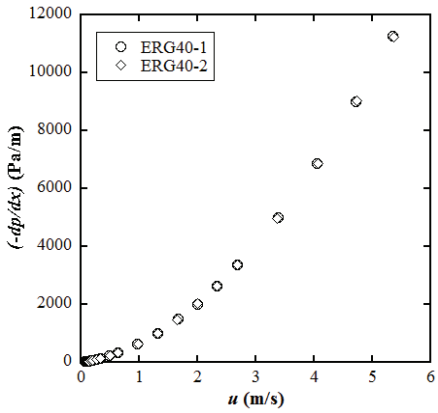


Figure 4.3: Repeatability of experimental data obtained with ERG40 metal foam

The two experimental runs performed for each of the M20-1, M40-1, M60-2, and ERG40 test sections showed very good repeatability of the corresponding data. Figure 4.3 above illustrates this repeatability for the two experimental runs conducted with the test section containing the ERG40 metal foam. Similar plots were obtained for the M20-1, M40-1, and M60-2 metal-foam test sections.

As was discussed in Section 2.5, four different approaches were evaluated for processing the experimental data collected for the determination of the permeability, $K$, and dimensionless form-drag coefficient, $c_F$: Approaches 1 and 2, based on least-squares quadratic-curve-fits to the experimental data; Approach 3, in which the Darcy-Forchheimer equation (Eq. 2.19) is divided by the product ($\mu u$) and cast in the form of

Eq. 2.22, and a least-squares linear-curve-fit to experimentally determined values of the terms in this latter equation; and Approach 4, in which the experimental data that falls in the so-called Darcy regime (form-drag or Forchheimer term is ignored in this regime) is processed first using a least-squares linear-curve-fit to determine the value of $K$, and then this value of permeability and all experimental data points are used in a least-squares quadratic-curve-fit to determine the value of $c_F$. The results obtained with Approaches 1 and 2 are discussed next in Subsection 4.3.2; then, in Section 4.3.3, the results obtained with Approach 4 are discussed; the results obtained with Approach 3, the approach finally adopted in this work, are presented in Subsection 4.3.4; and in Subsection 4.3.5, the final results for $K$ and $c_F$ are presented and discussed.

### 4.3.2 Approaches 1 and 2

Taking the data obtained for the experiments conducted with the ERG40-1 metal foam as an example, the following results were obtained: permeability values of 5.1087E-08 $m^2$ and 5.4822E-08 $m^2$ with Approaches 1 and 2, respectively (an absolute percentage difference of 7.05%); and dimensionless form-drag coefficient values of 0.06449 and 0.06911 with Approaches 1 and 2, respectively (an absolute percentage difference of 6.92%). The curve-fits in both these approaches produced excellent coefficients of determination, 0.99994 and 0.99998 for Approaches 1 and 2, respectively. These results, and similar results obtained with the experimental data obtained with the other metal foams investigated in this work, show that there is an appreciable difference in the values of $K$ and $c_F$ yielded by the Approaches 1 and 2. To further assess these two approaches, the percentage difference between the experimental values of the pressure gradient in the test sections with the different foams and those calculated using the values of values of $K$ and $c_F$ yielded by each of the Approaches 1 and 2 were examined. Based on an examination of the average values of these percentage differences over all data points obtained in the ERG40-1 run, Approach 2 outperformed Approach 1, yielding values of 9.17% and 12.61%, respectively. Similar results were obtained with the data from experimental runs with the other metal foams. The results obtained with these two approaches are compared to those obtained with Approach 3 in Subsection 4.3.4.

### 4.3.3 Approach 4

In this approach, first, tentative values of $K$ and $c_F$ are determined using the above-mentioned Approach 2; then, these values are used to assess the contribution of the Forchheimer term to the axial pressure gradient for each experimental data point. Using this approach, it was determined that for the M60 metal foam, for a few of the data points, the contribution of the Forchheimer term to the axial pressure gradient was as low as 1%; however, for the other metal foams investigated in this work, the limit on this contribution had to be set to about 15% to ensure enough data points for a statistically meaningful calculation of the value of $K$.

Using the above-mentioned technique for the demarcation of the Darcy regime, Approach 4, and the experimental data obtained for the M60 metal foam, the permeability was determined to be 1.0510E-08 $m^2$ and 9.6687E-09 $m^2$ when the above-mentioned limit was set to 5% and 15%, respectively (a percent difference of 8.34%); and the dimensionless form-drag coefficient was determined to be 0.09482 and 0.07964 with the 5% and 15% limits, respectively (a percent difference of 10.58%). These percentage differences were considered too high, so it was concluded that a 15% limit for the contribution of the Forchheimer term to the axial pressure gradient would not produce reliable results for the values of $K$ and $c_F$. It may be practical and viable to fix this limit at 5% or even lower. However, with the experimental apparatus and instrumentation used in this work, for conditions corresponding to limits lower than 5%, it was not possible to measure the mass flow rates and the pressure drops with sufficient accuracy, so Approach 4 was not applicable. Nevertheless, although this approach was not applicable in this work, the author still believes it is worthy of further investigation, possibly in future works with the incorporation of LFEs with smaller tubes and a differential-pressure transducer capable of accurately measuring values of 10 Pa or lower (and related calibration capability).

### 4.3.4 Approach 3

For convenience in the presentation, Eq. 2.22 is repeated below, and the data pertaining to the ERG40-1 run is presented in Figure 4.4:

$$\left(-\frac{dp}{dx}\right)\left(\frac{1}{\mu u}\right)=\frac{1}{K}+\frac{\rho c_F}{\mu\sqrt{K}}u \tag{4.1}$$

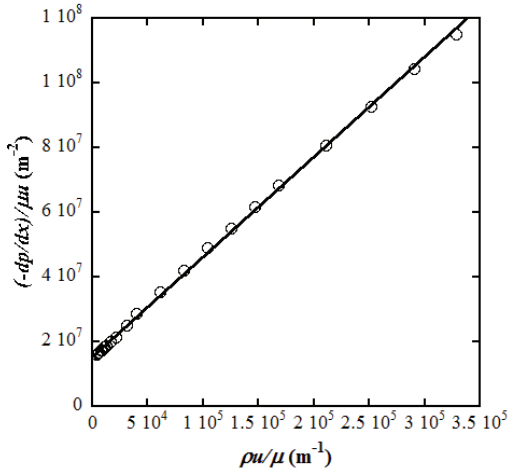


Figure 4.4: Processing of data from experimental run ERG40-1 using Approach 3

As is seen in Figure 4.4, the data points $\{(-dp/dx)/(\mu u)$ and $(\rho u/\mu)\}$ conform very well to a least-squares linear-curve-fit: in quantitative terms, the calculated coefficient of determination for this least-squares linear curve-fit was 0.99918. The corresponding values of $K$ and $c_F$ were determined to be 6.5298E-08 $m^2$ and 0.07885, respectively. To obtain further guidance in the choice of a suitable approach for determining the individual values of $K$ and $c_F$, the percent differences between the experimentally determined values of axial pressure gradient in the fully developed region of the flow within the foams in the test section and those predicted using the values of $K$ and $c_F$ yielded from Approaches 1, 2, and 3 were examined. These results obtained with the data from the ERG40-1 experimental run are plotted in Figure 4.5: they show that Approach 2 is slightly better that Approach 1, but Approach 3 is significantly better than both Approaches 1 and 2 over the lower end of the data range, and the percentage difference it produces remains in a ±5% band over the whole data set. Similar results were obtained from the experimental runs with all of the other foams. Thus, it was decided to adopt Approach 3 for processing the data from all of the experimental runs for the determination of the final values of $K$ and $c_F$.

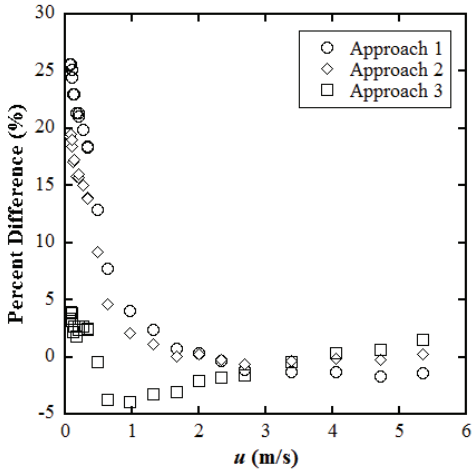


Figure 4.5: Comparison of percentage differences between the measured axial pressure gradient and that predicted using $K$ and $c_F$ values obtained using Approaches 1, 2, and 3 to process the data obtained in ERG40-1 experimental run

### 4.3.5 Final Values

These results are summarized in Table 4.5, in which $K_1$, $K_2$, $c_{F1}$, and $c_{F2}$ denote the values of the permeability and the dimensionless form-drag coefficient calculated from the first and second experimental runs for each of the M20-1, M40-1, M60-2, and ERG40 metal-foam test sections; and the absolute percentage differences between the corresponding values obtained from data from each set of repeatability runs are also presented in this table.

| Foam | $K_1$ (m$^2$) | $K_2$ (m$^2$) | % Diff | $c_{F1}$ | $c_{F2}$ | % Diff |
|---|---|---|---|---|---|---|
| **M20-1** | 9.5394E-08 | 9.5353E-08 | 0.04 | 0.10155 | 0.10166 | 0.11 |
| **M40-1** | 2.4014E-08 | 2.4131E-08 | 0.49 | 0.14840 | 0.15067 | 1.52 |
| **M60-2** | 1.1026E-08 | 1.1029E-08 | 0.03 | 0.09330 | 0.09328 | 0.02 |
| **ERG40** | 6.5298E-08 | 6.4730E-08 | 0.87 | 0.07885 | 0.07815 | 0.89 |

Table 4.5: Repeatability checks on the determination of $K$ and $c_F$

The final values of $K$ and $c_F$ for each porous metal foam used in this work are presented in Table 4.6, along with their uncertainties, $U_K$ and $U_{c_F}$, respectively. All related experimental data are presented in Appendix B.

| Foam / Value | M20-1 | M20-2 | M40-1 | M40-2 | M60-1 | M60-2 | ERG40 |
|---|---|---|---|---|---|---|---|
| $K$ (m$^2$) | 9.5374 E-08 | 1.0480 E-07 | 2.4073 E-08 | 2.2357 E-08 | 1.0785 E-08 | 1.1028 E-08 | 6.5014 E-08 |
| $U_K$ (%) | 1.18 | 1.17 | 0.97 | 1.00 | 0.90 | 0.87 | 1.09 |
| $c_F$ | 0.10161 | 0.09640 | 0.14954 | 0.17852 | 0.12041 | 0.09329 | 0.07850 |
| $U_{cF}$ (%) | 0.64 | 0.64 | 0.59 | 0.59 | 0.75 | 0.82 | 0.61 |
| $Da_{d_l}$ | 0.9752 | 1.1697 | 1.2347 | 1.3723 | 1.4531 | 1.8437 | 1.1164 |

Table 4.6: $K$, $c_F$, and $Da_{d_l}$ values for the porous metal foams used in this work

## 4.4 Friction Factors for Fully Developed Flows in Straight Rectangular Ducts of Uniform Cross-Section Filled with Porous Metal Foams

In Eq. 2.34, expressions were proposed for a Darcy friction factor, $(f_D)_{d_l}$, a Reynolds number, $\mathrm{Re}_{d_l}$, and a Darcy number, $Da_{d_l}$, for fully developed flows in straight rectangular ducts of uniform cross section filled with porous metal foams. For convenience in the presentation, these expressions are presented again below in Eq. 4.2.

$$(f_D)_{d_l} = \frac{(-dp/dx)d_l}{0.5\rho u^2} = \left[\frac{2}{Da_{d_l}}\frac{1}{\mathrm{Re}_{d_l}} + \frac{2c_F}{\sqrt{Da_{d_l}}}\right];\ Da_{d_l} = \frac{K}{d_l^2};\ \mathrm{Re}_{d_l} = \frac{\rho u d_l}{\mu} \qquad (4.2)$$

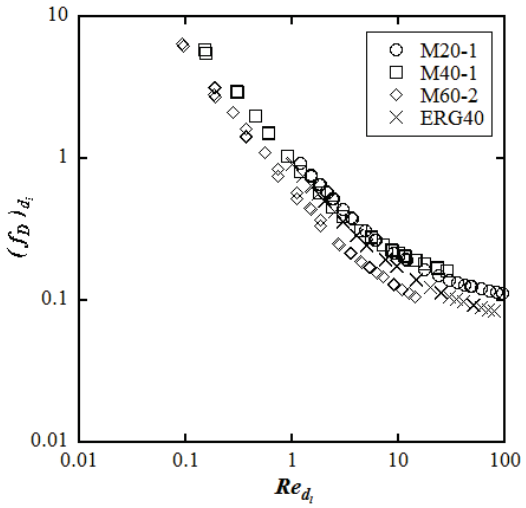


Figure 4.6: Variation of $(f_D)_{d_l}$ with $\mathrm{Re}_{d_l}$ for the M20-1, M40-1, M60-2, and ERG40 porous metal foams (see Table 4.6 for values of $Da_{d_l}$)

Log-log plots of $\left(f_D\right)_{d_l}$ as a function of $\mathrm{Re}_{d_l}$ are presented in Figure 4.6 for the M20-1, M40-1, M60-2, and ERG40 porous metal foams. In these plots, some data points for the M40-1 and M60-2 porous metal foams seem to fall within the Darcy regime (linear variation of $\left(f_D\right)_{d_l}$ with $1/\mathrm{Re}_{d_l}$ in these log-log plots), for $\mathrm{Re}_{d_l} \leq 0.1$; but the majority of the data points fall in a transition regime, between the aforementioned Darcy regime and the Forchheimer regime (constant value of $\left(f_D\right)_{d_l}$ for each porous metal foam), for $\mathrm{Re}_{d_l} > 0.1$. The data points that possibly fall within the Darcy regime pertain to the runs with the M40-1 and M60-2 porous metal foams, which have the smallest values of the pore diameter (among the metal foams considered here), and thus present the highest resistance to the flows through them. However, based on this data, it was not possible to definitively state that $\mathrm{Re}_{d_l} \leq 0.1$ is the demarcation for the Darcy flow regime, as there were no data points in this regime for the M20-1 and ERG40 porous metal foams, and even for the M40-1 and M60-2 porous metal foams, there were very few data points in this regime. More data are required to confirm this finding, using an experimental apparatus that could accurately measure lower pressure drops and lower mass flow rates than those possible with the experimental apparatus used in this work.

## 4.5 Flows in Adjacent Open and Porous Domains

As was mentioned earlier, the test sections with the M20-1, M40-1, M60-2, and the ERG40 porous metal foams were used in the experimental runs undertaken for determining the coefficients in the interfacial stress-jump condition. For convenience, the Figure 2.1 and Eq. 2.11 are provided again below, in Figure 4.7 and Eq. 4.3, respectively.

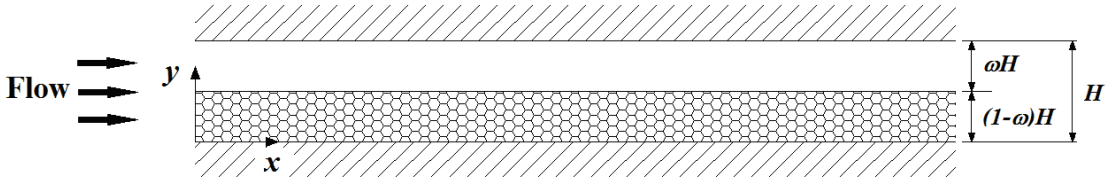


Figure 4.7: Schematic illustration of the problems of interest

$$\left[\frac{1}{\varepsilon}\left(\frac{du_*}{dy_*}\right)_{pd} - \left(\frac{du_*}{dy_*}\right)_{od}\right]^I = \left[\beta_1 \frac{1}{\sqrt{Da}} u_* + \beta_2 \,\mathrm{Re}\, u_*^2\right]^I \tag{4.3}$$

The various dimensionless variables that appear in this equation were defined and discussed in Sections 2.3 and 2.4, so they are not repeated here.

The following data were collected in the experiments on fully developed fluid flows in test sections with adjacent open and porous domains, and some of the data that corresponded to the laminar-flow regime were used for determining the coefficients in the interfacial stress-jump condition: the total mass flow rate of air flowing through the test section, $\dot{m}_{total}$; the absolute temperature, dynamic viscosity, and density of air within the test section, $T_{abs}$, $\mu$, and $\rho$, respectively; and axial variation of the time-averaged wall-static-pressure drop along the top wall and the instantaneous and time-averaged values of wall-shear-stress at one location on the top wall. The full sets of experimental data collected in these experiments could be useful in validating and refining mathematical models of transitional and turbulent flows in the problems of interest, and are a key contribution of this work; these data are concisely presented in Appendix C. These data, along with the analytical solution for laminar flows and related physical requirements (as presented in Section 2.4) were used to obtain the following results: open-domain interfacial shear stress; open- and porous-domain interfacial dimensionless velocity gradients (normal to the interface) for laminar flow; guidance for laminar-turbulent transition in the flows of interest; the coefficients in the interfacial tangential stress-jump condition; and the open-domain Darcy friction factor. These results are presented and discussed in the following subsections.

### 4.5.1 Open-Domain Interfacial Shear Stress

As was discussed in Section 2.4, the open-domain interfacial shear stress can be calculated using the following equation, obtained using a simple force balance on the open-domain side of the problem of interest, and the measured wall-shear-stress values on the surface of the top wall:

$$\tau_{od}^{I} = \left(-dp/dx\right)\omega H - \tau_{od}^{UW} \tag{4.4}$$

As was noted in Chapter 2, this equation applies to laminar flow and also turbulent flow (if the shear stresses and pressure gradient are interpreted as time-averaged quantities).

### 4.5.2 Open- and Porous-Domain Interfacial Dimensionless Velocity Gradients (Normal to the Interface) in Laminar Flow

The open-domain interfacial wall shear stress and the analytical solution to laminar flow in the problems of interest were used to determine the above-mentioned dimensionless velocity gradients, using Eq. 2.17, which is repeated below for convenience:

$$\begin{aligned} u_{*}^{I} &= [0.5\omega^{2} - \tau_{od}^{I}\omega / \{(-dp/dx)H\}] \\ (du_{*}/dy_{*})_{od}^{I} &= [0.5\omega - (u_{*}^{I}/\omega)] \\ (du_{*}/dy_{*})_{pd}^{I} &= -\frac{4(u_{\infty *} + u_{1*})}{(1+C)^{3}}(1-C)CB \end{aligned} \tag{4.5}$$

The various dimensional and dimensionless variables that appear in these equations were defined and discussed in Section 2.4, so they are not repeated here. As was noted above, the solution given in Eq. 4.5 applies only to laminar flows. Thus, when using this solution, it is necessary to determine which data points obtained in the related experiments pertain to the laminar-flow regime. Guidance for this determination required special considerations, which are discussed in the next subsection.

### 4.5.3 Guidance for Determining Laminar-Turbulent Transition

Guidance for determining laminar-turbulent transition in the problems of interest was obtained using several indicators. First, it must be realized that only two physically tenable shapes exist for the laminar-flow velocity profiles: in one, the interfacial velocity exceeds the superficial velocity within the porous domain; in the other, the interfacial velocity is less than the superficial velocity within the porous domain; and qualitative sketches of these two physically tenable shapes are given in the figure below.

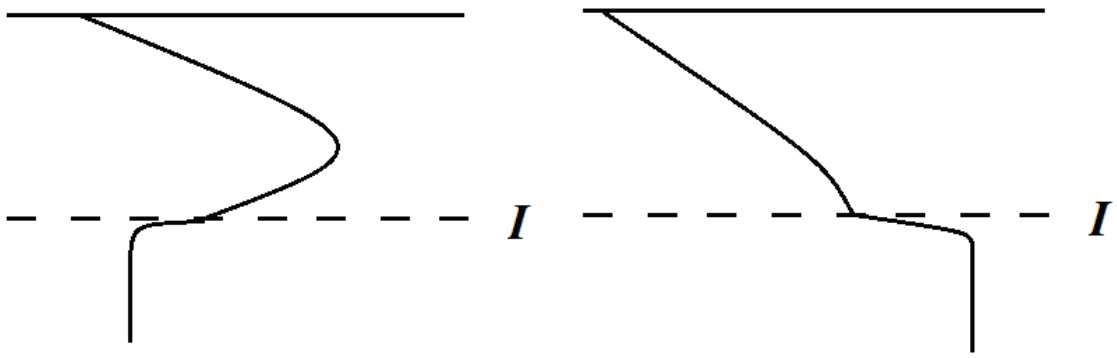


Figure 4.8: Two physically tenable shapes of the laminar-flow velocity profiles

From the two physically tenable shapes of the laminar-flow velocity profiles shown in Figure 4.8, it is possible to determine two indicators for laminar-turbulent transition. The first such indicator is based on the requirement that for laminar flows, the calculated open-domain interfacial shear stress cannot exceed the value of the shear stress measured at the top wall of the domain (otherwise, the analytical solution for laminar flows would require a negative value of the interfacial velocity, which is physically impossible in the problems of interest). The second indicator is based on the requirement that the open- and porous-domain velocity gradients normal to the interface must be of the same sign. Thus, for any set of experimental data, if the above-mentioned two requirements were not satisfied, then that would be a sufficient condition to deduce that the particular data set applies to turbulent flow at or in the vicinity of the interface. On the other hand, it should also be noted that the satisfaction of these requirements does not guarantee laminar flow.

Thus, additional indicators of laminar-turbulent transition were needed. One other such indicator is a plot of the power spectral density (PSD) of the instantaneous wall-shear-stress measurements taken at the top wall versus the frequency of its fluctuations. Such a graphical representation of the PSD is indicative of the magnitude of the fluctuations of the instantaneous wall shear stress at various frequencies. In this context, it should be noted that no fluctuations (for all practical purposes) in the measured wall-shear-stress on the top wall of the domain (see Figure 4.7) is indicative of laminar flow. Two plots of the PSD of the instantaneous shear stress on the top wall of the domain are presented in Figure 4.9.

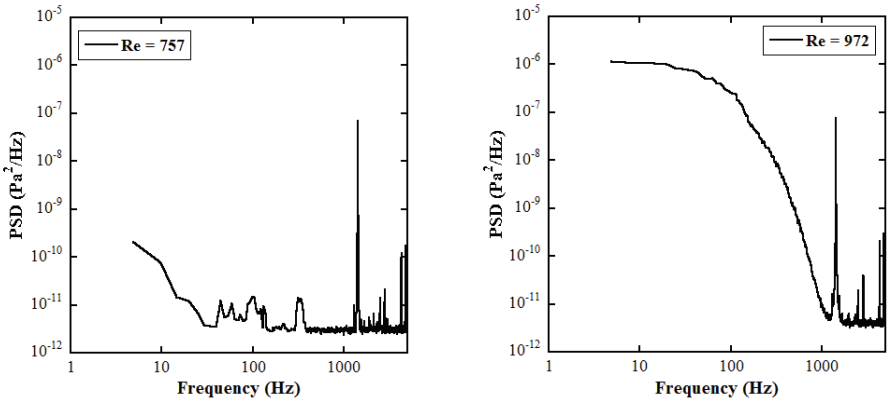


Figure 4.9: Plots of power spectral density (PSD) of the instantaneous shear stress on the top wall for laminar flow (left) and turbulent flow (right)

The plot on the left of Figure 4.9 is indicative of laminar flows as the PSD spectrum is essentially flat, and the magnitude of the PSDs are of the order of effectively white electronic noise contained in the sensor signal (except for slightly larger values found at lower frequencies). The plot on the right of Figure 4.9 is indicative of turbulent flows as it contains PSD values orders of magnitude greater than the laminar-flow PSD values, continuously distributed over a broad range of frequencies. As can be seen in both these plots, a spike occurs at a frequency of approximately 1500-2000 Hz: this spike is not indicative of any physical fluctuations in the instantaneous wall shear stress, as it is present in both plots; rather, it is a feature of the signal from the wall-shear-stress sensor (unexplained at the moment), which could be filtered out, if desired.

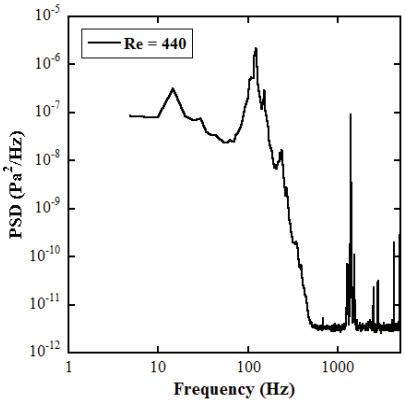


Figure 4.10: Plot of power spectral density of the instantaneous shear stress on the top wall for flow in the transitional regime

A plot of PSD for flow in the transitional regime is presented in Figure 4.10: it contains distinct peaks at intermediate frequencies, and the magnitudes of the PSDs are larger than those for laminar flow but not as high as those for turbulent flow; both these features are indicative of flow in the transitional regime. Plots of PSD of the last set of experimental data that falls in the laminar regime and the first set of such data that indicates flow in the transitional regime were obtained for each of the test-section configurations considered.

In this context, it should be noted that the PSD plots obtained in this work cannot be used to definitively deduce that the open-domain flow is laminar in the vicinity of the interface in the problems of interest. This uncertainty arises because the experimental shear-stress data used for these PSD plots pertain to the top wall, and the possibility exists that the open-domain flow is laminar in the vicinity of the top wall but it is in the turbulent or transitional regimes in the vicinity of the interface between the porous and open domains.

Thus, the aforementioned three indicators cannot be used to definitively conclude that the flow in the vicinity of the interface is laminar. No additional indicators could be gleaned from the experimental data obtained in this work. Nevertheless, the above-mentioned three indicators do provide useful (but not definitive) guidance regarding laminar-turbulent transition. They were used in this work to determine the following: 1) the suitability of experimental data for use in determining the coefficients in the interfacial stress-jump condition; and 2) the upper-limit values of the open-domain Reynolds number, $\mathrm{Re}_{od}^{D_h}$, for existence of laminar flow.

### 4.5.4 Upper-Limit Values of Open-Domain Reynolds Number for Existence of Laminar Flow

As was discussed in the previous subsection, the above-mentioned three indicators were used to deduce upper-limit values of the open-domain Reynolds number, $\mathrm{Re}_{od}^{D_h}$, for existence of laminar flow. With reference to the aforementioned PSD plots, these upper-limit values of $\mathrm{Re}_{od}^{D_h}$ were taken as those pertaining to the last set of experimental data

that falls in the laminar regime. These values of $\mathrm{Re}_{od}^{D_h}$ for the M20-1, M40-1, M60-1, ERG40-1, and ERG40-2 experimental runs are presented below in Table 4.7.

| $(\mathrm{Re}_{od})^{Dh}$ Transition | M20-1 | M40-1 | M60-2 | ERG40-1 | ERG40-2 |
|---|---|---|---|---|---|
| **1/8" Open-Domain Height** | 304 | 88 | 306 | 240 | 242 |
| **1/4" Open-Domain Height** | --- | 516 | 1529 | 498 | 498 |
| **1/2" Open-Domain Height** | --- | 2139 | 2416 | --- | --- |

Table 4.7: Upper-limit values of open-domain Reynolds number for laminar flow

The cells in Table 4.7 with dashed lines (---) indicate that no data could be collected in the laminar regime for the corresponding metal-foam/open-domain combination. The results in this table show the following: the upper-limit value of $\mathrm{Re}_{od}^{D_h}$ for the existence of laminar flow for the nominal 1/8" open-domain height configuration is of the order of 300 (for M20-1) or lower; increasing the open-domain height to nominal 1/4", increases this value of $\mathrm{Re}_{od}^{D_h}$, to about 1500 (for M60-2); and increasing the open-domain height to nominal 1/2", further increases this value of $\mathrm{Re}_{od}^{D_h}$ to about 2400 (for M60-2). This increase in the upper-limit value of $\mathrm{Re}_{od}^{D_h}$ for laminar flow with an increase in the open-domain height can be explained by examining the apparent surface roughness the metal foam presents at the interface between the porous and open domains. As the open-domain height is increased, the ratio of this surface roughness to the open-domain height (relative roughness) decreases. Therefore, as the open-domain height is increased, the effect this roughness has on the flow within the open domain is lowered, and the upper-limit value of $\mathrm{Re}_{od}^{D_h}$ is higher. Further evidence of this effect can be found in plots of the open-domain Darcy friction factor versus $\mathrm{Re}_{od}^{D_h}$ presented in the Subsection 4.5.6. It should also be noted that the repeatability runs undertaken for the ERG40 foam (ERG40-1 and ERG40-2), produced remarkably similar upper-limit values of $\mathrm{Re}_{od}^{D_h}$ (see Table 4.7).

### 4.5.5 Determination of the Interfacial Stress-Jump Coefficients

Using the above-mentioned indicators and guidance for laminar-turbulent transition in the problems of interest, experimental data points that were most likely to fall in the laminar-

flow regime were used to determine the two coefficients, $\beta_1$ and $\beta_2$, in the interfacial tangential stress-jump condition (see Eqs. 4.3). First, these experimental data points in the laminar-flow regime and the corresponding analytical solution to the problems of interest (see Eq. 4.5) were used to calculate the corresponding values of the open- and porous-domain interfacial dimensionless velocity gradients (normal to the interface). These velocity gradients were then used in the following form of the dimensionless interfacial tangential stress-jump condition (see Eq. 4.6 below), along with a least-squares linear-curve-fit, to calculate values of $\beta_1$ and $\beta_2$ for each of the chosen experimental runs, M20-1, M40-1, M60-2, and a combination of ERG40-1 and ERG40-2 (denoted in this context as simply ERG40. Plots of $Y_{interface}$ versus $X_{interface}$ for M20-1 and M40-1 are given in Figure 4.11 (calculated values using suitable experimental data points); and these plots for M60-2 and ERG40-1 are given in Figure 4.12.

$$
\begin{aligned}
Y_{interface} &= \left[\frac{1}{\varepsilon}\left(\frac{du_*}{dy_*}\right)^I_{pd} - \left(\frac{du_*}{dy_*}\right)^I_{od}\right] \Bigg/ \left[\frac{1}{\sqrt{Da}}u_*^I\right] \\
X_{interface} &= \left[\mathrm{Re}\left(u_*^I\right)^2\right] \Bigg/ \left[\frac{1}{\sqrt{Da}}u_*^I\right] \\
Y_{interface} &= \beta_1 + X_{interface}\beta_2
\end{aligned}
\tag{4.6}
$$

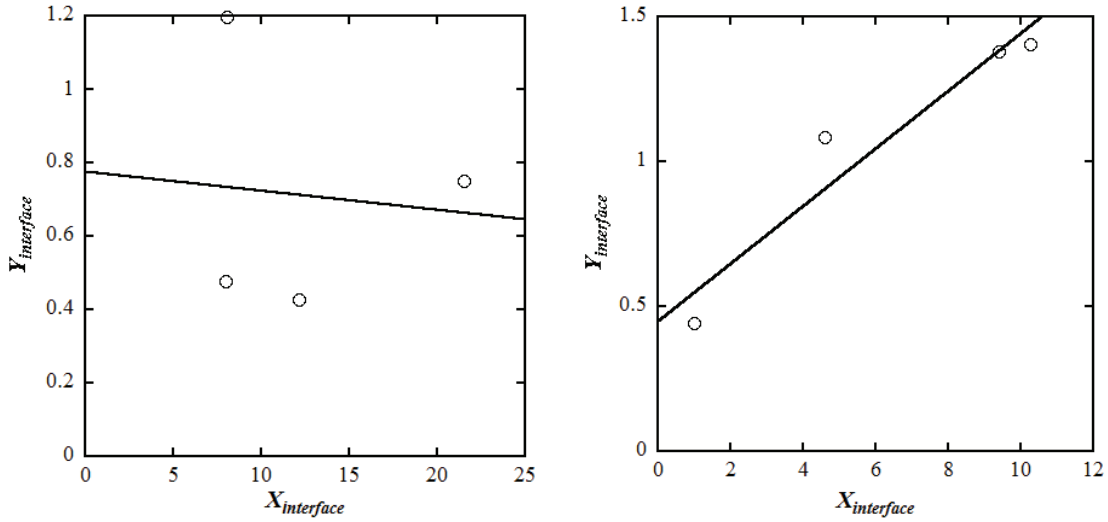


Figure 4.11: $Y_{interface}$ versus $X_{interface}$ plots for M20-1 (left) and M40-1 (right)

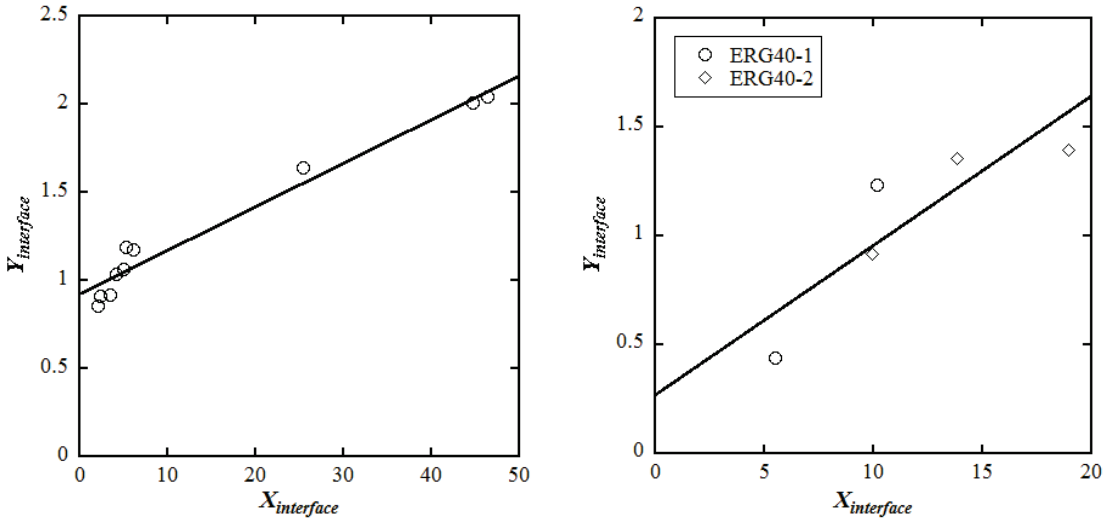


Figure 4.12: $Y_{interface}$ versus $X_{interface}$ plots for M60-2 (left) and ERG40 (right)

Very few data points could be obtained in the laminar-flow regime for M20-1, M40-1, and ERG40 metal foams (as was stated above, the data points from the experimental runs ERG40-1 and ERG40-2 were combined to obtain a more reliable least-squares liner-curve-fit). The paucity of data points in the laminar-flow regime for the M20-1 run makes the resulting $Y_{interface}$ versus $X_{interface}$ plot unreliable, so it does not yield satisfactory values of $\beta_1$ and $\beta_2$. Fairly reliable values of $\beta_1$ and $\beta_2$ could be obtained for the M40-1 and M60-2 metal foams. The values of $\beta_1$ and $\beta_2$, and the coefficient of determination ($R^2$) of the corresponding least-squares linear-curve-fits, are summarized below in the Table 4.8. All experimental data obtained for the flows in adjacent open and porous domains are presented in Appendix C.

| | M20-1 | M40-1 | M60-2 | ERG40 |
|---|---|---|---|---|
| $\beta_1$ | 0.7772 | 0.4506 | 0.9225 | 0.2654 |
| $\beta_2$ | -0.00523 | 0.09914 | 0.02482 | 0.06871 |
| $R^2$ | 0.009 | 0.9230 | 0.9649 | 0.7464 |

Table 4.8: Values of the coefficients in the interfacial stress-jump condition

### 4.5.6 Open-Domain Friction Factors

The plots of the open-domain Darcy friction factor ( $f_{D-od}$ ) versus the open-domain Reynolds number ( $\mathrm{Re}_{od}^{D_h}$ ) are presented in Figure 4.13 for the M60-2 foam (these data are presented in tabular forms in Appendix C, for each of the foams considered in this work). The results in Figure 4.13 display the following features: 1) for all three open-domain heights, there are transition- and turbulent-flow regimes; 2) for the nominal 1/8" and 1/4" open-domain heights, there is a clear laminar-to-turbulent transition regime; and 3) as the open-domain height is increased, the value of open-domain Darcy friction factor decreases for the same value of open-domain Reynolds number, which demonstrates the diminishing effect of the apparent surface roughness that the metal-foam presents at the interface. The experiments conducted with the other metal foams yielded similar results, except that the plots for the three different open-domain heights for each of these foams were somewhat closer together than those for the M60-2 foam shown in Figure 4.13.

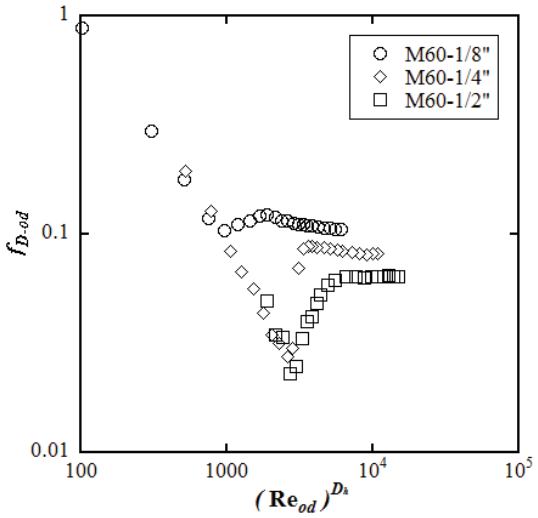


Figure 4.13: Open-domain Darcy friction factor values for the M60-2 porous metal foam

This subsection concludes the presentation of the results obtained in this work. In the following chapter, the thesis and the contributions of this work are reviewed, and some ideas for potential extensions of this work are put forward.

# Chapter 5 – Conclusion

This final chapter contains a review of the thesis, a summary of the contributions of this work, and some recommendations for extensions of this work.

## 4.1 Review of the Thesis

In Chapter 1, the motivation for this work, its overall goals and specific objectives, a review of the relevant literature, and the organization of the thesis were presented. Central to the literature review were discussions of the permeability and dimensionless form-drag coefficient of porous media, and fluid flows in adjacent open and porous domains. The practices of using empirical correlations and experimental data for determining the permeability and dimensionless form-drag coefficient were comparatively discussed, and their advantages, difficulties, and shortcomings were highlighted. Various approaches to modeling fluid flows in adjacent open and porous domains were presented. It was discussed in this context that if the most practical of these approaches (the macroscopic-scale approach) is used along with the assumption of uniform porosity and permeability throughout the porous medium, all the way to the interface between the open and porous domains, then an interfacial condition is needed to account for an apparent jump in the shear (tangential) stress. This interfacial condition contains two dimensionless coefficients, of order unity or less. It was also highlighted that experimental inputs are critically important and urgently needed for the determination of the aforementioned two dimensionless coefficients in the interfacial tangential stress-jump condition.

The theoretical considerations used in this work for designing the experimental set-ups and procedures, selecting and implementing related instrumentation, and processing the experimental data collected were presented and concisely discussed in Chapter 2. The assumptions invoked and the mathematical models of the problems of interest were presented. The emphasis was on a macroscopic approach to the mathematical modeling of Newtonian fluid flows in adjacent open and porous domains: the fluid flow in the open domain was modeled using the continuity and Navier-Stokes equations; the volume-averaged forms of the continuity equation and the momentum equation (Darcy-Brinkman-

Forchheimer equation) were used to model the fluid flow in the porous domain; the no-slip and impermeability conditions were imposed at solid boundaries; the velocity (superficial velocity in the porous domain), pressure (intrinsic-phase-average pressure in the porous domain), and normal stresses were assumed to be continuous at the interface between the open and porous domains; and the apparent jump in the shear stress at this interface was handled using a condition which involved two dimensionless coefficients. An analytical solution for laminar, fully developed, constant-property Newtonian fluid flow in the problem of interest was adapted from the works of Kuznetsov (1999) and Costa et al. (2008). Four different approaches for processing the data obtained from experiments for determining the permeability and dimensionless form-drag coefficient for the porous metal foam used in this work were presented, with special emphasis on their pros and cons. Use of the aforementioned analytical solution and experimental data (for laminar flows) for the determination of the two coefficients in the interfacial tangential stress-jump condition was also discussed. Finally, the definitions of several friction factors were presented along with related analytical solutions (when possible) or empirical correlations (if available) for laminar and turbulent flows in straight rectangular ducts with no porous medium (entirely open or unobstructed), completely filled with porous metal foam, and containing adjacent open and porous-metal-foam domains.

The porous metal foams and the experimental apparatus used in this work (a straight rectangular air channel, flow-measurement devices, and related instrumentation) were described in Chapter 3. The air channel was specially designed and constructed to conveniently allow experiments in which the test section had no porous medium within it (entirely open), was fully filled with the porous metal foams, and contained adjacent open and porous-metal-foam domains, with three different open-domain heights. The top wall of the test section was designed to incorporate 64 wall-static-pressure taps (for the measurement of time-averaged wall-static-pressure distributions) and also a wall-shear-stress sensor (for measurements of instantaneous and time-averaged wall-shear-stress) flush-mounted within a cylindrical Delrin insert. The wall-shear-stress sensor was specially constructed, calibrated, and used in this work: it is a redesigned version (incorporating several improvements) of a sensor designed and used earlier by Afara

(2012). Two flow-measurement devices were incorporated into the experimental facility: a Venturi tube that was specially designed, constructed, and calibrated for this work; and a bank of laminar flow elements, which the author had designed constructed in an earlier project, and were benchmarked used in Afara (2012).

The results obtained from the various experiments undertaken for benchmarking tasks, characterizing the porous metal foams (photomicrographs; measurements of the ligament, pore, and cell effective diameters; and porosity), determining the permeability and dimensionless form-drag coefficient for the porous metal foams, and determining the two dimensionless coefficients in the interfacial stress-jump condition were presented and discussed in Chapter 4, along with the related uncertainties, when applicable. With regard to the permeability and dimensionless form-drag coefficient, the results obtained using four different approaches to processing of the pertinent experimental data (labeled Approach 1-4; see discussions in Chapter 2) were presented and comparatively discussed in Chapter 4; checks of these results against corresponding measurements of time-averaged wall-static-pressure distributions showed that Approach 3 provided the most reliable and consistent results, with the proposed experimental facilities.

The full sets of data obtained from the experiments on airflows in test sections with adjacent open and porous domains (air temperature and atmospheric pressure within the test section; mass flow rates; wall-static-pressure distributions; and instantaneous and time-averaged wall-shear-stress measurements) in laminar, transitional, and turbulent regimes are presented in Appendix C. It was shown that a force balance equation can be used to obtain values of the open-domain interfacial shear stress from the measured values of the shear stress at the top-wall and the overall axial pressure gradient, for both laminar and turbulent flows in the open domain (time-averaged data must be used for cases involving turbulent flow). The aforementioned comprehensive sets of data, the analytical solution to the problem of fully developed laminar flow in adjacent open and porous domains, power-spectral-density (PSD) plots of the instantaneous wall-shear-stress measurements, and the requirements for physically tenable values for the laminar-flow results were used together to obtain guidance regarding laminar-turbulent transition,

and the corresponding results were presented in Chapter 4. The data collected in the experiments undertaken for determining the permeability and dimensionless form-drag coefficients for the porous metal foams were also used to prepare log-log plots of the a Darcy friction factor as a function of a Reynolds number (both based on the superficial velocity of the air and the ligament effective diameter of the metal foam) in the fully developed regime. Finally, the data collected in the experiments on flows in test sections with adjacent open and porous domains were also used to obtain the open-domain Darcy friction factor as a function of the corresponding Reynolds number. These friction-factor results were also presented and discussed in Chapter 4.

## 4.2 Contributions of the Thesis

The main contributions of this work are summarized below:

1. The design and construction of the straight rectangular air tunnel facility and the Venturi flow meter described in Chapter 3; and also the selection, implementation, calibration, and benchmarking of the related instrumentation.

2. The design and construction of an improved version of a wall-shear-stress sensor proposed earlier by Afara (2012), as described in Chapter 3. Another contribution in this regard was in the calibration of this sensor: it was discovered that it is more reliable and consistent to cast the related data in the form of ( $E^2 / R_{op}$ ) against $\overline{\tau}_w$, rather than $E^2$ against $\overline{\tau}_w$, as the former produces significantly less scatter of the data over many calibration runs; and the reasons behind this finding were described (in Chapter 3). In this context, it should be noted that $E^2$ against $\overline{\tau}_w$ was used initially in this work, as it is more in line with practices used in traditional in hot-wire anemometry Brunn (1996), and it was also the practice adopted in Afara (2012) and Afara et al. (2013).

3. A comparative assessment of four different approaches (Approach 1-4; as described in Chapter 2) to the processing of experimental data for determining the permeability and dimensionless form-drag coefficient for porous metal foams, and the reasons for the selection of Approach 3 for use in this work, as described in Chapter 4.

4. All of the experimental data presented in Appendices A-C.

5. All of the results and discussions presented in Chapter 4, and summarized in the previous section of this chapter.

## 4.3 Recommendations for Extensions of this Work

Some recommendations for extending this work are summarized below:

1. Visualization of the flow in the vicinity of the interface between the open and porous-metal domains could be used as an additional indicator of laminar-turbulent transition. Such flow visualization would require the use of clear Plexiglas (rather than aluminum) for the construction of the sidewalls and the wall-static-pressure-tap plate.

2. With relatively minor modifications of the porous-metal-foam test-section c-channels used in this work, experiments involving heat transfer could be undertaken.

3. Approach 4 may be the best of the four approaches discussed in this thesis for processing the data for determining the permeability and dimensionless form-drag coefficient of porous metal foams. However, the effective use of Approach 4 would require the incorporation of LFEs with smaller tubes and a differential-pressure transducer capable of accurately measuring values of 10 Pa or lower (and the related calibration capabilities). It would be worthwhile to undertake such enhancements.

4. The data collected during the experimental runs undertaken for determining the coefficients in the interfacial tangential stress-jump condition spanned the laminar, transitional, and turbulent fluid flow regimes. This data could be used to test and refine mathematical models and numerical methods for predictions of such fluid flows.

5. The design, construction, and optimization of thermal engineering devices incorporating porous metal foams, for example, ultra-compact heat exchangers and enhanced thermal energy storage units, would be worthwhile extensions of this work.

In conclusion, the author hopes that the discussions, results, and findings presented in this thesis will be useful to other researchers working on fluid flows in adjacent open and porous domains, and also serve as a motivation and provide a good foundation for the above-mentioned extensions of this work.

# References


Afara, S. (2012). *Development and testing of a wall-shear-stress sensor for measurements within notebook computers* (Master's Thesis). McGill University, Montréal, Canada.

Afara, S., Medvescek, J., Mydlarski, L., Baliga, B.R., & MacDonald, M. (2013) Development of a wall-shear-stress sensor and measurements in mini-channels with blockages. *8th World Conference on Experimental Heat Transfer, Fluid Mechanics, and Thermodynamics*. Lisbon, Portugal, June 16-20.

Alazmi, B., & Vafai, K. (2001). Analysis of fluid flow and heat transfer interfacial conditions between a porous medium and a fluid layer. *International Journal of Heat and Mass Transfer*, *44*(9), 1735-1749.

Albanakis, C., Missirlis, D., Michailidis, N., Yakinthos, K., Goulas, A., Omar, H., Tsipas, D., & Granier, B. (2009). Experimental analysis of the pressure drop and heat transfer through metal foams used as volumetric receivers under concentrated solar radiation. *Experimental Thermal and Fluid Science*, *33*(2), 246-252.

Antohe, B.V., Lage, J.L., Price, D.C., & Weber, R.M. (1997). Experimental determination of permeability and inertia coefficients of mechanically compressed aluminum porous matrices. *ASME Journal of Fluids Engineering, 119*(2)*,* 404-412.

Arthur, J.K., Ruth, D.W., & Tachie, M.F. (2009). PIV measurements of flow through a model porous medium with varying boundary conditions. *Journal of Fluid Mechanics*, *629*(1), 343-374.

Ashby, M.F., Evans, T., Fleck, N.A., Hutchinson, J.W., Wadley, H.N.G., & Gibson, L.J. (2000). *Metal foams: a design guide*. Butterworth-Heinemann.

Batchelor, G.K. (1967). *An introduction to fluid mechanics*. Cambridge University Press.

Beavers, G.S., & Joseph, D.D. (1967). Boundary conditions at a naturally permeable wall. *Journal of Fluid Mechanics*, *30*(1), 197-207.

Beavers, G.S., Sparrow, E.M. (1969). Non-Darcy flow through fibrous porous media. *ASME Journal of Applied Mechanics, 36*(4), 711-714.

Beavers, G.S., Sparrow, E.M., & Magnuson, R.A. (1970). Experiments on coupled parallel flows in a channel and a bounding porous medium. *Journal of Basic Engineering*, *92*(4), 843-848.

Beavers, G.S., Sparrow, E.M., & Rodenz, D.E. (1973). Influence of bed size on the flow characteristics and porosity of randomly packed beds of spheres. *ASME Journal of Applied Mechanics, 40*(3), 655-660.

Bhattacharya, A., Calmidi, V.V., & Mahajan, R.L. (2002). Thermophysical properties of high porosity metal foams. *International Journal of Heat and Mass Transfer*, *45*(5), 1017-1031.

Biasetto, L., Colombo, P., Innocentini, M.D.M., & Mullens, S. (2007). Gas permeability of microcellular ceramic foams. *Industrial and Engineering Chemistry Research, 46*(10), 3366-3372.

Bonnet, J.-P., Topin, F., & Tadrist, L. (2008). Flow laws in metal foams: compressibility and pore size effects. *Transport in Porous Media, 73*(2), 233-254.

Boosma, K., & Poulikakos, D. (2002). The effects of compression and pore size variations on the liquid flow characteristics in metal foams. *AMSE Journal of Fluids Engineering, 124*(1), 263-272.

Boosma, K., Poulikakos, D., & Zwick, F. (2003). Metal foams as compact high performance heat exchangers. *Mechanics of Materials, 35*(12), 1161-1176.

Breugem, W.P., Boersma, B.J., & Uittenbogaard, R.E. (2006). The influence of wall permeability on turbulent channel flow. *Journal of Fluid Mechanics*, *562*(1), 35-72.

Brinkman, H.C. (1949). A calculation of the viscous force exerted by a flowing fluid on a dense swarm of particles. *Applied Scientific Research*, *1*(1), 27-34.

Bruun, H.H. (1996). *Hot wire anemometry: principles and signal analysis*. Oxford University Press.

Calmidi, V.V. (1998). *Transport phenomenon in high porosity metal foams* (Ph.D. Thesis). University of Colorado, Colorado, USA.

Carotenuto, C., Marinello, F., & Minale, M. (2012). A new experimental technique to study the flow in a porous layer via rheological tests. *AIP Conference Proceedings, 1453*(1), 29-34.

Chan, H. C., Huang, W. C., Leu, J. M., & Lai, C. J. (2007). Macroscopic modeling of turbulent flow over a porous medium. *International Journal of Heat and Fluid Flow*, *28*(5), 1157-1166.

Chandesris, M., & Jamet, D. (2006). Boundary conditions at a planar fluid–porous interface for a Poiseuille flow. *International Journal of Heat and Mass Transfer*, *49*(13), 2137-2150.

Chandesris, M., & Jamet, D. (2007). Boundary conditions at a fluid–porous interface: an a priori estimation of the stress jump coefficients. *International journal of heat and mass transfer*, *50*(17), 3422-3436.

Chandesris, M., & Jamet, D. (2009). Jump conditions and surface-excess quantities at a fluid/porous interface: a multi-scale approach. *Transport in porous media*, *78*(3), 419-438.

Coleman, S. E., Nikora, V. I., McLean, S. R., & Schlicke, E. (2007). Spatially averaged turbulent flow over square ribs. *Journal of Engineering Mechanics*, *133*(2), 194-204.

Costa, V.A.F., Oliveira, L.A., & Baliga, B.R. (2008). Implementation of the Stress Jump Condition in a Control-Volume Finite-Element Method for the Simulation of Laminar Coupled Flows in Adjacent Open and Porous Domains. *Numerical Heat Transfer, Part B: Fundamentals*, *53*(5), 383-411.

Crosnier, S., du Plessis, J.P., Riva, R., & Legrand, J. (2006). Modeling of gas flow through isotropic metallic foams. *Journal of Porous Media*, *9*(1), 35-54.

Darcy, H.P.G. (1856). *Les fontaines publiques de la ville de Dijon*.

de Lemos, M.J., & Silva, R. A. (2006). Turbulent flow over a layer of a highly permeable medium simulated with a diffusion-jump model for the interface. *International Journal of Heat and Mass Transfer*, *49*(3), 546-556.

de Lemos, M.J. (2012). *Turbulence in porous media: modeling and applications*. Elsevier.

Deng, C., & Martinez, D.M. (2005). Viscous flow in a channel partially filled with a porous medium and with wall suction. *Chemical Engineering Science*, *60*(2), 329-336.

Despois, J.-F., & Mortensen, A. (2005). Permeability of open-pore microcellular materials. *Acta Meterialia, 53*(5), 1381-1388.

Dimitris, S., & Panayotis, P. (2010). Macroscopic turbulence models and their application in turbulent vegetated flows. *Journal of Hydraulic Engineering*, *137*(3), 315-332.

Dukhan, N. (2006). Correlations for the pressure drop for flow through metal foam. *Experiments in Fluids, 41*(4), 665-672.

Dukhan, N., & Minjeur II, C.A. (2011). A two-permeability approach for assessing flow properties in metal foam. *Journal of Porous Materials, 18*(4), 417-424.

Dukhan, N., & Patel, K. (2011). Effect of sample's length on flow properties of open-cell metal foam and pressure-drop correlations. *Journal of Porous Materials, 18*(6), 655-665.

Dukhan, N., & Ali, M. (2012). Strong wall and transverse size effects on pressure drop of flow through open-cell metal foam. *International Journal of Thermal Sciences, 57*, 85-91.

Dullien, F.A.L. (1992). *Porous media: fluid transport and pore structure*. Academic Press.

du Plessis, J.P., Montillet, A., Comiti, J., & Legrand, J. (1994). Pressure drop prediction for flow through high porosity metallic foams. *Chemical Engineering Science*, *49*(21), 3545-3553.

Dupuit, A.J. (1863). Etude theoriques et pratiques sur les mouvements des eaux a travers les terrains permeables. *Carilian-Goeury, Paris*.

Edouard, D., Lacroix, M., Huu, C.P., & Luck, F. (2008). Pressure drop modeling on SOLID foam: State-of-the art correlation. *Chemical Engineering Journal*, *144*(2), 299-311.

Ergun, S. (1952). Fluid flow through packed columns. *Chemical Engineering Progress*, *48*(2), 89-94.

Finnigan, J. J., & Shaw, R. H. (2008). Double-averaging methodology and its application to turbulent flow in and above vegetation canopies. *Acta Geophysica*, *56*(3), 534-561.

Firdaouss, M., Guermond, J.L., & Le Quéré, P. (1997). Nonlinear corrections to Darcy's law at low Reynolds numbers. *Journal of Fluid Mechanics*, *343*, 331-350.

Forchheimer, P. (1901). Wasserbewegung durch boden. *Zeitschrift des Vereines Deutscher Ingenieure*, *45*, 1781-1788.

Fourie, J.G., & du Plessis, J.P. (2002). Pressure drop modelling in cellular metallic foams. *Chemical Engineering Science*, *57*(14), 2781-2789.

Fox, R.W., McDonald, A.T., & Pritchard, P.J. (2006). *Introduction to fluid mechanics*. John Wiley.

Givler, R.C., & Altobelli, S.A. (1994). A determination of the effective viscosity for the Brinkman-Forchheimer flow model. *Journal of Fluid Mechanics, 258*(1), 355-370.

Goyeau, B., Lhuillier, D., Gobin, D., & Velarde, M.G. (2003). Momentum transport at a fluid–porous interface. *International Journal of Heat and Mass Transfer*, *46*(21), 4071-4081.

Hazen, A. (1893). Some physical properties of sand and gravels with reference to their use in filtration. *Massachusetts State Board of Health, Twenty-fourth Annual Report, 34*, 539–556.

Higashino, M., & Stefan, H.G. (2012). Model of turbulence penetration into a suspension layer on a sediment bed and effect on vertical solute transfer. *Environmental Fluid Mechanics*, *12*(5), 451-469.

Hu, Z., Yu, B., Chen, Z., Li, T., & Liu, M. (2012). Numerical investigation on the urban heat island in an entire city with an urban porous media model. *Atmospheric Environment*, *47*, 509-518.

Innocentini, M.D.M., Antunes, W.L., Baumgartner, J.B., Seville, J.P.K., & Coury, J.R. (1999a). Permeability of ceramic membranes to gas flow. *Advanced Powder Technology: Materials Science Forum, 299-300*, 19-28.

Innocentini, M.D.M., Salvini, V.R., Pandolfelli, V.C., & Coury, J.R. (1999b). Assessment of Forchheimer's equation to predict the permeability of ceramic foams. *Journal of the American Ceramic Society, 82*(7), 1945-1948.

Innocentini, M.D.M., Salvini, V.R., Pandolfelli, V.C., & Coury, J.R. (1999c). The permeability of ceramic foams. *American Ceramic Society Bulletin, 78*(9), 78-84.

Innocentini, M.D.M., Lefebvre, L.P., Meloni, R.V., & Baril, E. (2010). Influence of sample thickness and measurement set-up on the experimental evaluation of permeability of metallic foams. *Journal of Porous Materials*, *17*(4), 491-499.

Jamet, D., & Chandesris, M. (2009). On the intrinsic nature of jump coefficients at the interface between a porous medium and a free fluid region. *International Journal of Heat and Mass Transfer*, *52*(1), 289-300.

Jamet, D., Chandesris, M., & Goyeau, B. (2009). On the equivalence of the discontinuous one-and two-domain approaches for the modeling of transport phenomena at a fluid/porous interface. *Transport in porous media*, *78*(3), 403-418.

Jin, L.W., Leong, K.C. (2008). Pressure drop and friction factor of steady and oscillating flows in open-cell porous media. *Transport in Porous Media*, *72*(1), 37-52.

Jones Jr., O.C. (1976). An Improvement in the Calculation of Turbulent Friction in Rectangular Ducts. *Journal of Fluids Engineering*, *98*(6), 173-180.

Joseph, D.D., Nield, D.A., & Papanicolaou, G. (1982). Nonlinear equation governing flow in a saturated porous medium. *Water Resources Research, 18*(4), 1049-1052.

Kaviany, M. (1995). *Principles of Heat Transfer in Porous Media*. Springer.

Kays, W.M., & London, A.L. (1984). *Compact heat exchangers*. McGraw-Hill.

Kell, G.S. (1975). Density, thermal expansivity, and compressibility of liquid water from 0. deg. to 150. deg.. Correlations and tables for atmospheric pressure and saturation reviewed and expressed on 1968 temperature scale. *Journal of Chemical and Engineering Data*, *20*(1), 97-105.

Kline, S.J., & McClintock, F.A. (1953). Describing uncertainties in single-sample experiments. *Mechanical engineering*, *75*(1), 3-8.

Krüger, E. (1918). Die Grundwasserbewegung. *Internationale Mitteilungen für Bodenkunde, 8*, 105.

Kubrak, E., Kubrak, J., & Rowinski, P. M. (2008). Vertical velocity distributions through and above submerged, flexible vegetation. *Hydrological sciences journal*, *53*(4), 905-920.

Kuznetsov, A.V. (1997). Influence of the stress jump condition at the porous-medium/clear-fluid interface on a flow at a porous wall. *International communications in heat and mass transfer*, *24*(3), 401-410.

Kuznetsov, A.V. (1999). Fluid mechanics and heat transfer in the interface region between a porous medium and a fluid layer: a boundary layer solution. *Journal of Porous Media*, *2*(3), 309-321.

Lacroix, M., Nguyen, P., Schweich, D., Pham Huu, C., Savin-Poncet, S., & Edouard, D. (2007). Pressure drop measurements and modeling on SiC foams. *Chemical engineering science*, *62*(12), 3259-3267.

Lage, J.L., Antohe, B.V., & Nield, D.A. (1997). Two types of nonlinear pressure-drop versus flow-rate relation observed for saturated porous media. *ASME Journal of Fluids Engineering, 119*(3), 700-706.

Lage, J.L. (1998). The fundamental theory of flow through permeable media from Darcy to turbulence. In Ingham, D.,B., and Pop, I. (Eds.), *Transport phenomena in porous media* (1-30). Pergamon.

Lage, J.L., & Antohe, B.V. (2000). Darcy's experiments and the deviation to nonlinear flow regime. *ASME Journal of Fluids Engineering, 122*(3), 619-625.

Lage, J.L., Krueger, P.S., & Narasimhan, A. (2005). Protocol for measuring permeability and form coefficient of porous media. *Physics of Fluids, 17*(8), 1-4.

Lefebvre, L.P., Banhart, J., & Dunand, D. (2008). Porous metals and metallic foams: current status and recent developments. *Advanced Engineering Materials*, *10*(9), 775-787.

Lu, T., Jiang, P.X., Guo, Z.J., Zhang, Y.W., & Li, H. (2010). Large-eddy simulations (LES) of temperature fluctuations in a mixing tee with/without a porous medium. *International Journal of Heat and Mass Transfer*, *53*(21), 4458-4466.

Ma, H., & Ruth, D.W. (1993). The microscopic analysis of high Forchheimer number flow in porous media. *Transport in Porous Media, 13*(2), 139-160.

Madani, B., Topin, F., Rigollet, F., & Tadrist, L. (2007). Flow laws in metallic foams: experimental determination of inertial and viscous contributions. *Journal of Porous Media, 10*(1), 51-70.

Mancin, S., Zilio, C., Cavallini, A., & Rossetto, L. (2010). Pressure drop during air flow in aluminum foams. *International Journal of Heat and Mass Transfer*, *53*(15), 3121-3130.

Maydanik, Y.F. (2005). Loop heat pipes. *Applied Thermal Engineering*, *25*(5), 635-657.

McLean, S.R., & Nikora, V.I. (2006). Characteristics of turbulent unidirectional flow over rough beds: Double-averaging perspective with particular focus on sand dunes and gravel beds. *Water resources research*, *42*(10).

Medraj, M., Baril, E., Loya, V., & Lefebvre, L.-P. (2007). The effect of microstructure on the permeability of metallic foams. *Journal of Materials Science, 42*(12), 4372-4383.

Mei, C.C., & Auriault, J.L. (1991). The effect of weak inertia on flow through a porous medium. *Journal of Fluid Mechanics*, *222*(1), 647-663.

Miwa, S., & Revankar, S.T. (2009). Hydrodynamic characterization of nickel metal foam, part 1: single-phase permeability. *Transport in porous media*, *80*(2), 269-279.

Moreira, E.A., Innocentini, M.D.M., & Coury, J.R. (2004). Permeability of ceramic foams to compressible and incompressible flow. *Journal of the European Ceramic Society, 24*(10-11), 3209-3218.

Muley, A., Kiser, C., Sundén, B., & Shah, R.K. (2012). Foam heat exchangers: A technology assessment. *Heat Transfer Engineering*, *33*(1), 42-51.

Nabovati, A., & Sousa, A.C.M. (2007). Fluid flow simulation in random porous media at pore level using the lattice Boltzmann method. *Journal of Engineering Science and Technology*, *2*(3), 226-237.

Nawaz, K., Bock, J., & Jacobi, A. (2012). Thermal-hydraulic performance of metal foam heat exchangers. *International Refrigeration and Air Conditioning Conference at Purdue*, West Lafayette, USA, July 16-19.

Neale, G., & Nader, W. (1974). Practical significance of Brinkman's extension of Darcy's law: coupled parallel flows within a channel and a bounding porous medium. *The Canadian Journal of Chemical Engineering*, *52*(4), 475-478.

Nield, D.A., & Bejan, A. (2013). *Convection in porous media*. Springer.

Ochoa-Tapia, J.A., & Whitaker, S. (1995a). Momentum transfer at the boundary between a porous medium and a homogeneous fluid—I. Theoretical development. *International Journal of Heat and Mass Transfer*, *38*(14), 2635-2646.

Ochoa-Tapia, J.A., & Whitaker, S. (1995b). Momentum transfer at the boundary between a porous medium and a homogeneous fluid—II. Comparison with experiment. *International Journal of Heat and Mass Transfer*, *38*(14), 2647-2655.

Ochoa-Tapia, J.A., & Whitaker, S. (1998). Momentum jump condition at the boundary between a porous medium and a homogeneous fluid: inertial effects. *Journal of Porous Media*, *1*(3), 201-218.

Onstad, A.J., Elkins, C.J., Medina, F., Wicker, R.B., & Eaton, J.K. (2011). Full-field measurements of flow through a scaled metal foam replica. *Experiments in Fluids*, *50*(6), 1571-1585.

Paek, J.W., Kang, B.H., Kim, S.Y., & Hyun, J.M. (2000). Effective thermal conductivity and permeability of aluminum foam materials. *International Journal of Thermophysics, 21*(2), 453-464.

Prinos, P., Sofialidis, D., & Keramaris, E. (2003). Turbulent flow over and within a porous bed. *Journal of Hydraulic Engineering*, *129*(9), 720-733.

Prony, R. (1804). *Recherches physico-mathématiques sur la théorie des eaux courantes*. Imprimerie Impériale.

Saito, M.B., & de Lemos, M.J. (2010). A macroscopic two-energy equation model for turbulent flow and heat transfer in highly porous media. *International Journal of Heat and Mass Transfer*, *53*(11), 2424-2433.

Shwartz, J., & Probstein, R.F. (1969). Experimental study of slurry separators for use in desalination. *Desalination*, *6*(2), 239-266.

Suga, K., Matsumura, Y., Ashitaka, Y., Tominaga, S., & Kaneda, M. (2010). Effects of wall permeability on turbulence. *International Journal of Heat and Fluid Flow*, *31*(6), 974-984.

Suga, K., Mori, M., & Kaneda, M. (2011). Vortex structure of turbulence over permeable walls. *International Journal of Heat and Fluid Flow*, *32*(3), 586-595.

Vafai, K., & Tien, C.L. (1981). Boundary and inertia effects on flow and heat transfer in porous media. *International Journal of Heat and Mass Transfer*, *24*(2), 195-203.

Vafai, K., & Kim, S.J. (1990). Fluid mechanics of the interface region between a porous medium and a fluid layer—an exact solution. *International Journal of Heat and Fluid Flow*, *11*(3), 254-256.

Valdés-Parada, F.J., Ochoa-Tapia, J.A., & Alvarez-Ramirez, J. (2007). Diffusive mass transport in the fluid–porous medium inter-region: Closure problem solution for the one-domain approach. *Chemical Engineering Science*, *62*(21), 6054-6068.

Valdés-Parada, F.J., Alvarez-Ramírez, J., Goyeau, B., & Ochoa-Tapia, J.A. (2009). Computation of jump coefficients for momentum transfer between a porous medium and a fluid using a closed generalized transfer equation. *Transport in porous media*, *78*(3), 439-457.

Ward, J.C. (1964). Turbulent flow in porous media. *ASCE Journal of the Hydraulics Division, 90*(HY5), 1-12.

Whitaker, S. (1999). *The Method of Volume Averaging*. Kluwer Academic Publishing.

White, F.M. (1991). *Viscous fluid flow*. McGraw-Hill.

Wodie, J.C., & Levy, T. (1991). Correction non linéaire de la loi de Darcy. *Comptes rendus de l'Académie des sciences. Série 2, Mécanique, Physique, Chimie, Sciences de l'univers, Sciences de la Terre*, *312*(3), 157-161.

Woudberg, S., & du Plessis, J.P. (2010). An adaptable analytical Ergun-type equation for high porosity spongelike porous media. *AIP Conference Proceedings, 1254*, 3-8.

Zanoun, E.S., Durst,F., & Nagib,H. (2003). Evaluating the law of the wall in two-dimensional fully developed turbulent channel flows. *Physics of Fluids*, *15*(10), 3079-3089.

Zeng, Z., & Grigg, R. (2006). A criterion for non-Darcy flow in porous media. *Transport in Porous Media, 63*(1), 57-69.

Zhao, C.Y., Kim, T., Lu, T.J., & Hodson, H.P. (2001). *Thermal transport phenomena in Porvair Metal foams and sintered beds* (Final Report). Micromechanics Centre & Whittle Lab, Department of Engineering, University of Cambridge, Cambridge, UK.

# Appendix A – Venturi-Tube Design and Calibration Details

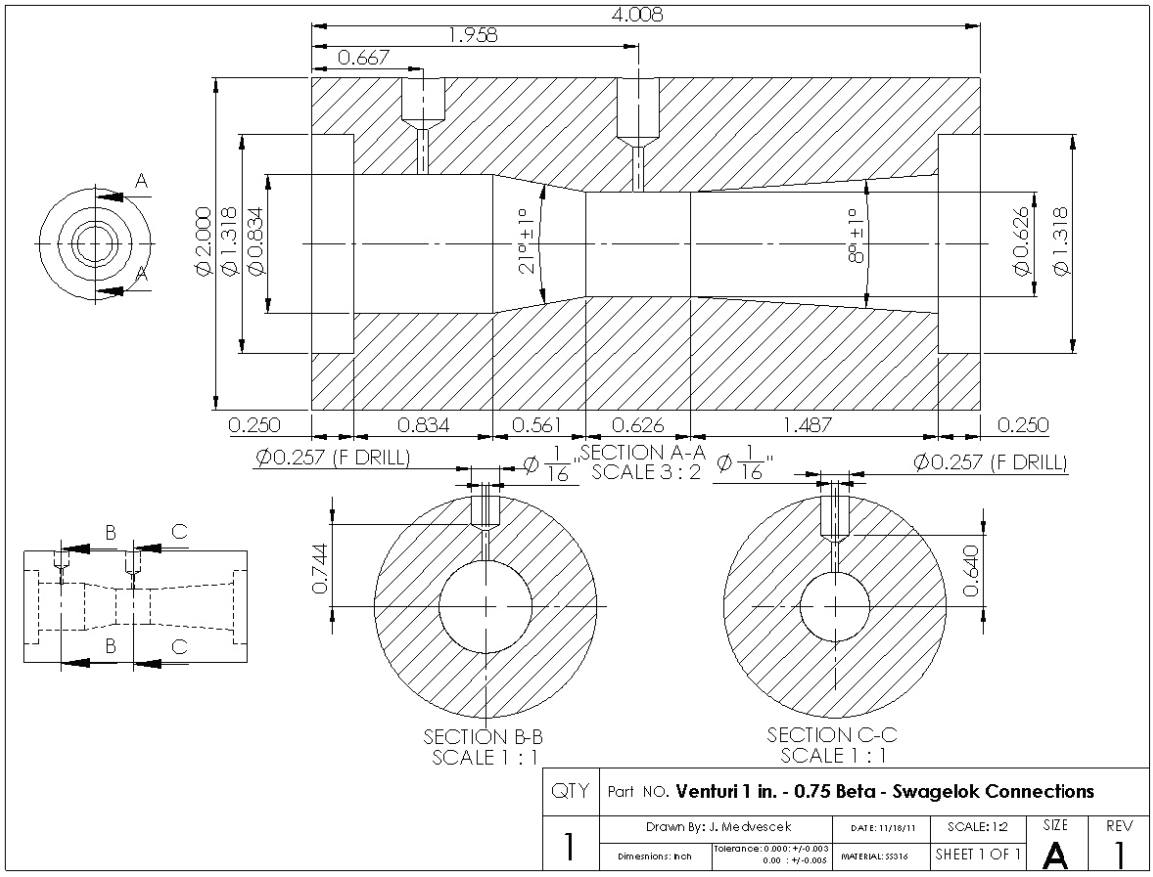


Figure A.1: CAD drawings and dimensions of the Venturi tube

The CAD drawings and dimensions of the Venturi tube are shown in Figure A.1. It was calibrated at Polycontrols Technologies Inc., a calibration-services laboratory located in Brossard, Québec, in accordance with procedures described in the Polycontrols Laboratory Quality Assurance Manual and conforming to ISO/IEC 17025-2005, ISO 9001-2008. This laboratory also states "the traceability for flow standard to the National Institute of Standards and Technology, NIST, is maintained by DH Instruments of Phoenix, Arizona and conform to ISO/IEC 17025, ANSI/NCSL Z540-1-1994, ISO-10012-1 and MIL-STD 45662A." The Calibration Laboratory Assessment Service (CLAS) of the National Research Council of Canada (NRC) certified the calibration capabilities of Polycontrols and the traceability of their standards to the International System of Units (SI) or those acceptable to the CLAS program. Details of the calibration procedure are provided in Subsection 3.5.1.2.

The range of calibration of the Venturi tube was chosen so as to utilize the full differential-pressure ranges of both the PX938 transducer and the PX838 transducer. The calibration data supplied by Polycontrols Technologies Inc. are presented in Table A.1: for each calibration point, they included the differential-pressure-transducer output voltage, $V_{measured}$; the absolute pressure, $p_1$, temperature, $T_1$, of the air at the upstream pressure tap of the Venturi tube; and the mass flow rate through the Venturi tube, $\dot{m}_{Venturi}$.

| $V_{measured}$ (V) | $p_1$ (in. $H_2O$) | $T_1$ (˚C) | $\dot{m}_{Venturi}$ (mg/s) | $V_{measured}$ (V) | $p_1$ (in. $H_2O$) | $T_1$ (˚C) | $\dot{m}_{Venturi}$ (mg/s) |
|---|---|---|---|---|---|---|---|
| **Omega PX938-0.4WD10V** | | | | **Omega PX838-40WD10V** | | | |
| -0.001 | | | 0 | 0.003 | | | 0 |
| 0.197 | 405.751 | 19.63 | 1581.64 | 0.896 | 406.222 | 20.03 | 10862.7 |
| 0.499 | 405.797 | 19.69 | 2533.55 | 1.006 | 406.727 | 18.75 | 11522.8 |
| 1.004 | 405.864 | 20.04 | 3610.80 | 2.009 | 407.268 | 19.58 | 16197.2 |
| 1.504 | 405.926 | 19.86 | 4454.50 | 3.028 | 409.281 | 19.05 | 19680.5 |
| 1.997 | 405.972 | 19.66 | 5152.40 | 3.996 | 409.900 | 17.96 | 22456.4 |
| 3.506 | 406.132 | 18.64 | 6885.30 | 5.019 | 410.910 | 18.02 | 24939.0 |
| 5.003 | 406.295 | 18.79 | 8248.70 | 6.011 | 411.832 | 18.04 | 27064.7 |
| 6.502 | 406.487 | 18.64 | 9351.30 | 6.987 | 412.744 | 18.10 | 28963.5 |
| 9.011 | 406.762 | 18.15 | 11032.0 | 7.982 | 413.637 | 18.39 | 30718.9 |
| 10.003 | 407.138 | 18.18 | 11628.7 | 8.999 | 415.615 | 18.81 | 32416.5 |
| | | | | 9.997 | 416.328 | 17.27 | 33898.8 |

Table A.1: Venturi-tube calibration data supplied by Polycontrols Technologies Inc.

Polycontrols Technologies Inc. measured all voltage outputs from the differential-pressure transducers using a Martel Voltage Calibrator Model MC-1200, absolute pressures with a DHI Molbox1, and temperatures with a Mist RTD Model M22. To increase the accuracy of the measured mass flow rates over the full range of calibration of the Venturi tube, they used four different sonic nozzle flow meters. All these sonic nozzles are referred to as Molblocs and were manufactured by DHI: Model 5E2-S was used for the lowest flow rate, up to 250 standard litres per minute (SLPM); model 1E3-S for flow rates up to 600 SLPM; model 2E3-2 for flow rates up to 1200 SLPM; and model 5E3-S for flow rates up to 3000 SLPM; and the stated experimental uncertainty is ±0.2% of reading for flow rates between 30 SLPM and 3000 SLPM. As the Venturi-tube calibration falls within the aforementioned range, the associated accuracy was taken to be ±0.2% of reading.

The zero-output voltage reading of each differential-pressure transducer, at zero mass flow rate through the Venturi tube, was subtracted from the output-voltage reading for each calibration point. The compensated output voltages were then converted to differential-pressure readings using the appropriate pressure transducer calibration curve. The upstream-tap absolute pressure was converted to Pascals using a conversion factor of 0.004021732 inch-$H_20$_20ºC/Pa, as the DHI Molbox1 absolute pressure transducer was calibrated in terms of inch-$H_20$_20 ºC. Using the upstream-tap pressure and temperature values, the density of the air could be obtained. All of the remaining parameters in Eq. 3.3 could then be calculated from the calibration data: their values are summarized in Table A.2 below (in order of ascending values of $\Delta p$), including the associated discharge coefficient, $C$, calculated by taking the calibration mass flow rate and dividing it by the theoretical mass flow rate (obtained using $C$ = 1 in Eq. 3.3). The last column in this table is the Reynolds number at the upstream-tap location; this data was included to confirm that the flow was indeed turbulent within the entrance tube.

| $\Delta p$ (Pa) | $p_1$ (kPa) | $\zeta$ ($p_2/p_1$) | $\rho_1$ (kg/m$^3$) | $\eta$ | $C$ | $Re_d$ | $Re_D$ |
|---|---|---|---|---|---|---|---|
| 19.63 | 100.89 | 0.9998 | 1.185 | 0.9998 | 0.9525 | 6958.6 | 5243.1 |
| 49.56 | 100.90 | 0.9995 | 1.185 | 0.9996 | 0.9604 | 11144.9 | 8397.4 |
| 99.62 | 100.92 | 0.9990 | 1.184 | 0.9991 | 0.9663 | 15868.8 | 11956.7 |
| 149.19 | 100.93 | 0.9985 | 1.185 | 0.9987 | 0.9742 | 19586.1 | 14757.6 |
| 198.06 | 100.94 | 0.9980 | 1.185 | 0.9983 | 0.9780 | 22666.7 | 17078.8 |
| 347.64 | 100.98 | 0.9966 | 1.190 | 0.9970 | 0.9859 | 30372.6 | 22884.9 |
| 496.03 | 101.02 | 0.9951 | 1.190 | 0.9957 | 0.9901 | 36372.3 | 27405.5 |
| 644.63 | 101.07 | 0.9936 | 1.191 | 0.9944 | 0.9854 | 41250.6 | 31081.3 |
| 875.84 | 101.01 | 0.9913 | 1.185 | 0.9924 | 0.9866 | 47740.9 | 35971.5 |
| 893.34 | 101.14 | 0.9912 | 1.194 | 0.9923 | 0.9885 | 48728.2 | 36715.4 |
| 983.72 | 101.13 | 0.9903 | 1.191 | 0.9915 | 0.9857 | 50814.7 | 38287.5 |
| 991.67 | 101.23 | 0.9902 | 1.195 | 0.9915 | 0.9893 | 51359.7 | 38698.2 |
| 1967.45 | 101.27 | 0.9806 | 1.190 | 0.9831 | 0.9889 | 71270.8 | 53700.7 |
| 2966.87 | 101.77 | 0.9708 | 1.198 | 0.9747 | 0.9835 | 86720.2 | 65341.4 |
| 3916.26 | 101.92 | 0.9616 | 1.204 | 0.9668 | 0.9822 | 99240.1 | 74774.8 |
| 4919.6 | 102.17 | 0.9518 | 1.207 | 0.9585 | 0.9806 | 110194.0 | 83028.0 |
| 5892.54 | 102.40 | 0.9425 | 1.209 | 0.9505 | 0.9794 | 119580.0 | 90100.1 |
| 6849.78 | 102.63 | 0.9333 | 1.212 | 0.9427 | 0.9792 | 127949.0 | 96405.9 |
| 7825.66 | 102.85 | 0.9239 | 1.213 | 0.9349 | 0.9792 | 135598.0 | 102170.0 |
| 8823.11 | 103.34 | 0.9146 | 1.217 | 0.9271 | 0.9797 | 142931.0 | 107695.0 |
| 9801.94 | 103.52 | 0.9053 | 1.226 | 0.9194 | 0.9767 | 150084.0 | 113084.0 |

Table A.2: Data used in calculation of the Venturi-tube discharge coefficient

As was described in Subsection 3.5.1.2, for each value of the measured differential pressure between the upstream and downstream pressure taps of the Venturi tube, $\Delta p$, and the related measured values of absolute pressure and temperature at the upstream pressure tap, $p_1$ and $T_1$, respectively, the values of $\eta$ and $\rho_1$ were obtained (using Eq. 3.4 and property data for air); and then an iterative procedure was used to obtain the corresponding mass flow rate, using Eqs. 3.3 to 3.6. Table A.3 summarizes the percent difference between the mass flow rates in the calibration data supplied by Polycontrols Technologies Inc. and the corresponding values calculated using the iterative method described in Section 3.5.1.2, for each calibration point.

| $\Delta p$ (Pa) | $\dot{m}_{calibration}$ (kg/s) | $\dot{m}_{method}$ (kg/s) | Difference (%) |
|---|---|---|---|
| 19.63 | 1.58E-03 | 1.58E-03 | 0.001 |
| 49.56 | 2.53E-03 | 2.53E-03 | 0.037 |
| 99.62 | 3.61E-03 | 3.62E-03 | 0.224 |
| 149.19 | 4.45E-03 | 4.45E-03 | 0.082 |
| 198.06 | 5.15E-03 | 5.15E-03 | 0.117 |
| 347.64 | 6.89E-03 | 6.87E-03 | 0.263 |
| 496.03 | 8.25E-03 | 8.22E-03 | 0.376 |
| 644.63 | 9.35E-03 | 9.38E-03 | 0.263 |
| 875.84 | 1.09E-02 | 1.09E-02 | 0.229 |
| 893.34 | 1.10E-02 | 1.10E-02 | 0.050 |
| 983.72 | 1.15E-02 | 1.16E-02 | 0.335 |
| 991.67 | 1.16E-02 | 1.16E-02 | 0.035 |
| 1967.45 | 1.62E-02 | 1.62E-02 | 0.251 |
| 2966.87 | 1.97E-02 | 1.97E-02 | 0.027 |
| 3916.26 | 2.25E-02 | 2.24E-02 | 0.083 |
| 4919.60 | 2.49E-02 | 2.49E-02 | 0.004 |
| 5892.54 | 2.71E-02 | 2.71E-02 | 0.078 |
| 6849.78 | 2.90E-02 | 2.90E-02 | 0.080 |
| 7825.66 | 3.07E-02 | 3.07E-02 | 0.034 |
| 8823.12 | 3.24E-02 | 3.24E-02 | 0.105 |
| 9801.94 | 3.39E-02 | 3.39E-02 | 0.017 |
| | | **Average Percent Difference** | 0.135 |
| | | **Maximum Percent Difference** | 0.376 |
| | | **Minimum Percent Difference** | 0.001 |

Table A.3: Comparison of the mass flow rates reported in the calibration data and the corresponding values obtained using an iterative method (details in Section 3.5.1.2)

# Appendix B – Experimental Data for Determining Permeability and Dimensionless Form-Drag Coefficient

| M20-1 (Run #1) | | | | M20-1 (Run #2) | | | |
|---|---|---|---|---|---|---|---|
| *u* (m/s) | *(-dp/dx)* (Pa/m) | $\rho$ (kg/m$^3$) | $\mu$ (Pa·s) | *u* (m/s) | *(-dp/dx)* (Pa/m) | $\rho$ (kg/m$^3$) | $\mu$ (Pa·s) |
| 0.06119 | 12.88 | 1.1547 | 1.8287E-05 | 0.06079 | 12.81 | 1.1637 | 1.8285E-05 |
| 0.07692 | 16.51 | 1.1552 | 1.8282E-05 | 0.07659 | 16.55 | 1.1641 | 1.8280E-05 |
| 0.09095 | 20.13 | 1.1668 | 1.8284E-05 | 0.09125 | 20.42 | 1.1646 | 1.8276E-05 |
| 0.09170 | 20.35 | 1.1554 | 1.8279E-05 | 0.09223 | 20.53 | 1.1593 | 1.8273E-05 |
| 0.10669 | 24.65 | 1.1556 | 1.8277E-05 | 0.10706 | 24.71 | 1.1646 | 1.8275E-05 |
| 0.12197 | 28.74 | 1.1559 | 1.8274E-05 | 0.12226 | 29.01 | 1.1649 | 1.8274E-05 |
| 0.15292 | 38.03 | 1.1560 | 1.8276E-05 | 0.15194 | 37.66 | 1.1652 | 1.8273E-05 |
| 0.18303 | 47.25 | 1.1562 | 1.8277E-05 | 0.18256 | 46.97 | 1.1583 | 1.8277E-05 |
| 0.18309 | 47.26 | 1.1666 | 1.8281E-05 | 0.18264 | 47.52 | 1.1656 | 1.8273E-05 |
| 0.24454 | 68.29 | 1.1563 | 1.8277E-05 | 0.24221 | 67.75 | 1.1658 | 1.8274E-05 |
| 0.30449 | 91.55 | 1.1665 | 1.8280E-05 | 0.30456 | 91.03 | 1.1577 | 1.8278E-05 |
| 0.30456 | 91.64 | 1.1566 | 1.8275E-05 | 0.30472 | 91.90 | 1.1660 | 1.8274E-05 |
| 0.45579 | 165.87 | 1.1657 | 1.8280E-05 | 0.45612 | 164.99 | 1.1558 | 1.8279E-05 |
| 0.59505 | 254.92 | 1.1649 | 1.8281E-05 | 0.58527 | 248.35 | 1.1547 | 1.8280E-05 |
| 0.88066 | 475.71 | 1.1636 | 1.8281E-05 | 0.89508 | 484.97 | 1.1534 | 1.8280E-05 |
| 1.18815 | 783.72 | 1.1616 | 1.8282E-05 | 1.21597 | 809.88 | 1.1520 | 1.8280E-05 |
| 1.51123 | 1182.02 | 1.1598 | 1.8280E-05 | 1.52273 | 1185.47 | 1.1505 | 1.8279E-05 |
| 1.83167 | 1642.70 | 1.1581 | 1.8278E-05 | 1.84091 | 1653.39 | 1.1489 | 1.8278E-05 |
| 2.13733 | 2155.00 | 1.1559 | 1.8277E-05 | 2.13996 | 2152.02 | 1.1471 | 1.8277E-05 |
| 2.44601 | 2757.84 | 1.1535 | 1.8276E-05 | 2.47441 | 2801.91 | 1.1447 | 1.8278E-05 |
| 3.08517 | 4211.53 | 1.1492 | 1.8275E-05 | 3.09694 | 4212.81 | 1.1402 | 1.8279E-05 |
| 3.69703 | 5854.89 | 1.1444 | 1.8275E-05 | 3.72467 | 5893.85 | 1.1351 | 1.8280E-05 |
| 4.32095 | 7789.82 | 1.1389 | 1.8273E-05 | 4.34382 | 7831.46 | 1.1294 | 1.8280E-05 |
| 4.95791 | 10011.43 | 1.1322 | 1.8272E-05 | 4.99634 | 10097.06 | 1.1226 | 1.8282E-05 |

Table B.1: Data for determining $K$ and $c_F$ - M20-1, Runs #1 and #2

| M40-1 (Run #1) | | | | M40-1 (Run #2) | | | |
|---|---|---|---|---|---|---|---|
| *u* (m/s) | *(-dp/dx)* (Pa/m) | $\rho$ (kg/m$^3$) | $\mu$ (Pa·s) | *u* (m/s) | *(-dp/dx)* (Pa/m) | $\rho$ (kg/m$^3$) | $\mu$ (Pa·s) |
| 0.01665 | 13.80 | 1.1876 | 1.8203E-05 | 0.01721 | 13.70 | 1.1803 | 1.829E-05 |
| 0.03275 | 26.99 | 1.1868 | 1.8213E-05 | 0.03343 | 27.86 | 1.1799 | 1.829E-05 |
| 0.03388 | 28.25 | 1.1785 | 1.8292E-05 | 0.03364 | 27.92 | 1.1787 | 1.827E-05 |
| 0.04959 | 41.62 | 1.1859 | 1.8226E-05 | 0.04991 | 42.04 | 1.1796 | 1.829E-05 |
| 0.06605 | 56.32 | 1.1790 | 1.8286E-05 | 0.06644 | 56.54 | 1.1796 | 1.830E-05 |
| 0.06607 | 55.90 | 1.1846 | 1.8239E-05 | 0.06669 | 56.03 | 1.1785 | 1.827E-05 |
| 0.09922 | 87.49 | 1.1833 | 1.8250E-05 | 0.09956 | 87.89 | 1.1792 | 1.830E-05 |
| 0.13276 | 120.91 | 1.1822 | 1.8260E-05 | 0.13286 | 121.31 | 1.1791 | 1.830E-05 |
| 0.13291 | 121.32 | 1.1792 | 1.8283E-05 | 0.13287 | 121.46 | 1.1783 | 1.828E-05 |
| 0.19882 | 192.94 | 1.1813 | 1.8268E-05 | 0.19975 | 194.45 | 1.1783 | 1.828E-05 |
| 0.19974 | 193.62 | 1.1788 | 1.8281E-05 | 0.20001 | 194.39 | 1.1789 | 1.830E-05 |
| 0.26497 | 271.86 | 1.1805 | 1.8274E-05 | 0.26635 | 273.26 | 1.1786 | 1.831E-05 |
| 0.33127 | 361.21 | 1.1782 | 1.8281E-05 | 0.33031 | 360.28 | 1.1782 | 1.828E-05 |
| 0.33180 | 361.39 | 1.1797 | 1.8280E-05 | 0.33204 | 362.63 | 1.1783 | 1.831E-05 |
| 0.49531 | 636.55 | 1.1770 | 1.8280E-05 | 0.49606 | 639.14 | 1.1778 | 1.828E-05 |
| 0.62349 | 910.89 | 1.1758 | 1.8282E-05 | 0.62150 | 915.74 | 1.1768 | 1.828E-05 |
| 0.80060 | 1324.55 | 1.1743 | 1.8283E-05 | 0.80317 | 1338.90 | 1.1760 | 1.828E-05 |
| 0.97564 | 1799.71 | 1.1730 | 1.8282E-05 | 0.96841 | 1798.59 | 1.1749 | 1.828E-05 |
| 1.11900 | 2257.08 | 1.1720 | 1.8279E-05 | 1.12291 | 2275.57 | 1.1737 | 1.828E-05 |
| 1.29390 | 2864.51 | 1.1703 | 1.8276E-05 | 1.28028 | 2844.94 | 1.1728 | 1.828E-05 |
| 1.62451 | 4208.36 | 1.1670 | 1.8274E-05 | 1.64511 | 4350.00 | 1.1690 | 1.828E-05 |
| 1.97115 | 5846.68 | 1.1629 | 1.8273E-05 | 1.95967 | 5866.37 | 1.1654 | 1.828E-05 |
| 2.64042 | 9725.58 | 1.1527 | 1.8272E-05 | 2.64300 | 9829.74 | 1.1553 | 1.828E-05 |
| 3.31319 | 14521.68 | 1.1406 | 1.8270E-05 | 3.30430 | 14593.96 | 1.1432 | 1.827E-05 |

Table B.2: Data for determining $K$ and $c_F$ - M40-1, Runs #1 and #2

| M60-2 (Run #1) | | | | M60-2 (Run #2) | | | |
|---|---|---|---|---|---|---|---|
| ***u*** **(m/s)** | ***(-dp/dx)*** **(Pa/m)** | **ρ (kg/m$^3$)** | **μ (Pa·s)** | ***u*** **(m/s)** | ***(-dp/dx)*** **(Pa/m)** | **ρ (kg/m$^3$)** | **μ (Pa·s)** |
| 0.01853 | 33.75 | 1.1772 | 1.826E-05 | 0.01926 | 34.89 | 1.1714 | 1.829E-05 |
| 0.03769 | 60.20 | 1.1615 | 1.829E-05 | 0.03767 | 68.27 | 1.1713 | 1.829E-05 |
| 0.03770 | 68.19 | 1.1762 | 1.826E-05 | 0.03843 | 61.16 | 1.1728 | 1.826E-05 |
| 0.05641 | 102.07 | 1.1750 | 1.827E-05 | 0.05632 | 102.20 | 1.1714 | 1.829E-05 |
| 0.07471 | 136.65 | 1.1740 | 1.828E-05 | 0.07522 | 122.35 | 1.1723 | 1.826E-05 |
| 0.07557 | 122.91 | 1.1609 | 1.830E-05 | 0.07548 | 138.43 | 1.1715 | 1.830E-05 |
| 0.11236 | 209.27 | 1.1730 | 1.828E-05 | 0.11291 | 210.72 | 1.1715 | 1.830E-05 |
| 0.15003 | 254.49 | 1.1605 | 1.831E-05 | 0.14897 | 252.71 | 1.1716 | 1.827E-05 |
| 0.15004 | 284.62 | 1.1721 | 1.828E-05 | 0.14985 | 284.96 | 1.1713 | 1.830E-05 |
| 0.22562 | 397.19 | 1.1598 | 1.832E-05 | 0.22462 | 394.95 | 1.1706 | 1.827E-05 |
| 0.22585 | 442.11 | 1.1714 | 1.829E-05 | 0.22567 | 441.25 | 1.1712 | 1.830E-05 |
| 0.29990 | 603.27 | 1.1704 | 1.829E-05 | 0.30186 | 608.47 | 1.1705 | 1.830E-05 |
| 0.37611 | 709.26 | 1.1591 | 1.832E-05 | 0.37312 | 703.29 | 1.1692 | 1.828E-05 |
| 0.37620 | 785.70 | 1.1697 | 1.829E-05 | 0.37553 | 785.37 | 1.1697 | 1.830E-05 |
| 0.56152 | 1182.73 | 1.1581 | 1.832E-05 | 0.56008 | 1176.66 | 1.1678 | 1.828E-05 |
| 0.73775 | 1742.61 | 1.1567 | 1.833E-05 | 0.70675 | 1636.46 | 1.1669 | 1.828E-05 |
| 0.92512 | 2377.26 | 1.1551 | 1.833E-05 | 0.90667 | 2320.78 | 1.1653 | 1.828E-05 |
| 1.09013 | 3025.12 | 1.1532 | 1.833E-05 | 1.09283 | 3049.00 | 1.1632 | 1.828E-05 |
| 1.29130 | 3866.18 | 1.1512 | 1.833E-05 | 1.26964 | 3789.21 | 1.1613 | 1.828E-05 |
| 1.47231 | 4697.37 | 1.1490 | 1.833E-05 | 1.45120 | 4604.11 | 1.1594 | 1.827E-05 |
| 1.85765 | 6642.01 | 1.1436 | 1.834E-05 | 1.87143 | 6724.70 | 1.1539 | 1.827E-05 |
| 2.25817 | 8953.07 | 1.1373 | 1.834E-05 | 2.22294 | 8773.77 | 1.1484 | 1.827E-05 |
| 2.63757 | 11421.66 | 1.1305 | 1.834E-05 | 2.61217 | 11277.44 | 1.1418 | 1.827E-05 |
| 3.03741 | 14270.14 | 1.1229 | 1.834E-05 | 3.01575 | 14183.71 | 1.1339 | 1.827E-05 |

Table B.3: Data for determining $K$ and $c_F$ - M60-2, Runs #1 and #2

| ERG40 (Run #1) | | | | ERG40 (Run #2) | | | |
|---|---|---|---|---|---|---|---|
| ***u*** **(m/s)** | ***(-dp/dx)*** **(Pa/m)** | **ρ (kg/m$^3$)** | **μ (Pa·s)** | ***u*** **(m/s)** | ***(-dp/dx)*** **(Pa/m)** | **ρ (kg/m$^3$)** | **μ (Pa·s)** |
| 0.06654 | 19.54 | 1.1549 | 1.829E-05 | 0.06640 | 19.25 | 1.1499 | 1.828E-05 |
| 0.08358 | 24.90 | 1.1543 | 1.829E-05 | 0.08350 | 25.00 | 1.1496 | 1.828E-05 |
| 0.09969 | 30.47 | 1.1536 | 1.829E-05 | 0.09950 | 30.30 | 1.1491 | 1.828E-05 |
| 0.10045 | 30.53 | 1.1535 | 1.829E-05 | 0.11587 | 36.06 | 1.1489 | 1.829E-05 |
| 0.11656 | 36.68 | 1.1539 | 1.829E-05 | 0.13303 | 42.25 | 1.1488 | 1.829E-05 |
| 0.13381 | 42.69 | 1.1527 | 1.829E-05 | 0.16526 | 54.73 | 1.1491 | 1.829E-05 |
| 0.16650 | 55.47 | 1.1523 | 1.829E-05 | 0.20021 | 68.21 | 1.1498 | 1.829E-05 |
| 0.19970 | 68.52 | 1.1545 | 1.829E-05 | 0.26544 | 96.65 | 1.1500 | 1.828E-05 |
| 0.20000 | 68.42 | 1.1520 | 1.829E-05 | 0.33394 | 129.67 | 1.1502 | 1.828E-05 |
| 0.26665 | 97.33 | 1.1515 | 1.829E-05 | 0.49724 | 227.32 | 1.1501 | 1.828E-05 |
| 0.33269 | 129.32 | 1.1535 | 1.829E-05 | 0.64038 | 338.51 | 1.1496 | 1.828E-05 |
| 0.33322 | 129.66 | 1.1513 | 1.830E-05 | 0.97714 | 634.32 | 1.1488 | 1.828E-05 |
| 0.49112 | 224.34 | 1.1534 | 1.829E-05 | 1.31239 | 1007.29 | 1.1480 | 1.828E-05 |
| 0.62814 | 328.36 | 1.1524 | 1.829E-05 | 1.65036 | 1470.29 | 1.1468 | 1.828E-05 |
| 0.96816 | 628.38 | 1.1511 | 1.829E-05 | 2.00246 | 2021.48 | 1.1455 | 1.828E-05 |
| 1.31350 | 1011.79 | 1.1495 | 1.829E-05 | 2.34195 | 2635.94 | 1.1443 | 1.828E-05 |
| 1.66304 | 1491.25 | 1.1485 | 1.829E-05 | 2.68963 | 3363.91 | 1.1424 | 1.828E-05 |
| 1.99743 | 2013.34 | 1.1475 | 1.829E-05 | 3.36588 | 4953.97 | 1.1382 | 1.828E-05 |
| 2.33908 | 2635.33 | 1.1454 | 1.829E-05 | 4.06086 | 6870.09 | 1.1328 | 1.827E-05 |
| 2.68733 | 3356.19 | 1.1438 | 1.829E-05 | 4.74020 | 9034.72 | 1.1269 | 1.827E-05 |
| 3.38062 | 4988.14 | 1.1394 | 1.829E-05 | 5.36825 | 11235.94 | 1.1206 | 1.827E-05 |
| 4.05194 | 6855.09 | 1.1344 | 1.829E-05 | | | | |
| 4.71699 | 9007.80 | 1.1287 | 1.828E-05 | | | | |
| 5.35441 | 11254.77 | 1.1227 | 1.828E-05 | | | | |

Table B.4: Data for determining $K$ and $c_F$ - ERG40, Runs #1 and #2

| M20-2 | | | | M40-2 | | | |
|---|---|---|---|---|---|---|---|
| ***u*** **(m/s)** | ***(-dp/dx)*** **(Pa/m)** | $\rho$ **(kg/m$^3$)** | **μ (Pa·s)** | ***u*** **(m/s)** | ***(-dp/dx)*** **(Pa/m)** | $\rho$ **(kg/m$^3$)** | **μ (Pa·s)** |
| 0.06168 | 11.80 | 1.1508 | 1.8282E-05 | 0.01660 | 15.01 | 1.1785 | 1.8245E-05 |
| 0.07629 | 14.92 | 1.1507 | 1.8279E-05 | 0.03301 | 29.98 | 1.1782 | 1.8248E-05 |
| 0.09136 | 18.71 | 1.1506 | 1.8278E-05 | 0.03325 | 30.30 | 1.1828 | 1.8283E-05 |
| 0.09159 | 18.98 | 1.1826 | 1.8261E-05 | 0.04912 | 44.90 | 1.1777 | 1.8252E-05 |
| 0.10581 | 22.12 | 1.1505 | 1.8277E-05 | 0.06607 | 61.59 | 1.1770 | 1.8258E-05 |
| 0.12192 | 26.37 | 1.1504 | 1.8276E-05 | 0.06657 | 62.43 | 1.1826 | 1.8280E-05 |
| 0.15142 | 34.12 | 1.1505 | 1.8275E-05 | 0.09895 | 95.75 | 1.1766 | 1.8264E-05 |
| 0.18155 | 42.67 | 1.1506 | 1.8276E-05 | 0.13148 | 131.50 | 1.1827 | 1.8277E-05 |
| 0.18210 | 43.11 | 1.1819 | 1.8260E-05 | 0.13208 | 132.68 | 1.1759 | 1.8270E-05 |
| 0.24080 | 60.64 | 1.1506 | 1.8275E-05 | 0.19766 | 212.69 | 1.1821 | 1.8276E-05 |
| 0.30160 | 82.10 | 1.1505 | 1.8276E-05 | 0.19792 | 213.09 | 1.1755 | 1.8275E-05 |
| 0.30180 | 82.74 | 1.1813 | 1.8260E-05 | 0.26398 | 302.19 | 1.1752 | 1.8281E-05 |
| 0.45129 | 148.73 | 1.1803 | 1.8261E-05 | 0.32961 | 402.96 | 1.1812 | 1.8274E-05 |
| 0.57476 | 221.56 | 1.1799 | 1.8263E-05 | 0.32999 | 404.04 | 1.1751 | 1.8284E-05 |
| 0.87038 | 423.42 | 1.1789 | 1.8264E-05 | 0.49092 | 716.43 | 1.1799 | 1.8273E-05 |
| 1.18038 | 705.48 | 1.1776 | 1.8265E-05 | 0.61896 | 1034.66 | 1.1786 | 1.8274E-05 |
| 1.48021 | 1036.29 | 1.1760 | 1.8266E-05 | 0.78783 | 1495.49 | 1.1770 | 1.8274E-05 |
| 1.79724 | 1448.51 | 1.1751 | 1.8267E-05 | 0.94818 | 2015.12 | 1.1754 | 1.8274E-05 |
| 2.10863 | 1924.17 | 1.1737 | 1.8268E-05 | 1.11766 | 2658.73 | 1.1736 | 1.8272E-05 |
| 2.42814 | 2485.27 | 1.1716 | 1.8268E-05 | 1.27370 | 3327.56 | 1.1716 | 1.8272E-05 |
| 3.03424 | 3758.42 | 1.1679 | 1.8267E-05 | 1.61425 | 4977.44 | 1.1679 | 1.8270E-05 |
| 3.65631 | 5285.81 | 1.1635 | 1.8266E-05 | 1.97136 | 7081.83 | 1.1628 | 1.8270E-05 |
| 4.25837 | 6988.82 | 1.1585 | 1.8267E-05 | 2.62882 | 11668.48 | 1.1516 | 1.8270E-05 |
| 4.89353 | 8998.63 | 1.1527 | 1.8266E-05 | 3.09350 | 15572.51 | 1.1422 | 1.8269E-05 |

Table B.5: Data for determining $K$ and $c_F$ - M20-2 and M40-2

| M60-1 | | | |
|---|---|---|---|
| ***u*** **(m/s)** | ***(-dp/dx)*** **(Pa/m)** | $\rho$ **(kg/m$^3$)** | **M (Pa·s)** |
| 0.01805 | 32.73 | 1.1829 | 1.8254E-05 |
| 0.03538 | 64.30 | 1.1817 | 1.8263E-05 |
| 0.03650 | 63.34 | 1.1666 | 1.8303E-05 |
| 0.05340 | 97.45 | 1.1801 | 1.8271E-05 |
| 0.07085 | 130.75 | 1.1791 | 1.8278E-05 |
| 0.07136 | 126.24 | 1.1655 | 1.8313E-05 |
| 0.10626 | 200.01 | 1.1784 | 1.8283E-05 |
| 0.14093 | 271.03 | 1.1780 | 1.8286E-05 |
| 0.14206 | 262.45 | 1.1639 | 1.8322E-05 |
| 0.21238 | 422.06 | 1.1769 | 1.8291E-05 |
| 0.21311 | 408.66 | 1.1613 | 1.8331E-05 |
| 0.28323 | 581.98 | 1.1759 | 1.8295E-05 |
| 0.35414 | 731.43 | 1.1592 | 1.8339E-05 |
| 0.35679 | 764.66 | 1.1749 | 1.8297E-05 |
| 0.53049 | 1234.74 | 1.1564 | 1.8347E-05 |
| 0.70303 | 1836.07 | 1.1534 | 1.8354E-05 |
| 0.85998 | 2441.86 | 1.1510 | 1.8359E-05 |
| 1.04101 | 3230.30 | 1.1485 | 1.8364E-05 |
| 1.23314 | 4145.20 | 1.1453 | 1.8368E-05 |
| 1.39721 | 4997.16 | 1.1420 | 1.8371E-05 |
| 1.75746 | 7094.90 | 1.1356 | 1.8375E-05 |
| 2.13414 | 9584.15 | 1.1267 | 1.8378E-05 |
| 2.49187 | 12316.95 | 1.1190 | 1.8380E-05 |
| 2.84416 | 15284.72 | 1.1100 | 1.8383E-05 |

Table B.6: Data for determining $K$ and $c_F$ - M60-1

# Appendix C – Data for Fully Developed Fluid Flows in Straight Rectangular Duct with Adjacent Open and Porous Domains

Data collected in the experiments on fully developed fluid flows in straight rectangular ducts with adjacent open and porous domains, for each of the porous metal foams and open-domain heights (1/8", 1/4", and 1/2"), are summarized below in Tables C.1-C.15: the Reynolds number in the open domain of the test section, $\mathrm{Re}_{od}^{D_h}$; the total mass flow rate flowing through the test section, $\dot{m}_{total}$; the percentage of the total mass flow rate flowing through the open domain of the test section, $\%\dot{m}_{od}$; the percentage of the total mass flow rate flowing through the porous domain of the test section, $\%\dot{m}_{pd}$; mean values of the absolute temperature, dynamic viscosity, and density of air within the test section, $T_{abs}$, $\mu$, and $\rho$, respectively; axial gradient of time-averaged wall-static pressure in the test section, $(-dp/dx)$; time-averaged wall-shear stress at the top wall of the test section, $\tau_w$; and the Darcy friction factor for the open domain of the test section, $f_{D-od}$.

| $(Re_{od})^{Dh}$ | $\dot{m}_{total}$ (kg/s) | $\%\,\dot{m}_{od}$ (kg/s) | $\%\,\dot{m}_{pd}$ (kg/s) | $T_{abs}$ (K) | $\mu$ (*$10^6$ Pa·s) | $\rho$ (kg/m$^3$) | (-dp/dx) (Pa/m) | $\tau_w$ (Pa) | $f_{D-od}$ |
|---|---|---|---|---|---|---|---|---|---|
| 2280.7 | 8.68E-03 | 36.6 | 63.4 | 296.79 | 18.306 | 1.10 | 2340.33 | 1.5686E+00 | 0.0947 |
| 2165.1 | 8.25E-03 | 36.6 | 63.4 | 296.73 | 18.303 | 1.11 | 2125.66 | 1.4427E+00 | 0.0960 |
| 2022.2 | 7.69E-03 | 36.7 | 63.3 | 296.59 | 18.297 | 1.13 | 1828.35 | 1.2726E+00 | 0.0967 |
| 1839.5 | 6.99E-03 | 36.7 | 63.3 | 296.51 | 18.293 | 1.14 | 1534.37 | 1.0987E+00 | 0.0988 |
| 1649.1 | 6.28E-03 | 36.6 | 63.4 | 296.49 | 18.292 | 1.15 | 1263.10 | 9.2506E-01 | 0.1018 |
| 1466.6 | 5.60E-03 | 36.5 | 63.5 | 296.56 | 18.295 | 1.15 | 1029.01 | 7.7415E-01 | 0.1054 |
| 1369.7 | 5.23E-03 | 36.5 | 63.5 | 296.49 | 18.292 | 1.16 | 914.48 | 6.9656E-01 | 0.1077 |
| 1280.8 | 4.89E-03 | 36.5 | 63.5 | 296.49 | 18.292 | 1.16 | 812.42 | 6.2544E-01 | 0.1096 |
| 1186.4 | 4.53E-03 | 36.5 | 63.5 | 296.42 | 18.289 | 1.16 | 710.58 | 5.5270E-01 | 0.1120 |
| 1100.5 | 4.18E-03 | 36.7 | 63.3 | 296.47 | 18.291 | 1.16 | 616.80 | 4.8553E-01 | 0.1132 |
| 1009.8 | 3.82E-03 | 36.9 | 63.1 | 296.54 | 18.295 | 1.17 | 527.57 | 4.1942E-01 | 0.1151 |
| 916.7 | 3.46E-03 | 37.0 | 63.0 | 296.51 | 18.293 | 1.17 | 446.22 | 3.6238E-01 | 0.1183 |
| 826.9 | 3.09E-03 | 37.3 | 62.7 | 296.45 | 18.290 | 1.17 | 368.03 | 3.0534E-01 | 0.1202 |
| 746.6 | 2.78E-03 | 37.5 | 62.5 | 296.60 | 18.297 | 1.17 | 308.87 | 2.5940E-01 | 0.1238 |
| 661.7 | 2.42E-03 | 38.2 | 61.8 | 296.59 | 18.297 | 1.17 | 244.29 | 2.1240E-01 | 0.1247 |
| 589.2 | 2.12E-03 | 38.7 | 61.3 | 296.49 | 18.292 | 1.17 | 197.79 | 1.8125E-01 | 0.1275 |
| 480.3 | 1.69E-03 | 39.6 | 60.4 | 296.45 | 18.290 | 1.17 | 138.59 | 1.3057E-01 | 0.1346 |
| 385.1 | 1.36E-03 | 39.5 | 60.5 | 296.44 | 18.290 | 1.18 | 101.83 | 9.9376E-02 | 0.1540 |
| 303.9 | 1.06E-03 | 40.0 | 60.0 | 296.49 | 18.292 | 1.18 | 71.49 | 6.9205E-02 | 0.1736 |
| 200.5 | 7.05E-04 | 39.6 | 60.4 | 296.45 | 18.290 | 1.18 | 42.57 | 4.0838E-02 | 0.2378 |
| 117.0 | 4.23E-04 | 38.6 | 61.4 | 296.48 | 18.292 | 1.18 | 23.44 | 2.3221E-02 | 0.3842 |
| 37.3 | 1.41E-04 | 36.9 | 63.1 | 296.41 | 18.288 | 1.18 | 7.10 | 1.0300E-02 | 1.1489 |

Table C.1: Data for M20-1 metal foam, and 1/8" open-domain height

| $(Re_{od})^{Dh}$ | $\dot{m}_{total}$ (kg/s) | % $\dot{m}_{od}$ (kg/s) | % $\dot{m}_{pd}$ (kg/s) | $T_{abs}$ (K) | $\mu$ (*$10^6$ Pa·s) | $\rho$ (kg/m$^3$) | (-dp/dx) (Pa/m) | $\tau_w$ (Pa) | $f_{D\text{-}od}$ |
|---|---|---|---|---|---|---|---|---|---|
| 8392.8 | 1.55E-02 | 75.7 | 24.3 | 296.65 | 18.300 | 1.14 | 1152.33 | 1.5742E+00 | 0.0957 |
| 7779.4 | 1.43E-02 | 75.9 | 24.1 | 296.67 | 18.301 | 1.14 | 982.24 | 1.3629E+00 | 0.0954 |
| 7056.4 | 1.29E-02 | 76.1 | 23.9 | 296.69 | 18.302 | 1.15 | 813.96 | 1.1370E+00 | 0.0966 |
| 6315.5 | 1.15E-02 | 76.3 | 23.7 | 296.68 | 18.301 | 1.15 | 655.68 | 9.2762E-01 | 0.0977 |
| 5582.9 | 1.02E-02 | 76.6 | 23.4 | 296.64 | 18.299 | 1.16 | 517.72 | 7.3912E-01 | 0.0991 |
| 4801.8 | 8.71E-03 | 76.9 | 23.1 | 296.70 | 18.302 | 1.16 | 394.61 | 5.6155E-01 | 0.1025 |
| 4413.3 | 7.99E-03 | 77.0 | 23.0 | 296.74 | 18.304 | 1.17 | 339.16 | 4.8144E-01 | 0.1044 |
| 4008.7 | 7.24E-03 | 77.2 | 22.8 | 296.69 | 18.302 | 1.17 | 287.27 | 4.0757E-01 | 0.1074 |
| 3620.9 | 6.52E-03 | 77.4 | 22.6 | 296.69 | 18.302 | 1.17 | 240.02 | 3.4164E-01 | 0.1101 |
| 3219.2 | 5.78E-03 | 77.7 | 22.3 | 296.67 | 18.301 | 1.17 | 195.01 | 2.7985E-01 | 0.1135 |
| 3022.2 | 5.41E-03 | 77.9 | 22.1 | 296.68 | 18.301 | 1.17 | 174.92 | 2.5053E-01 | 0.1155 |
| 2816.4 | 5.03E-03 | 78.1 | 21.9 | 296.72 | 18.303 | 1.17 | 154.94 | 2.2254E-01 | 0.1179 |
| 2616.0 | 4.66E-03 | 78.3 | 21.7 | 296.71 | 18.303 | 1.17 | 136.06 | 1.9979E-01 | 0.1200 |
| 2418.7 | 4.29E-03 | 78.6 | 21.4 | 296.69 | 18.302 | 1.17 | 118.45 | 1.7636E-01 | 0.1223 |
| 2226.2 | 3.93E-03 | 79.1 | 20.9 | 296.68 | 18.301 | 1.17 | 101.54 | 1.5306E-01 | 0.1238 |
| 2010.3 | 3.53E-03 | 79.4 | 20.6 | 296.74 | 18.304 | 1.17 | 85.77 | 1.2998E-01 | 0.1282 |
| 1828.3 | 3.19E-03 | 80.0 | 20.0 | 296.71 | 18.303 | 1.18 | 71.61 | 1.1064E-01 | 0.1295 |
| 1625.8 | 2.81E-03 | 80.7 | 19.3 | 296.68 | 18.301 | 1.18 | 57.87 | 9.1148E-02 | 0.1324 |
| 1433.4 | 2.45E-03 | 81.6 | 18.4 | 296.65 | 18.300 | 1.18 | 45.90 | 7.3506E-02 | 0.1351 |
| 1241.5 | 2.10E-03 | 82.5 | 17.5 | 296.75 | 18.304 | 1.18 | 35.60 | 5.7987E-02 | 0.1396 |
| 1030.2 | 1.72E-03 | 83.3 | 16.7 | 296.60 | 18.297 | 1.18 | 26.49 | 4.3403E-02 | 0.1510 |
| 876.1 | 1.45E-03 | 84.3 | 15.7 | 296.68 | 18.301 | 1.18 | 20.12 | 3.3518E-02 | 0.1585 |
| 664.8 | 1.08E-03 | 85.8 | 14.2 | 296.71 | 18.302 | 1.18 | 12.91 | 2.2048E-02 | 0.1766 |
| 461.7 | 7.20E-04 | 89.4 | 10.6 | 296.72 | 18.303 | 1.18 | 6.05 | 1.4883E-02 | 0.1715 |

Table C.2: Data for M20-1 metal foam, and 1/4” open-domain height

| $(Re_{od})^{Dh}$ | $\dot{m}_{total}$ (kg/s) | % $\dot{m}_{od}$ (kg/s) | % $\dot{m}_{pd}$ (kg/s) | $T_{abs}$ (K) | $\mu$ (*$10^6$ Pa·s) | $\rho$ (kg/m$^3$) | (-dp/dx) (Pa/m) | $\tau_w$ (Pa) | $f_{D\text{-}od}$ |
|---|---|---|---|---|---|---|---|---|---|
| 13664.0 | 2.05E-02 | 93.3 | 6.7 | 297.35 | 18.333 | 1.16 | 214.68 | 6.7856E-01 | 0.0891 |
| 12886.3 | 1.93E-02 | 93.4 | 6.6 | 297.35 | 18.333 | 1.16 | 191.21 | 6.0135E-01 | 0.0893 |
| 11971.6 | 1.79E-02 | 93.6 | 6.4 | 297.33 | 18.332 | 1.16 | 164.25 | 5.2000E-01 | 0.0891 |
| 11015.5 | 1.64E-02 | 93.8 | 6.2 | 297.34 | 18.333 | 1.17 | 136.87 | 4.3677E-01 | 0.0878 |
| 10109.2 | 1.50E-02 | 94.0 | 6.0 | 297.34 | 18.333 | 1.17 | 115.16 | 3.6563E-01 | 0.0879 |
| 9155.0 | 1.36E-02 | 94.3 | 5.7 | 297.35 | 18.333 | 1.17 | 94.89 | 2.9928E-01 | 0.0884 |
| 8198.2 | 1.21E-02 | 94.5 | 5.5 | 297.35 | 18.333 | 1.17 | 76.99 | 2.4428E-01 | 0.0896 |
| 7187.2 | 1.06E-02 | 94.7 | 5.3 | 297.35 | 18.333 | 1.17 | 60.38 | 1.9465E-01 | 0.0915 |
| 6212.8 | 9.13E-03 | 95.1 | 4.9 | 297.33 | 18.332 | 1.17 | 45.89 | 1.5120E-01 | 0.0932 |
| 5164.7 | 7.56E-03 | 95.4 | 4.6 | 297.33 | 18.332 | 1.18 | 32.93 | 1.1124E-01 | 0.0968 |
| 4635.4 | 6.77E-03 | 95.6 | 4.4 | 297.34 | 18.333 | 1.18 | 27.25 | 9.3299E-02 | 0.0995 |
| 4122.5 | 6.01E-03 | 95.9 | 4.1 | 297.35 | 18.333 | 1.18 | 22.05 | 7.6692E-02 | 0.1018 |
| 3884.5 | 5.65E-03 | 96.1 | 3.9 | 297.36 | 18.334 | 1.18 | 19.57 | 6.9835E-02 | 0.1018 |
| 3619.8 | 5.25E-03 | 96.2 | 3.8 | 297.38 | 18.335 | 1.18 | 17.11 | 6.2162E-02 | 0.1025 |
| 3338.2 | 4.84E-03 | 96.4 | 3.6 | 297.40 | 18.336 | 1.18 | 14.67 | 5.4692E-02 | 0.1033 |
| 3108.4 | 4.49E-03 | 96.7 | 3.3 | 297.41 | 18.336 | 1.18 | 12.47 | 4.9645E-02 | 0.1013 |
| 2828.9 | 4.08E-03 | 96.8 | 3.2 | 297.24 | 18.328 | 1.18 | 10.75 | 4.4850E-02 | 0.1056 |
| 2569.7 | 3.71E-03 | 96.9 | 3.1 | 297.32 | 18.332 | 1.18 | 9.47 | 3.9681E-02 | 0.1126 |
| 2318.3 | 3.34E-03 | 97.1 | 2.9 | 297.39 | 18.335 | 1.18 | 7.82 | 3.5464E-02 | 0.1142 |
| 2048.7 | 2.93E-03 | 97.5 | 2.5 | 297.24 | 18.328 | 1.18 | 5.77 | 3.0702E-02 | 0.1080 |
| 1811.9 | 2.58E-03 | 98.1 | 1.9 | 297.31 | 18.331 | 1.18 | 3.74 | 2.6182E-02 | 0.0895 |

Table C.3: Data for M20-1 metal foam, and 1/2” open-domain height

| $(Re_{od})^{Dh}$ | $\dot{m}_{total}$ (kg/s) | % $\dot{m}_{od}$ (kg/s) | % $\dot{m}_{pd}$ (kg/s) | $T_{abs}$ (K) | $\mu$ (*$10^6$ Pa·s) | $\rho$ (kg/m$^3$) | (-dp/dx) (Pa/m) | $\tau_w$ (Pa) | $f_{D\text{-}od}$ |
|---|---|---|---|---|---|---|---|---|---|
| 4692.2 | 8.92E-03 | 73.4 | 26.6 | 296.93 | 18.313 | 1.09 | 2072.44 | 1.9199E+00 | 0.1047 |
| 4351.9 | 8.26E-03 | 73.5 | 26.5 | 296.94 | 18.314 | 1.09 | 1827.48 | 1.6933E+00 | 0.1074 |
| 4027.4 | 7.62E-03 | 73.8 | 26.2 | 296.96 | 18.315 | 1.10 | 1570.46 | 1.4810E+00 | 0.1086 |
| 3680.1 | 6.94E-03 | 74.0 | 26.0 | 296.98 | 18.316 | 1.11 | 1329.53 | 1.2807E+00 | 0.1109 |
| 3324.2 | 6.24E-03 | 74.3 | 25.7 | 296.95 | 18.314 | 1.11 | 1106.43 | 1.0887E+00 | 0.1139 |
| 2965.9 | 5.54E-03 | 74.7 | 25.3 | 296.98 | 18.315 | 1.12 | 900.09 | 8.9062E-01 | 0.1171 |
| 2792.3 | 5.20E-03 | 74.9 | 25.1 | 297.00 | 18.316 | 1.12 | 808.63 | 7.9980E-01 | 0.1190 |
| 2611.3 | 4.85E-03 | 75.2 | 24.8 | 296.96 | 18.314 | 1.13 | 714.75 | 7.1609E-01 | 0.1208 |
| 2431.0 | 4.49E-03 | 75.5 | 24.5 | 296.96 | 18.315 | 1.13 | 627.91 | 6.3131E-01 | 0.1227 |
| 2253.6 | 4.14E-03 | 75.9 | 24.1 | 296.96 | 18.315 | 1.13 | 548.22 | 5.5408E-01 | 0.1250 |
| 2077.0 | 3.80E-03 | 76.3 | 23.7 | 296.97 | 18.315 | 1.14 | 474.95 | 4.7854E-01 | 0.1277 |
| 1898.7 | 3.45E-03 | 76.8 | 23.2 | 296.93 | 18.313 | 1.14 | 404.22 | 4.0600E-01 | 0.1304 |
| 1721.5 | 3.10E-03 | 77.5 | 22.5 | 296.95 | 18.314 | 1.14 | 337.03 | 3.4118E-01 | 0.1325 |
| 1537.1 | 2.75E-03 | 78.1 | 21.9 | 296.96 | 18.315 | 1.14 | 276.52 | 2.8104E-01 | 0.1366 |
| 1375.4 | 2.43E-03 | 79.0 | 21.0 | 296.95 | 18.314 | 1.14 | 225.09 | 2.3317E-01 | 0.1392 |
| 1187.6 | 2.07E-03 | 80.2 | 19.8 | 296.92 | 18.313 | 1.15 | 171.42 | 1.8602E-01 | 0.1424 |
| 1003.6 | 1.72E-03 | 81.6 | 18.4 | 296.93 | 18.313 | 1.15 | 125.65 | 1.3952E-01 | 0.1464 |
| 828.8 | 1.39E-03 | 83.2 | 16.8 | 296.95 | 18.314 | 1.15 | 88.45 | 1.0117E-01 | 0.1513 |
| 639.7 | 1.04E-03 | 85.6 | 14.4 | 296.94 | 18.314 | 1.15 | 54.58 | 6.5036E-02 | 0.1569 |
| 439.7 | 6.98E-04 | 87.8 | 12.2 | 296.93 | 18.313 | 1.15 | 29.57 | 3.7143E-02 | 0.1801 |
| 265.7 | 4.20E-04 | 88.3 | 11.7 | 296.95 | 18.314 | 1.15 | 16.73 | 2.1855E-02 | 0.2792 |
| 88.2 | 1.40E-04 | 88.1 | 11.9 | 296.93 | 18.313 | 1.15 | 5.57 | 8.4152E-03 | 0.8441 |

Table C.4: Data for M40-1 metal foam, and 1/8” open-domain height

| $(Re_{od})^{Dh}$ | $\dot{m}_{total}$ (kg/s) | % $\dot{m}_{od}$ (kg/s) | % $\dot{m}_{pd}$ (kg/s) | $T_{abs}$ (K) | $\mu$ (*$10^6$ Pa·s) | $\rho$ (kg/m$^3$) | (-dp/dx) (Pa/m) | $\tau_w$ (Pa) | $f_{D\text{-}od}$ |
|---|---|---|---|---|---|---|---|---|---|
| 10207.7 | 1.57E-02 | 90.8 | 9.2 | 296.63 | 18.299 | 1.14 | 920.72 | 1.5296E+00 | 0.1014 |
| 9419.6 | 1.44E-02 | 91.1 | 8.9 | 296.63 | 18.299 | 1.15 | 770.27 | 1.3023E+00 | 0.1002 |
| 8542.3 | 1.30E-02 | 91.4 | 8.6 | 296.64 | 18.299 | 1.15 | 628.12 | 1.0798E+00 | 0.0999 |
| 7652.8 | 1.16E-02 | 91.8 | 8.2 | 296.61 | 18.298 | 1.16 | 503.36 | 8.7177E-01 | 0.1003 |
| 6771.0 | 1.02E-02 | 92.2 | 7.8 | 296.59 | 18.297 | 1.16 | 392.97 | 6.8451E-01 | 0.1004 |
| 5835.0 | 8.78E-03 | 92.6 | 7.4 | 296.53 | 18.294 | 1.17 | 296.83 | 5.1769E-01 | 0.1026 |
| 5373.2 | 8.06E-03 | 92.9 | 7.1 | 296.64 | 18.299 | 1.17 | 253.46 | 4.4507E-01 | 0.1034 |
| 4871.0 | 7.28E-03 | 93.2 | 6.8 | 296.36 | 18.286 | 1.17 | 211.51 | 3.7203E-01 | 0.1053 |
| 4415.6 | 6.59E-03 | 93.5 | 6.5 | 296.60 | 18.297 | 1.17 | 176.95 | 3.0831E-01 | 0.1071 |
| 3948.4 | 5.87E-03 | 93.8 | 6.2 | 296.78 | 18.306 | 1.17 | 144.36 | 2.5102E-01 | 0.1093 |
| 3659.1 | 5.42E-03 | 94.1 | 5.9 | 296.64 | 18.299 | 1.17 | 125.51 | 2.2169E-01 | 0.1108 |
| 3433.8 | 5.08E-03 | 94.3 | 5.7 | 296.63 | 18.299 | 1.18 | 111.89 | 2.0002E-01 | 0.1122 |
| 3193.2 | 4.71E-03 | 94.5 | 5.5 | 296.55 | 18.295 | 1.18 | 97.48 | 1.7825E-01 | 0.1131 |
| 2938.5 | 4.33E-03 | 94.7 | 5.3 | 296.64 | 18.299 | 1.18 | 84.31 | 1.5385E-01 | 0.1154 |
| 2684.1 | 3.95E-03 | 94.9 | 5.1 | 296.65 | 18.300 | 1.18 | 74.05 | 1.3358E-01 | 0.1215 |
| 2487.1 | 3.64E-03 | 95.1 | 4.9 | 296.46 | 18.291 | 1.18 | 63.96 | 1.1761E-01 | 0.1224 |
| 2187.6 | 3.19E-03 | 95.5 | 4.5 | 296.38 | 18.287 | 1.18 | 51.14 | 9.4901E-02 | 0.1266 |
| 1951.6 | 2.84E-03 | 95.8 | 4.2 | 296.47 | 18.291 | 1.18 | 41.99 | 7.7447E-02 | 0.1305 |
| 1717.3 | 2.49E-03 | 96.2 | 3.8 | 296.56 | 18.295 | 1.18 | 32.53 | 6.2177E-02 | 0.1306 |
| 1462.8 | 2.11E-03 | 96.7 | 3.3 | 296.45 | 18.290 | 1.18 | 23.66 | 4.8050E-02 | 0.1310 |
| 1220.7 | 1.75E-03 | 97.4 | 2.6 | 296.57 | 18.296 | 1.18 | 15.09 | 3.5283E-02 | 0.1198 |
| 1010.6 | 1.44E-03 | 98.0 | 2.0 | 296.71 | 18.303 | 1.18 | 9.39 | 2.8511E-02 | 0.1086 |
| 772.3 | 1.09E-03 | 98.5 | 1.5 | 296.69 | 18.302 | 1.17 | 5.44 | 1.7639E-02 | 0.1077 |
| 515.6 | 7.30E-04 | 98.5 | 1.5 | 296.41 | 18.288 | 1.18 | 3.63 | 1.3697E-02 | 0.1617 |

Table C.5: Data for M40-1 metal foam, and 1/4” open-domain height

| $(Re_{od})^{Dh}$ | $\dot{m}_{total}$ (kg/s) | % $\dot{m}_{od}$ (kg/s) | % $\dot{m}_{pd}$ (kg/s) | $T_{abs}$ (K) | $\mu$ (*$10^6$ Pa·s) | $\rho$ (kg/m$^3$) | (-dp/dx) (Pa/m) | $\tau_w$ (Pa) | $f_{D\text{-}od}$ |
|---|---|---|---|---|---|---|---|---|---|
| 14346.0 | 2.09E-02 | 95.5 | 4.5 | 295.73 | 18.256 | 1.18 | 175.37 | 5.8848E-01 | 0.0927 |
| 13386.5 | 1.95E-02 | 95.7 | 4.3 | 295.70 | 18.254 | 1.18 | 152.08 | 5.1276E-01 | 0.0925 |
| 12367.9 | 1.79E-02 | 95.9 | 4.1 | 295.69 | 18.254 | 1.18 | 129.02 | 4.3689E-01 | 0.0921 |
| 11496.2 | 1.66E-02 | 96.1 | 3.9 | 295.70 | 18.254 | 1.19 | 109.64 | 3.7009E-01 | 0.0908 |
| 10526.2 | 1.52E-02 | 96.3 | 3.7 | 295.69 | 18.253 | 1.19 | 91.50 | 3.1190E-01 | 0.0905 |
| 9528.5 | 1.37E-02 | 96.5 | 3.5 | 295.66 | 18.252 | 1.19 | 74.69 | 2.5321E-01 | 0.0903 |
| 8533.6 | 1.23E-02 | 96.7 | 3.3 | 295.89 | 18.263 | 1.19 | 60.19 | 2.0373E-01 | 0.0907 |
| 7538.9 | 1.08E-02 | 97.0 | 3.0 | 295.96 | 18.267 | 1.19 | 46.90 | 1.6355E-01 | 0.0906 |
| 6497.7 | 9.30E-03 | 97.3 | 2.7 | 295.89 | 18.263 | 1.19 | 35.16 | 1.2697E-01 | 0.0916 |
| 5381.4 | 7.67E-03 | 97.6 | 2.4 | 295.80 | 18.259 | 1.20 | 24.77 | 9.2514E-02 | 0.0942 |
| 4839.4 | 6.88E-03 | 97.8 | 2.2 | 295.72 | 18.255 | 1.20 | 20.04 | 7.7854E-02 | 0.0944 |
| 4355.3 | 6.18E-03 | 98.0 | 2.0 | 295.68 | 18.253 | 1.20 | 16.13 | 6.6434E-02 | 0.0939 |
| 4019.0 | 5.69E-03 | 98.1 | 1.9 | 295.54 | 18.246 | 1.20 | 13.63 | 5.8264E-02 | 0.0933 |
| 3752.3 | 5.31E-03 | 98.3 | 1.7 | 295.81 | 18.259 | 1.20 | 11.83 | 5.0635E-02 | 0.0927 |
| 3529.5 | 4.99E-03 | 98.4 | 1.6 | 295.86 | 18.262 | 1.20 | 10.12 | 4.5354E-02 | 0.0896 |
| 3200.0 | 4.51E-03 | 98.7 | 1.3 | 295.73 | 18.256 | 1.20 | 7.59 | 3.9308E-02 | 0.0819 |
| 3020.2 | 4.25E-03 | 98.8 | 1.2 | 295.91 | 18.264 | 1.20 | 6.13 | 3.6985E-02 | 0.0741 |
| 2680.7 | 3.76E-03 | 99.2 | 0.8 | 295.81 | 18.259 | 1.20 | 3.62 | 3.6130E-02 | 0.0556 |
| 2483.8 | 3.47E-03 | 99.5 | 0.5 | 295.66 | 18.252 | 1.20 | 2.31 | 3.3363E-02 | 0.0414 |
| 2242.4 | 3.14E-03 | 99.5 | 0.5 | 295.81 | 18.259 | 1.20 | 2.02 | 2.7586E-02 | 0.0443 |
| 1865.2 | 2.61E-03 | 99.6 | 0.4 | 295.75 | 18.257 | 1.20 | 1.32 | 2.1326E-02 | 0.0419 |

Table C.6: Data for M40-1 metal foam, and 1/2" open-domain height

| $(Re_{od})^{Dh}$ | $\dot{m}_{total}$ (kg/s) | % $\dot{m}_{od}$ (kg/s) | % $\dot{m}_{pd}$ (kg/s) | $T_{abs}$ (K) | $\mu$ (*$10^6$ Pa·s) | $\rho$ (kg/m$^3$) | (-dp/dx) (Pa/m) | $\tau_w$ (Pa) | $f_{D\text{-}od}$ |
|---|---|---|---|---|---|---|---|---|---|
| 6126.2 | 9.41E-03 | 90.6 | 9.4 | 296.12 | 18.274 | 1.10 | 949.70 | 1.3972E+00 | 0.1054 |
| 5520.9 | 8.43E-03 | 91.1 | 8.9 | 296.10 | 18.273 | 1.12 | 766.32 | 1.1523E+00 | 0.1060 |
| 5117.6 | 7.78E-03 | 91.5 | 8.5 | 296.05 | 18.271 | 1.13 | 656.15 | 9.9286E-01 | 0.1064 |
| 4676.0 | 7.08E-03 | 92.0 | 8.0 | 296.08 | 18.273 | 1.13 | 548.67 | 8.3764E-01 | 0.1073 |
| 4248.1 | 6.40E-03 | 92.5 | 7.5 | 296.14 | 18.275 | 1.14 | 452.68 | 6.9585E-01 | 0.1079 |
| 3801.9 | 5.69E-03 | 93.0 | 7.0 | 296.09 | 18.273 | 1.15 | 363.43 | 5.6156E-01 | 0.1089 |
| 3563.9 | 5.32E-03 | 93.3 | 6.7 | 296.09 | 18.273 | 1.15 | 320.87 | 4.9477E-01 | 0.1098 |
| 3337.8 | 4.97E-03 | 93.6 | 6.4 | 296.15 | 18.276 | 1.16 | 283.50 | 4.3461E-01 | 0.1109 |
| 3100.9 | 4.60E-03 | 93.9 | 6.1 | 296.14 | 18.275 | 1.16 | 245.01 | 3.7807E-01 | 0.1113 |
| 2872.1 | 4.24E-03 | 94.3 | 5.7 | 296.13 | 18.275 | 1.16 | 210.51 | 3.2695E-01 | 0.1117 |
| 2626.7 | 3.87E-03 | 94.5 | 5.5 | 296.11 | 18.274 | 1.16 | 180.35 | 2.7853E-01 | 0.1148 |
| 2384.8 | 3.50E-03 | 95.0 | 5.0 | 296.03 | 18.270 | 1.17 | 148.80 | 2.3261E-01 | 0.1152 |
| 2149.2 | 3.14E-03 | 95.2 | 4.8 | 296.04 | 18.270 | 1.17 | 124.88 | 1.9380E-01 | 0.1192 |
| 1901.1 | 2.77E-03 | 95.6 | 4.4 | 296.06 | 18.271 | 1.17 | 100.93 | 1.5563E-01 | 0.1234 |
| 1679.9 | 2.43E-03 | 96.1 | 3.9 | 296.05 | 18.271 | 1.17 | 77.53 | 1.2299E-01 | 0.1216 |
| 1454.6 | 2.09E-03 | 96.8 | 3.2 | 296.05 | 18.271 | 1.17 | 55.26 | 9.2229E-02 | 0.1158 |
| 1183.4 | 1.69E-03 | 97.4 | 2.6 | 296.04 | 18.270 | 1.18 | 34.77 | 6.1873E-02 | 0.1102 |
| 972.0 | 1.38E-03 | 98.0 | 2.0 | 296.10 | 18.273 | 1.18 | 22.19 | 4.6780E-02 | 0.1043 |
| 756.7 | 1.07E-03 | 98.2 | 1.8 | 296.10 | 18.273 | 1.18 | 15.26 | 3.0975E-02 | 0.1184 |
| 508.4 | 7.21E-04 | 98.2 | 1.8 | 296.16 | 18.276 | 1.18 | 10.28 | 2.1677E-02 | 0.1769 |
| 305.7 | 4.34E-04 | 98.2 | 1.8 | 296.17 | 18.277 | 1.18 | 6.21 | 1.4579E-02 | 0.2957 |
| 101.2 | 1.43E-04 | 98.2 | 1.8 | 296.19 | 18.278 | 1.18 | 2.02 | 7.6790E-03 | 0.8784 |

Table C.7: Data for M60-2 metal foam, and 1/8" open-domain height

| $(Re_{od})^{Dh}$ | $\dot{m}_{total}$ (kg/s) | % $\dot{m}_{od}$ (kg/s) | % $\dot{m}_{pd}$ (kg/s) | $T_{abs}$ (K) | $\mu$ (*$10^6$ Pa·s) | $\rho$ (kg/m$^3$) | (-dp/dx) (Pa/m) | $\tau_w$ (Pa) | $f_{D\text{-}od}$ |
|---|---|---|---|---|---|---|---|---|---|
| 10777.6 | 1.55E-02 | 97.1 | 2.9 | 296.30 | 18.283 | 1.12 | 426.70 | 1.0749E+00 | 0.0816 |
| 10029.9 | 1.44E-02 | 97.3 | 2.7 | 296.17 | 18.277 | 1.13 | 365.05 | 9.2003E-01 | 0.0811 |
| 9093.1 | 1.30E-02 | 97.5 | 2.5 | 296.21 | 18.279 | 1.13 | 296.89 | 7.4233E-01 | 0.0807 |
| 8165.5 | 1.16E-02 | 97.7 | 2.3 | 296.25 | 18.280 | 1.14 | 240.34 | 5.9296E-01 | 0.0814 |
| 7174.8 | 1.02E-02 | 97.9 | 2.1 | 296.22 | 18.279 | 1.14 | 187.95 | 4.5051E-01 | 0.0829 |
| 6169.7 | 8.76E-03 | 98.1 | 1.9 | 296.17 | 18.276 | 1.15 | 139.61 | 3.2638E-01 | 0.0837 |
| 5683.4 | 8.06E-03 | 98.2 | 1.8 | 296.27 | 18.281 | 1.15 | 120.36 | 2.7606E-01 | 0.0851 |
| 5159.5 | 7.31E-03 | 98.4 | 1.6 | 296.26 | 18.281 | 1.15 | 99.27 | 2.2554E-01 | 0.0854 |
| 4634.9 | 6.55E-03 | 98.5 | 1.5 | 296.27 | 18.282 | 1.16 | 81.38 | 1.8411E-01 | 0.0869 |
| 4152.4 | 5.86E-03 | 98.7 | 1.3 | 296.32 | 18.284 | 1.16 | 65.53 | 1.4808E-01 | 0.0873 |
| 3866.0 | 5.45E-03 | 98.7 | 1.3 | 296.18 | 18.277 | 1.16 | 56.78 | 1.2904E-01 | 0.0875 |
| 3607.9 | 5.09E-03 | 98.8 | 1.2 | 296.25 | 18.281 | 1.16 | 49.68 | 1.1241E-01 | 0.0879 |
| 3334.8 | 4.70E-03 | 98.9 | 1.1 | 296.22 | 18.279 | 1.16 | 41.34 | 9.3341E-02 | 0.0857 |
| 3082.1 | 4.33E-03 | 99.2 | 0.8 | 296.36 | 18.286 | 1.16 | 28.92 | 7.6556E-02 | 0.0702 |
| 2833.3 | 3.96E-03 | 99.7 | 0.3 | 296.31 | 18.284 | 1.16 | 10.51 | 9.5486E-02 | 0.0302 |
| 2627.6 | 3.67E-03 | 99.7 | 0.3 | 296.28 | 18.282 | 1.16 | 8.24 | 8.0577E-02 | 0.0276 |
| 2296.1 | 3.21E-03 | 99.7 | 0.3 | 296.26 | 18.281 | 1.17 | 7.21 | 4.1253E-02 | 0.0316 |
| 2046.2 | 2.86E-03 | 99.7 | 0.3 | 296.23 | 18.279 | 1.17 | 6.27 | 2.8515E-02 | 0.0347 |
| 1769.5 | 2.47E-03 | 99.7 | 0.3 | 296.28 | 18.282 | 1.17 | 5.92 | 2.4605E-02 | 0.0438 |
| 1528.7 | 2.14E-03 | 99.7 | 0.3 | 296.16 | 18.276 | 1.17 | 5.64 | 2.2308E-02 | 0.0560 |
| 1254.8 | 1.75E-03 | 99.7 | 0.3 | 296.19 | 18.278 | 1.17 | 4.57 | 1.8873E-02 | 0.0674 |
| 1055.2 | 1.47E-03 | 99.7 | 0.3 | 296.25 | 18.280 | 1.17 | 3.99 | 1.6383E-02 | 0.0833 |
| 780.4 | 1.09E-03 | 99.6 | 0.4 | 296.21 | 18.279 | 1.17 | 3.34 | 1.3305E-02 | 0.1276 |
| 523.2 | 7.32E-04 | 99.6 | 0.4 | 296.24 | 18.280 | 1.17 | 2.28 | 1.0737E-02 | 0.1939 |

Table C.8: Data for M60-2 metal foam, and 1/4” open-domain height

| $(Re_{od})^{Dh}$ | $\dot{m}_{total}$ (kg/s) | % $\dot{m}_{od}$ (kg/s) | % $\dot{m}_{pd}$ (kg/s) | $T_{abs}$ (K) | $\mu$ (*$10^6$ Pa·s) | $\rho$ (kg/m$^3$) | (-dp/dx) (Pa/m) | $\tau_w$ (Pa) | $f_{D\text{-}od}$ |
|---|---|---|---|---|---|---|---|---|---|
| 14871.5 | 2.08E-02 | 99.5 | 0.5 | 295.71 | 18.255 | 1.17 | 94.62 | 4.6514E-01 | 0.0643 |
| 13787.3 | 1.93E-02 | 99.5 | 0.5 | 295.72 | 18.255 | 1.17 | 80.97 | 3.9507E-01 | 0.0642 |
| 12851.9 | 1.80E-02 | 99.5 | 0.5 | 295.64 | 18.251 | 1.17 | 70.78 | 3.3677E-01 | 0.0647 |
| 11903.7 | 1.66E-02 | 99.6 | 0.4 | 295.73 | 18.256 | 1.17 | 59.97 | 2.8397E-01 | 0.0639 |
| 10801.2 | 1.51E-02 | 99.6 | 0.4 | 295.82 | 18.260 | 1.18 | 49.49 | 2.2577E-01 | 0.0641 |
| 9855.6 | 1.38E-02 | 99.6 | 0.4 | 295.74 | 18.256 | 1.18 | 40.97 | 1.8825E-01 | 0.0639 |
| 8797.3 | 1.23E-02 | 99.7 | 0.3 | 295.77 | 18.257 | 1.18 | 32.40 | 1.4685E-01 | 0.0635 |
| 7706.4 | 1.08E-02 | 99.7 | 0.3 | 295.73 | 18.255 | 1.18 | 24.96 | 1.1219E-01 | 0.0638 |
| 6621.5 | 9.24E-03 | 99.7 | 0.3 | 295.89 | 18.263 | 1.18 | 18.46 | 8.2260E-02 | 0.0639 |
| 5528.2 | 7.71E-03 | 99.8 | 0.2 | 295.80 | 18.259 | 1.18 | 12.34 | 5.8324E-02 | 0.0614 |
| 4950.0 | 6.89E-03 | 99.8 | 0.2 | 295.51 | 18.245 | 1.18 | 9.44 | 4.9747E-02 | 0.0588 |
| 4399.4 | 6.13E-03 | 99.9 | 0.1 | 295.57 | 18.248 | 1.18 | 6.72 | 4.0604E-02 | 0.0530 |
| 4116.4 | 5.73E-03 | 99.9 | 0.1 | 295.73 | 18.256 | 1.18 | 5.38 | 3.4986E-02 | 0.0484 |
| 3836.3 | 5.34E-03 | 99.9 | 0.1 | 295.85 | 18.261 | 1.18 | 4.06 | 3.0780E-02 | 0.0420 |
| 3542.5 | 4.93E-03 | 99.9 | 0.1 | 295.77 | 18.257 | 1.18 | 3.30 | 2.7839E-02 | 0.0401 |
| 3285.2 | 4.57E-03 | 99.9 | 0.1 | 295.70 | 18.254 | 1.18 | 2.36 | 2.5027E-02 | 0.0333 |
| 3012.5 | 4.19E-03 | 100.0 | 0.0 | 295.80 | 18.259 | 1.18 | 1.47 | 1.9169E-02 | 0.0247 |
| 2720.6 | 3.79E-03 | 100.0 | 0.0 | 295.87 | 18.262 | 1.18 | 1.11 | 1.5350E-02 | 0.0228 |
| 2415.9 | 3.36E-03 | 100.0 | 0.0 | 295.76 | 18.257 | 1.18 | 1.29 | 1.4768E-02 | 0.0337 |
| 2156.1 | 3.00E-03 | 100.0 | 0.0 | 295.69 | 18.253 | 1.18 | 1.06 | 1.4127E-02 | 0.0348 |
| 1877.9 | 2.61E-03 | 99.9 | 0.1 | 295.68 | 18.253 | 1.18 | 1.15 | 1.3376E-02 | 0.0497 |

Table C.9: Data for M60-2 metal foam, and 1/2” open-domain height

| $(Re_{od})^{Dh}$ | $\dot{m}_{total}$ (kg/s) | % $\dot{m}_{od}$ (kg/s) | % $\dot{m}_{pd}$ (kg/s) | $T_{abs}$ (K) | $\mu$ (*$10^6$ Pa·s) | $\rho$ (kg/m$^3$) | (-dp/dx) (Pa/m) | $\tau_w$ (Pa) | $f_{D\text{-}od}$ |
|---|---|---|---|---|---|---|---|---|---|
| 4171.4 | 9.27E-03 | 62.7 | 37.3 | 296.17 | 18.277 | 1.11 | 1336.71 | 1.2220E+00 | 0.0922 |
| 3789.4 | 8.40E-03 | 62.8 | 37.2 | 296.20 | 18.278 | 1.12 | 1115.55 | 1.0409E+00 | 0.0942 |
| 3500.1 | 7.74E-03 | 63.0 | 37.0 | 296.23 | 18.280 | 1.13 | 964.71 | 9.0918E-01 | 0.0961 |
| 3185.3 | 7.02E-03 | 63.2 | 36.8 | 296.24 | 18.280 | 1.14 | 809.90 | 7.7581E-01 | 0.0981 |
| 2877.5 | 6.32E-03 | 63.5 | 36.5 | 296.24 | 18.280 | 1.15 | 674.14 | 6.5738E-01 | 0.1006 |
| 2574.3 | 5.63E-03 | 63.7 | 36.3 | 296.24 | 18.280 | 1.15 | 554.43 | 5.4431E-01 | 0.1040 |
| 2417.8 | 5.27E-03 | 64.0 | 36.0 | 296.30 | 18.283 | 1.16 | 494.88 | 4.8875E-01 | 0.1054 |
| 2270.1 | 4.93E-03 | 64.2 | 35.8 | 296.33 | 18.284 | 1.16 | 441.94 | 4.3581E-01 | 0.1070 |
| 2108.6 | 4.56E-03 | 64.5 | 35.5 | 296.34 | 18.285 | 1.16 | 388.64 | 3.8730E-01 | 0.1093 |
| 1950.9 | 4.19E-03 | 64.8 | 35.2 | 296.27 | 18.281 | 1.16 | 338.20 | 3.4202E-01 | 0.1115 |
| 1792.6 | 3.84E-03 | 65.1 | 34.9 | 296.22 | 18.279 | 1.17 | 293.44 | 2.9732E-01 | 0.1148 |
| 1644.3 | 3.49E-03 | 65.6 | 34.4 | 296.22 | 18.279 | 1.17 | 250.76 | 2.5812E-01 | 0.1168 |
| 1496.8 | 3.15E-03 | 66.2 | 33.8 | 296.23 | 18.280 | 1.17 | 211.40 | 2.2177E-01 | 0.1190 |
| 1339.8 | 2.78E-03 | 67.1 | 32.9 | 296.20 | 18.278 | 1.17 | 172.51 | 1.8823E-01 | 0.1214 |
| 1180.2 | 2.41E-03 | 68.1 | 31.9 | 296.24 | 18.280 | 1.17 | 136.76 | 1.5362E-01 | 0.1242 |
| 1004.1 | 2.02E-03 | 69.3 | 30.7 | 296.13 | 18.275 | 1.18 | 103.65 | 1.1947E-01 | 0.1303 |
| 868.8 | 1.71E-03 | 70.8 | 29.2 | 296.11 | 18.274 | 1.18 | 79.14 | 9.4705E-02 | 0.1330 |
| 694.7 | 1.32E-03 | 73.1 | 26.9 | 296.08 | 18.272 | 1.18 | 52.72 | 6.6139E-02 | 0.1387 |
| 574.1 | 1.07E-03 | 74.6 | 25.4 | 296.18 | 18.277 | 1.18 | 38.63 | 4.8492E-02 | 0.1488 |
| 400.2 | 7.12E-04 | 78.3 | 21.7 | 296.17 | 18.277 | 1.18 | 20.67 | 2.9278E-02 | 0.1639 |
| 239.5 | 4.27E-04 | 78.1 | 21.9 | 296.20 | 18.278 | 1.18 | 12.17 | 1.9338E-02 | 0.2695 |
| 78.6 | 1.42E-04 | 76.9 | 23.1 | 296.19 | 18.278 | 1.18 | 4.12 | 9.8241E-03 | 0.8484 |

Table C.10: Data for ERG40-1 metal foam, and 1/8” open-domain height

| $(Re_{od})^{Dh}$ | $\dot{m}_{total}$ (kg/s) | % $\dot{m}_{od}$ (kg/s) | % $\dot{m}_{pd}$ (kg/s) | $T_{abs}$ (K) | $\mu$ (*$10^6$ Pa·s) | $\rho$ (kg/m$^3$) | (-dp/dx) (Pa/m) | $\tau_w$ (Pa) | $f_{D\text{-}od}$ |
|---|---|---|---|---|---|---|---|---|---|
| 9172.4 | 1.52E-02 | 84.0 | 16.0 | 296.49 | 18.292 | 1.12 | 751.73 | 1.1410E+00 | 0.1035 |
| 8650.6 | 1.43E-02 | 84.2 | 15.8 | 296.43 | 18.289 | 1.13 | 665.53 | 1.0048E+00 | 0.1035 |
| 7826.5 | 1.29E-02 | 84.6 | 15.4 | 296.49 | 18.292 | 1.14 | 542.28 | 8.2063E-01 | 0.1036 |
| 7047.8 | 1.16E-02 | 84.9 | 15.1 | 296.49 | 18.292 | 1.14 | 439.88 | 6.7693E-01 | 0.1042 |
| 6220.1 | 1.01E-02 | 85.4 | 14.6 | 296.50 | 18.293 | 1.15 | 343.46 | 5.3276E-01 | 0.1050 |
| 5358.4 | 8.68E-03 | 86.0 | 14.0 | 296.51 | 18.293 | 1.15 | 257.30 | 4.0374E-01 | 0.1064 |
| 4948.7 | 7.99E-03 | 86.4 | 13.6 | 296.47 | 18.291 | 1.16 | 221.40 | 3.4862E-01 | 0.1076 |
| 4523.9 | 7.27E-03 | 86.8 | 13.2 | 296.52 | 18.293 | 1.16 | 186.03 | 2.9489E-01 | 0.1084 |
| 4070.4 | 6.50E-03 | 87.2 | 12.8 | 296.50 | 18.292 | 1.16 | 153.09 | 2.4525E-01 | 0.1104 |
| 3662.8 | 5.82E-03 | 87.7 | 12.3 | 296.48 | 18.291 | 1.16 | 125.41 | 2.0423E-01 | 0.1119 |
| 3415.1 | 5.40E-03 | 88.1 | 11.9 | 296.46 | 18.291 | 1.16 | 109.63 | 1.8337E-01 | 0.1127 |
| 3177.7 | 5.01E-03 | 88.4 | 11.6 | 296.48 | 18.292 | 1.16 | 96.49 | 1.6226E-01 | 0.1146 |
| 2970.2 | 4.67E-03 | 88.7 | 11.3 | 296.49 | 18.292 | 1.17 | 85.49 | 1.4393E-01 | 0.1163 |
| 2752.7 | 4.31E-03 | 89.0 | 11.0 | 296.49 | 18.292 | 1.17 | 74.60 | 1.2594E-01 | 0.1182 |
| 2526.7 | 3.95E-03 | 89.3 | 10.7 | 296.49 | 18.292 | 1.17 | 65.53 | 1.1001E-01 | 0.1234 |
| 2287.2 | 3.56E-03 | 89.5 | 10.5 | 296.47 | 18.291 | 1.17 | 56.75 | 9.3029E-02 | 0.1304 |
| 2055.1 | 3.19E-03 | 89.9 | 10.1 | 296.53 | 18.294 | 1.17 | 47.11 | 7.6987E-02 | 0.1342 |
| 1834.0 | 2.82E-03 | 90.5 | 9.5 | 296.50 | 18.293 | 1.17 | 38.30 | 6.3441E-02 | 0.1370 |
| 1602.5 | 2.45E-03 | 91.2 | 8.8 | 296.47 | 18.291 | 1.17 | 30.21 | 5.0903E-02 | 0.1417 |
| 1384.0 | 2.10E-03 | 92.1 | 7.9 | 296.46 | 18.291 | 1.17 | 22.65 | 3.9555E-02 | 0.1425 |
| 1152.1 | 1.73E-03 | 92.8 | 7.2 | 296.51 | 18.293 | 1.17 | 16.67 | 2.9104E-02 | 0.1513 |
| 965.4 | 1.43E-03 | 93.8 | 6.2 | 296.49 | 18.292 | 1.17 | 11.57 | 2.2277E-02 | 0.1497 |
| 744.4 | 1.09E-03 | 95.6 | 4.4 | 296.51 | 18.293 | 1.17 | 6.06 | 1.5471E-02 | 0.1319 |
| 497.8 | 7.22E-04 | 96.1 | 3.9 | 296.50 | 18.292 | 1.17 | 3.56 | 1.0152E-02 | 0.1733 |

Table C.11: Data for ERG40-1 metal foam, and 1/4” open-domain height

| $(Re_{od})^{Dh}$ | $\dot{m}_{total}$ (kg/s) | % $\dot{m}_{od}$ (kg/s) | % $\dot{m}_{pd}$ (kg/s) | $T_{abs}$ (K) | $\mu$ (*$10^6$ Pa·s) | $\rho$ (kg/m$^3$) | (-dp/dx) (Pa/m) | $\tau_w$ (Pa) | $f_{D\text{-}od}$ |
|---|---|---|---|---|---|---|---|---|---|
| 14346.0 | 2.09E-02 | 95.5 | 4.5 | 295.73 | 18.256 | 1.18 | 175.37 | 5.8848E-01 | 0.0927 |
| 13386.5 | 1.95E-02 | 95.7 | 4.3 | 295.70 | 18.254 | 1.18 | 152.08 | 5.1276E-01 | 0.0925 |
| 12367.9 | 1.79E-02 | 95.9 | 4.1 | 295.69 | 18.254 | 1.18 | 129.02 | 4.3689E-01 | 0.0921 |
| 11496.2 | 1.66E-02 | 96.1 | 3.9 | 295.70 | 18.254 | 1.19 | 109.64 | 3.7009E-01 | 0.0908 |
| 10526.2 | 1.52E-02 | 96.3 | 3.7 | 295.69 | 18.253 | 1.19 | 91.50 | 3.1190E-01 | 0.0905 |
| 9528.5 | 1.37E-02 | 96.5 | 3.5 | 295.66 | 18.252 | 1.19 | 74.69 | 2.5321E-01 | 0.0903 |
| 8533.6 | 1.23E-02 | 96.7 | 3.3 | 295.89 | 18.263 | 1.19 | 60.19 | 2.0373E-01 | 0.0907 |
| 7538.9 | 1.08E-02 | 97.0 | 3.0 | 295.96 | 18.267 | 1.19 | 46.90 | 1.6355E-01 | 0.0906 |
| 6497.7 | 9.30E-03 | 97.3 | 2.7 | 295.89 | 18.263 | 1.19 | 35.16 | 1.2697E-01 | 0.0916 |
| 5381.4 | 7.67E-03 | 97.6 | 2.4 | 295.80 | 18.259 | 1.20 | 24.77 | 9.2514E-02 | 0.0942 |
| 4839.4 | 6.88E-03 | 97.8 | 2.2 | 295.72 | 18.255 | 1.20 | 20.04 | 7.7854E-02 | 0.0944 |
| 4355.3 | 6.18E-03 | 98.0 | 2.0 | 295.68 | 18.253 | 1.20 | 16.13 | 6.6434E-02 | 0.0939 |
| 4019.0 | 5.69E-03 | 98.1 | 1.9 | 295.54 | 18.246 | 1.20 | 13.63 | 5.8264E-02 | 0.0933 |
| 3752.3 | 5.31E-03 | 98.3 | 1.7 | 295.81 | 18.259 | 1.20 | 11.83 | 5.0635E-02 | 0.0927 |
| 3529.5 | 4.99E-03 | 98.4 | 1.6 | 295.86 | 18.262 | 1.20 | 10.12 | 4.5354E-02 | 0.0896 |
| 3200.0 | 4.51E-03 | 98.7 | 1.3 | 295.73 | 18.256 | 1.20 | 7.59 | 3.9308E-02 | 0.0819 |
| 3020.2 | 4.25E-03 | 98.8 | 1.2 | 295.91 | 18.264 | 1.20 | 6.13 | 3.6985E-02 | 0.0741 |
| 2680.7 | 3.76E-03 | 99.2 | 0.8 | 295.81 | 18.259 | 1.20 | 3.62 | 3.6130E-02 | 0.0556 |
| 2483.8 | 3.47E-03 | 99.5 | 0.5 | 295.66 | 18.252 | 1.20 | 2.31 | 3.3363E-02 | 0.0414 |
| 2242.4 | 3.14E-03 | 99.5 | 0.5 | 295.81 | 18.259 | 1.20 | 2.02 | 2.7586E-02 | 0.0443 |
| 1865.2 | 2.61E-03 | 99.6 | 0.4 | 295.75 | 18.257 | 1.20 | 1.32 | 2.1326E-02 | 0.0419 |

Table C.12: Data for ERG40-1 metal foam, and 1/2” open-domain height

| $(Re_{od})^{Dh}$ | $\dot{m}_{total}$ (kg/s) | % $\dot{m}_{od}$ (kg/s) | % $\dot{m}_{pd}$ (kg/s) | $T_{abs}$ (K) | $\mu$ (*$10^6$ Pa·s) | $\rho$ (kg/m$^3$) | (-dp/dx) (Pa/m) | $\tau_w$ (Pa) | $f_{D\text{-}od}$ |
|---|---|---|---|---|---|---|---|---|---|
| 4082.3 | 9.09E-03 | 62.7 | 37.3 | 296.82 | 18.308 | 1.10 | 1303.75 | 1.1807E+00 | 0.0928 |
| 3783.8 | 8.40E-03 | 62.8 | 37.2 | 296.84 | 18.309 | 1.11 | 1126.69 | 1.0356E+00 | 0.0941 |
| 3495.5 | 7.74E-03 | 63.0 | 37.0 | 296.85 | 18.309 | 1.12 | 974.37 | 9.0817E-01 | 0.0961 |
| 3193.8 | 7.04E-03 | 63.3 | 36.7 | 296.82 | 18.308 | 1.13 | 819.21 | 7.8179E-01 | 0.0976 |
| 2869.6 | 6.30E-03 | 63.5 | 36.5 | 296.81 | 18.307 | 1.14 | 676.07 | 6.5408E-01 | 0.1005 |
| 2571.9 | 5.63E-03 | 63.8 | 36.2 | 296.80 | 18.307 | 1.15 | 556.88 | 5.4584E-01 | 0.1037 |
| 2415.6 | 5.26E-03 | 64.0 | 36.0 | 296.80 | 18.307 | 1.15 | 496.25 | 4.8997E-01 | 0.1051 |
| 2260.3 | 4.91E-03 | 64.2 | 35.8 | 296.81 | 18.307 | 1.15 | 442.48 | 4.3696E-01 | 0.1074 |
| 2106.3 | 4.56E-03 | 64.5 | 35.5 | 296.82 | 18.308 | 1.16 | 388.99 | 3.9098E-01 | 0.1090 |
| 1949.8 | 4.20E-03 | 64.8 | 35.2 | 296.82 | 18.308 | 1.16 | 339.88 | 3.4600E-01 | 0.1115 |
| 1791.4 | 3.83E-03 | 65.2 | 34.8 | 296.81 | 18.307 | 1.16 | 292.32 | 3.0141E-01 | 0.1139 |
| 1650.1 | 3.51E-03 | 65.7 | 34.3 | 296.78 | 18.306 | 1.17 | 252.37 | 2.6374E-01 | 0.1162 |
| 1486.5 | 3.13E-03 | 66.3 | 33.7 | 296.75 | 18.305 | 1.17 | 209.66 | 2.2410E-01 | 0.1192 |
| 1337.3 | 2.78E-03 | 67.2 | 32.8 | 296.71 | 18.302 | 1.17 | 171.14 | 1.9167E-01 | 0.1205 |
| 1179.2 | 2.41E-03 | 68.1 | 31.9 | 296.69 | 18.301 | 1.17 | 136.79 | 1.5746E-01 | 0.1241 |
| 1025.4 | 2.07E-03 | 69.2 | 30.8 | 296.73 | 18.303 | 1.18 | 106.92 | 1.2554E-01 | 0.1285 |
| 882.1 | 1.74E-03 | 70.7 | 29.3 | 296.81 | 18.307 | 1.18 | 81.25 | 9.8931E-02 | 0.1321 |
| 723.9 | 1.39E-03 | 72.8 | 27.2 | 296.64 | 18.299 | 1.18 | 56.32 | 7.2950E-02 | 0.1363 |
| 571.9 | 1.07E-03 | 74.4 | 25.6 | 296.73 | 18.304 | 1.18 | 39.05 | 5.0879E-02 | 0.1515 |
| 401.6 | 7.17E-04 | 78.1 | 21.9 | 296.77 | 18.305 | 1.18 | 21.01 | 3.1453E-02 | 0.1653 |
| 241.8 | 4.32E-04 | 78.1 | 21.9 | 296.70 | 18.302 | 1.18 | 12.29 | 2.1253E-02 | 0.2671 |
| 80.0 | 1.43E-04 | 78.2 | 21.8 | 296.71 | 18.303 | 1.18 | 3.89 | 1.0938E-02 | 0.7728 |

Table C.13: Data for ERG40-2, and 1/8” open-domain height

| $(Re_{od})^{Dh}$ | $\dot{m}_{total}$ (kg/s) | % $\dot{m}_{od}$ (kg/s) | % $\dot{m}_{pd}$ (kg/s) | $T_{abs}$ (K) | $\mu$ (*$10^6$ Pa·s) | $\rho$ (kg/m$^3$) | (-dp/dx) (Pa/m) | $\tau_w$ (Pa) | $f_{D\text{-}od}$ |
|---|---|---|---|---|---|---|---|---|---|
| 9078.9 | 1.51E-02 | 84.0 | 16.0 | 296.39 | 18.287 | 1.12 | 738.99 | 1.1197E+00 | 0.1031 |
| 8586.7 | 1.42E-02 | 84.2 | 15.8 | 296.39 | 18.287 | 1.12 | 658.94 | 1.0116E+00 | 0.1033 |
| 7776.0 | 1.28E-02 | 84.6 | 15.4 | 296.38 | 18.287 | 1.13 | 538.57 | 8.3396E-01 | 0.1036 |
| 6996.8 | 1.15E-02 | 85.0 | 15.0 | 296.39 | 18.287 | 1.14 | 434.15 | 6.8250E-01 | 0.1037 |
| 6192.2 | 1.01E-02 | 85.4 | 14.6 | 296.39 | 18.287 | 1.14 | 343.08 | 5.4267E-01 | 0.1052 |
| 5355.6 | 8.67E-03 | 86.0 | 14.0 | 296.41 | 18.288 | 1.15 | 258.85 | 4.1782E-01 | 0.1066 |
| 4934.5 | 7.96E-03 | 86.4 | 13.6 | 296.38 | 18.287 | 1.15 | 221.38 | 3.6103E-01 | 0.1077 |
| 4498.0 | 7.22E-03 | 86.8 | 13.2 | 296.40 | 18.287 | 1.15 | 184.42 | 3.0529E-01 | 0.1082 |
| 4063.2 | 6.49E-03 | 87.2 | 12.8 | 296.38 | 18.287 | 1.15 | 153.45 | 2.5442E-01 | 0.1106 |
| 3646.2 | 5.79E-03 | 87.7 | 12.3 | 296.44 | 18.290 | 1.16 | 125.06 | 2.1133E-01 | 0.1120 |
| 3399.0 | 5.38E-03 | 88.0 | 12.0 | 296.41 | 18.288 | 1.16 | 110.23 | 1.9106E-01 | 0.1137 |
| 3182.6 | 5.02E-03 | 88.4 | 11.6 | 296.38 | 18.287 | 1.16 | 97.40 | 1.7124E-01 | 0.1147 |
| 2962.1 | 4.65E-03 | 88.8 | 11.2 | 296.37 | 18.286 | 1.16 | 84.98 | 1.5182E-01 | 0.1157 |
| 2742.3 | 4.29E-03 | 89.1 | 10.9 | 296.41 | 18.288 | 1.16 | 74.21 | 1.3357E-01 | 0.1179 |
| 2514.8 | 3.92E-03 | 89.3 | 10.7 | 296.38 | 18.287 | 1.16 | 65.10 | 1.1627E-01 | 0.1231 |
| 2273.5 | 3.54E-03 | 89.5 | 10.5 | 296.41 | 18.288 | 1.16 | 56.51 | 9.9291E-02 | 0.1308 |
| 2053.8 | 3.18E-03 | 90.0 | 10.0 | 296.38 | 18.287 | 1.16 | 47.11 | 8.3967E-02 | 0.1338 |
| 1821.0 | 2.80E-03 | 90.6 | 9.4 | 296.39 | 18.287 | 1.16 | 37.96 | 6.9083E-02 | 0.1372 |
| 1596.5 | 2.44E-03 | 91.2 | 8.8 | 296.37 | 18.286 | 1.16 | 30.25 | 5.6446E-02 | 0.1423 |
| 1385.8 | 2.10E-03 | 91.9 | 8.1 | 296.38 | 18.287 | 1.16 | 23.21 | 4.5102E-02 | 0.1450 |
| 1162.9 | 1.75E-03 | 92.8 | 7.2 | 296.37 | 18.286 | 1.16 | 16.78 | 3.4121E-02 | 0.1488 |
| 969.5 | 1.44E-03 | 93.9 | 6.1 | 296.43 | 18.289 | 1.16 | 11.56 | 2.6608E-02 | 0.1475 |
| 741.2 | 1.08E-03 | 95.8 | 4.2 | 296.36 | 18.286 | 1.16 | 5.77 | 1.8852E-02 | 0.1260 |
| 498.3 | 7.19E-04 | 96.6 | 3.4 | 296.48 | 18.291 | 1.16 | 3.11 | 1.2887E-02 | 0.1500 |

Table C.14: Data for fully ERG40-2 metal foam, and 1/4” open-domain height

| $(Re_{od})^{Dh}$ | $\dot{m}_{total}$ (kg/s) | % $\dot{m}_{od}$ (kg/s) | % $\dot{m}_{pd}$ (kg/s) | $T_{abs}$ (K) | $\mu$ (*$10^6$ Pa·s) | $\rho$ (kg/m$^3$) | (-dp/dx) (Pa/m) | $\tau_w$ (Pa) | $f_{D\text{-}od}$ |
|---|---|---|---|---|---|---|---|---|---|
| 14368.2 | 2.09E-02 | 95.5 | 4.5 | 294.75 | 18.209 | 1.18 | 175.68 | 5.9391E-01 | 0.0931 |
| 13345.3 | 1.94E-02 | 95.7 | 4.3 | 294.75 | 18.209 | 1.18 | 150.92 | 5.1056E-01 | 0.0929 |
| 12425.5 | 1.80E-02 | 95.9 | 4.1 | 294.81 | 18.211 | 1.18 | 128.35 | 4.3773E-01 | 0.0912 |
| 11508.0 | 1.66E-02 | 96.1 | 3.9 | 294.84 | 18.213 | 1.19 | 109.87 | 3.6895E-01 | 0.0911 |
| 10474.1 | 1.51E-02 | 96.3 | 3.7 | 294.90 | 18.216 | 1.19 | 89.89 | 3.0574E-01 | 0.0900 |
| 9501.4 | 1.37E-02 | 96.5 | 3.5 | 294.79 | 18.211 | 1.19 | 74.22 | 2.5398E-01 | 0.0905 |
| 8517.5 | 1.22E-02 | 96.7 | 3.3 | 294.79 | 18.210 | 1.19 | 59.56 | 2.0587E-01 | 0.0905 |
| 7480.9 | 1.07E-02 | 97.0 | 3.0 | 294.74 | 18.208 | 1.19 | 45.71 | 1.6565E-01 | 0.0901 |
| 6422.9 | 9.16E-03 | 97.3 | 2.7 | 294.72 | 18.207 | 1.19 | 34.39 | 1.2639E-01 | 0.0921 |
| 5411.8 | 7.69E-03 | 97.6 | 2.4 | 294.88 | 18.215 | 1.19 | 24.57 | 9.3060E-02 | 0.0927 |
| 4846.8 | 6.88E-03 | 97.8 | 2.2 | 294.81 | 18.211 | 1.19 | 20.25 | 7.8365E-02 | 0.0953 |
| 4307.4 | 6.10E-03 | 98.0 | 2.0 | 294.79 | 18.211 | 1.19 | 15.76 | 6.4602E-02 | 0.0939 |
| 4037.9 | 5.71E-03 | 98.1 | 1.9 | 294.73 | 18.208 | 1.19 | 14.04 | 5.8304E-02 | 0.0952 |
| 3758.1 | 5.31E-03 | 98.3 | 1.7 | 294.84 | 18.213 | 1.19 | 11.82 | 5.1338E-02 | 0.0925 |
| 3480.5 | 4.91E-03 | 98.4 | 1.6 | 294.77 | 18.209 | 1.19 | 10.11 | 4.5914E-02 | 0.0922 |
| 3196.0 | 4.50E-03 | 98.6 | 1.4 | 294.80 | 18.211 | 1.19 | 7.71 | 4.0191E-02 | 0.0834 |
| 2950.5 | 4.14E-03 | 98.9 | 1.1 | 294.80 | 18.211 | 1.19 | 5.55 | 3.7706E-02 | 0.0704 |
| 2695.6 | 3.77E-03 | 99.2 | 0.8 | 294.69 | 18.206 | 1.19 | 3.65 | 3.7545E-02 | 0.0555 |
| 2421.3 | 3.38E-03 | 99.4 | 0.6 | 294.70 | 18.206 | 1.19 | 2.43 | 3.2990E-02 | 0.0458 |
| 2128.2 | 2.97E-03 | 99.5 | 0.5 | 294.71 | 18.206 | 1.19 | 2.00 | 2.6993E-02 | 0.0488 |
| 1851.3 | 2.58E-03 | 99.6 | 0.4 | 294.78 | 18.210 | 1.19 | 1.39 | 2.1604E-02 | 0.0448 |

Table C.15: Data for ERG40-2 metal foam, and 1/2” open-domain height